Title

Insights into the Tectonometamorphic Evolution of the Whipple Mountains Ductile Shear Zone, Southeastern California

Author

Jaramillo Hernandez, Valeria Guadalupe

Publication Date

2024

Peer reviewed|Thesis/dissertation

UNIVERSITY OF CALIFORNIA

Los Angeles

Insights into the tectonometamorphic evolution of the Whipple Mountains ductile shear zone, Southeastern California

A dissertation submitted in partial satisfaction of the requirements for

the degree Doctor of Philosophy in Geology

by

Valeria Guadalupe Jaramillo Hernandez

2024

ABSTRACT OF THE DISSERTATION

Insights into the tectonometamorphic evolution of the Whipple Mountains ductile shear zone, Southeastern California

by

Valeria Guadalupe Jaramillo Hernandez

Doctor of Philosophy in Geology

University of California, Los Angeles, 2024

Professor Craig E. Manning, Chair

The North American Cordilleran metamorphic core-complex belt provides insight into the tectonometamorphic evolution of North America. Specifically, the Whipple Mountains metamorphic core complex, or the birthplace of the modern concept of low-angle detachment faulting, has been a target of research for decades. Each project presented in this dissertation addresses scientific questions regarding the deformation history of the Whipple Mountains shear zone which build on each other to provide a holistic view of the geologic history. First, new pressure, temperature, and timing (P-T-t) of deformation constraints were determined for shear zone rocks. The high P-T conditions and the structural relations in the rocks allow for different styles of deformation to be present in the brittle-ductile transition zone at 15-20 km depth where the pore-fluid pressure ratios may be calculated. Finally, a new model is proposed to further explain the formation of the Whipple detachment fault which suggests it may have been active since Mesozoic time. The advancement of analytical tools continues to help bridge the gap between

what is known and what can be further discovered, and these projects may help further understand the evolution of the metamorphic core complexes in North America.

The dissertation of Valeria Guadalupe Jaramillo Hernandez is approved.

Mackenzie D. Day

Timothy Mark Harrison

Gilles F. Peltzer

Craig E. Manning, Committee Chair

University of California, Los Angeles

2024

Table of Contents

List of Figures and Tables

Acknowledgements

As I attempt to wrap up this dissertation time seems to have slowed and I am remembering everything that has happened during my PhD journey, a journey that was made possible because my late advisor, Professor An Yin, gave me the opportunity to join his research group and pursue a graduate degree. Working with An was a tremendous learning experience which helped me grow immensely, as a researcher, as an educator, and as a person– thank you, An.

Firstly, I would like to thank my current advisor, Craig Manning, for allowing me to continue working on my degree, at the time, I did not think I would make it, but I am so grateful for your support and encouragement. My committee members, Mackenzie Day, Gilles Peltzer, and Mark Harrison. Kenzie, thank you for your kindness and willingness to have group meetings with all of us, it meant a lot to have that help when needed (and I really needed it sometimes). Gilles, thank you for your support and for being so passionate about remote sensing, I learned a lot in your classes and the Death Valley trips have been some of my favorites. Last, but not least, Mark, thank you for encouraging me to step out of my comfort zone and take the Planet Habitability course, it was honestly my favorite class, and I learned so much. I wish I would have taken a class like that at the beginning of my program so that I could learn how to dissect a scientific paper earlier on. The conversation we had a few weeks ago will stay with me for a really long time, thank you.

I cannot continue without thanking Carolina Lithgow-Bertelloni, for allowing me to finish and for providing me with unwavering support, you have been an incredible role model, and I am so glad that I have been able to reach out to you since we first met at Santa Barbara. The department as a whole has been an incredible support system and I could not have done this without the help of all the faculty and administration staff that answered any questions or provided guidance any time I showed up at your offices or ran into you in the hallway. Thank you Abby Kavner, Edwin

Schauble, Hilke Schlichting, Edward Young, Peng Ni, Kevin Coffey, Lingsen Meng, Jeana Drake, Caitlin Brown and all the staff (Nanette Capulong, Carlene Brown, Lauri Holbrook, Eric Wessenauer, Daniel Chung, Kelli Yang, Barbara Wasaka, Tasha Taylor and Brian Damiata!

I would also like to thank my collaborators, Elizabeth J. Catlos and Elizabeth A. Bell, who worked with me first-hand with on my first project and helped me understand so much of the instruments and the modeling we did. Huge thanks to Andrew Zuza, who offered to help with my second project and invited me to his lab to collect data. Thanks to Emily J. Chin, Danny Stockli, and Axel Schmidt, and collaborators at the Chinese Academy of Science for their help with dating rocks. Shout out to An's former students who offered to help and continue cheering us on, Paul Burgess, and special thanks to Michael Murphy and Paul Kapp for coming out to the field to collect samples with me last Thanksgiving weekend. John Cottle and Basil Tikoff, I could not have made it through the past few GSA's without your guidance and encouragement, thank you for all that you have done for me in the last ~7 years! To the mentors I have since I was at Cerritos College, Peter Moloney and Tor B. Lacy, thank you for pushing me to pursue a geology degree and for your ongoing support – I cannot believe we will be colleagues at Cerritos now. To my undergraduate researchers and anyone that came out to the field to help me carry rocks… you rock!

I want to give a simple, but loaded thank you to my friends, I am incredibly grateful to have shared this experience with you all for the memories we made along the way including book clubs, running group, baseball games, game nights, paint nights, beach trips, you were one of my lifelines.

Finally, I would like to thank my mom and dad for sacrificing so much to give me and my brothers everything they could and for supporting me throughout my entire academic career. I am incredibly humbled to be the first in my family to receive a doctorate degree and it could not have been possible without their help. Gracias por todo!

Curriculum Vita

Valeria Guadalupe Jaramillo Hernandez

EDUCATION

University of California, Los Angeles – MS in Geology

Department of Earth, Planetary, and Space Sciences – Advised by Professors Craig Manning and An Yin

University of California, Santa Barbara – BS in Geology

Department of Earth Science – Advised by Professor John Cottle and Thomas Alex Johnson, PhD

HONORS AND AWARDS

Certificate of Appreciation in recognition of outstanding contributions to the Geological Society of America Student Advisory Council

Invited On To the Future Mentor at GSA Connects, Pittsburg, PA

Excellence in Teaching and EPSS Outreach Departmental Awards

AGU Student Travel Grant

GSA Graduate Student Research Award

GSA Graduate Student Research Travel Award

UCSB Undergraduate Research Grant

GSA On to The Future Award

UCSB Outstanding Excellence and Outstanding Academic Achievement Award

PUBLICATIONS AND CONFERENCES

Jaramillo, V., Yin, A., Catlos, E.J., Bell. E.A., Schmidt, A. 2024. Root Problem of Mid-Tertiary Cordilleran Detachment Faults: Deciphering the evolution of the Whipple Mountains detachment shear zone in southeastern California. *Extensional Tectonics: Continental Breakup to Formation of Oceanic Basins - Volume 1.* AGU Books. *Accepted March 2024 – in press.*

……

Jaramillo, V., Catlos, E.J., Bell, E.A., Schmitt, A.K., Chin, E.J. Yin, A., Quantifying Pore- Fluid Pressure Ratios and Analyzing Deformation Mechanisms in the Whipple Mountains Brittle-Ductile Shear Zone. Talk presented at *Geological Society of America*. **18 October 2023**. 253-11.

Jaramillo, V., Catlos, E.J., Chin, E.J., Bell, E.A., Yin, A. Stockli, D., Schmitt, A.K. "Superposition of 80-55 Ma High P-T (0.7GPA/750C) Metamorphism by Mid-Tertiary Detachment Faulting in the Whipple Mountains, SE California. Talk presented at Geological Society of America. **12 October 2022**. 217-10,

Jaramillo, V., Catlos, E.J., Chin, E.J., Bell, E.A., Yin, A., Using Paleobarometry to Quantify Pore-fluid Pressure Ratios in Mid-crustal (15-25 km) Semi-Brittle Shear Zones. Poster presented at: *American Geophysical Union*. **13-17 December 2021**. T15F-02.

Jaramillo, V., Johnson, T.A., Cottle, J., Larson, K., Kylander-Clark, A., Insights into the Emplacement of the Kathmandu Klippe from Quartz Microstructures and Titanite Petrochronology. Talk presented at *Geological Society of America*. Talk presented **24 September 2019**. 217-5.

1 Introduction

It wasn't until the late 18th century that geology was established as a scientific discipline. James Hutton, the "father of geology", argued the Earth was much older than was widely accepted at the time (Hutton, 1788). The advent of radiometric dating in the early 20th century (e.g., Boltwood, 1907) further transformed geology by providing a method of calculating rock ages that extended Earth history to billions of years. James Hall (1882) introduced the hypothesis that down warping due to sediment deposition at continental margins leads to a 'crisis' that results in rapid uplift of mountain ranges. James Dana (1895) extended this idea that mountain ranges formed following the deposition of tens of thousands of feet of sediment which was followed by faulting to accommodate horizontal stresses ultimately driven by contraction due to crustal cooling. He referred to the general hypothesis as geosynclinal theory which became the de facto ruling hypothesis for the next 70 years (e.g., Knopf, 1948, 1960).

During this period, Alfred Wegener (1912, 1915) introduced the idea that the continents were once connected and had drifted apart into their present configuration. For example, he observed how South America and Africa would fit well together if the Atlantic Ocean were closed and how the same fossils could be found at similar reconstructed positions on opposing landmasses (Gregory, 1925). Despite this evidence, Wegener's ideas were largely ridiculed and his continental drift hypothesis ignored for the lack of a mechanism to explain this movement (e.g., van Waterschoot van der Gracht et al., 1928).

Despite its wide acceptance, geosynclinal 'theory' provided little quantitative understanding of the horizontal stresses or lateral pressure and vertical movement of these thick layers of deformed material. Abundant geomorphological evidence pointed to the idea that, in the

recent past, there were no high mountains and all of Earth's crust was close to sea level (Bucher, 1939). In turn, this suggested that this world-wide sediment deposition and peneplation reflected a process occurring throughout Earth and was progressing rapidly. Bucher (1939) proposed that the thick sediment loads were created during "diastolic" periods when the crust was expanding. These depressions would later be folded and thrusted creating mountain ranges during the "systolic" periods (i.e., when the crust was under compression; Bucher, 1939). The pulsation theory appeared to be supported by emerging data from the seafloor, earthquake records, topographic observations (Bucher, 1939), stratigraphic relations (Glassner and Teitchert, 1947) and isostasy (Knopf, 1948). Hall (1888) had concluded that folding of the crust occurred due to bending at the base of the geosynclines combined with igneous intrusions and metamorphism, both of which decrease in magnitude towards the shallow parts of the geosynclines (Glassner and Teitchert, 1947). Finally, these geosynclines were exhumed due to lateral pressure resulting in the folded and faulted mountain ranges we see at present (Knopf, 1948).

By the early 1960s, measurements from Cold War era magnetometers scanning the ocean floor and global seismometer networks that showed, respectively, symmetric magnetic stripes (Vine and Matthews, 1963) and earthquake activity that was localized in narrow belts supporting the continental drift model (Hess, 1954, 1962; Vine and Matthews, 1963). The discovery of seismically active narrow zones bounding land and ocean masses that are essentially inactive clearly showed that the outermost crustal layers are in constant movement relative to one another (e.g., Morgan, 1967). The recognition of seafloor spreading, lithospheric plates, and hot spots, which provided a mechanism that could explain Wegener's continental drift hypothesis, led to the theory of plate tectonics (Vine and Matthews, 1963; Wilson, 1963).

While this provided an immediate explanation for the distribution and interactions among oceanic plates, the implications of this new model to the evolution of continental crust were slower to develop. By the early 1970s, our understanding of the complexities involved when continental crust experiences plate tectonic forces began to be appreciated (e.g., Dewey and Bird, 1970). Of particular relevance to this thesis, by the late-1970s the North American Cordillera was recognized as hosting a suite of enigmatic metamorphic domes extending from Canada to northern Mexico (Davis and Coney, 1979; Coney, 1980; Crittenden et al., 1978). What became known as metamorphic core complexes consist of exhumed, Paleozoic, middle- to lower-crustal, mylonitic rocks overlain by unmetamorphosed Tertiary volcanic and/or sedimentary tilted strata that are separated by low-angle detachments, all evidence of continental extension (e.g., Coney, 1980; Lister and Davis, 1989). Two schools of thought arose. The first argued that mylonitization was Tertiary, detachment faulting was bi-directional, and pure-shear was the dominant extension mechanism (Davis and Coney, 1979; Davis et al., 2019). This second view (Davis and Lister, 1988) argued that mylonitization was Mesozoic, detachment faulting was uni-directional, and gravity sliding displaced allochthonous units (Davis et al., 1980). In the late 1980's, Professor An Yin began efforts to understand the origin of these low-angle normal faults and focused on the structural and stratigraphic development of the detachment fault in the adjacent Whipple and Chemehuevi mountains (Yin, 1989; Yin, 1991; Hacker et al. 1992; Yin and Dunn, 1992; Forshee and Yin, 1994). Thirty years later, I stand on the shoulders of the late Professor An Yin, who himself stood on the shoulders of the those that came before him, to refine and extend his thoughts and discoveries in the Whipple Mountains.

The first project in this dissertation provides an overview of the North American Cordilleran metamorphic core complex (MCC) belt. While data for MMC's in the northern and

central segments of the North American Cordillera is abundant, there has been a lack of data in the southern segment. This project highlights new pressure, temperature, and time constraints for the Whipple ductile shear zone. Until recently, shear zone development and exhumation were thought to be linked and Tertiary in age (Gans and Gentry, 2016; Howard and John, 1987; Spencer and Reynolds, 1990), however, the unexpected Late Cretaceous, monazite-in-garnet ages (this study) along with a Late Cretaceous metamorphic zircon population (Gans and Gentry, 2016) in the metamorphic core of the Whipple MCC raised questions about the timing of deformation. The second project consists of calculating pore-fluid pressure ratios at the brittle-ductile transition zone using the new P-T constraints. Under the assumption that at the brittle-ductile transition zone there should be evidence of simultaneous brittle and ductile deformation mechanisms (e.g., Noël et al., 2021) thus both deformation mechanisms should share the same state of stress, we can use this relationship to calculate the pore-fluid pressure ratio. The third project is development of a model to examine possible effects of a Late Cretaceous to Paleogene heating event on the deformation history of the Whipple Mountains shear zone. U-Pb zircon ages from previous studies record Late Cretaceous metamorphism that has not yet been explained (Gans and Gentry, 2016; Seymour et al., 2018). These U-Pb zircon ages together with monazite-in-garnet ages (this study) raise questions about the thermal history of the area that require addressing. These three projects build on each other to provide insights into the tectonometamorphic history and evolution of the Whipple Mountains shear zone. Together, they incrementally add to our ~240-year legacy of increased understanding of how our planet works and, more specifically, what happens when plate tectonics comes ashore.

1.1 References

Boltwood, B. (1907). On the ultimate disintegration products of the radioactive elements. Part II. The disintegration products of uranium. Am. J. Sci. 4, 77-80.

Bucher, W. H. (1939). Deformation of the Earth's Crust. *Bulletin of the Geological Society of America*, *50*(3), 421-432.

Coney, P. J., Jones, D. L., & Monger, J. W. (1980). Cordilleran suspect terranes. *Nature*, *288*(5789), 329-333.

Crittenden Jr, M., Coney, P. J., & Davis, G. (1978). Tectonic significance of metamorphic core complexes in the North American Cordillera. *Geology*, *6*(2), 79-80.

Davis, G. A., J. L. Anderson, E. G. Frost, and T. J. Shackelford (1980), Mylonitization and detachment faulting in the Whipple-Buckskin-Rawhide Mountains terrane, southeastern California and western Arizona, Geol. Soc. Am. Mem., 153,79–130.

Davis, G. A., & Lister, G. S. (1988). Detachment faulting in continental extension: Perspectives from the southwestern US Cordillera. Processes in continental lithospheric deformation: Geological Society of America Special Paper, 218, 133-159.

Davis, G. H., & Coney, P. J. (1979). Geologic development of the Cordilleran metamorphic core complexes. *Geology*, *7*(3), 120-124.

Davis, G. H. (1980). Structural characteristics of metamorphic core complexes, southern Arizona. Cordilleran metamorphic core complexes: Geological Society of America Memoir, 153, 35-77.

Dewey, J.F. and Bird, J.M. (1970). Mountain belts and the new global tectonics. *Journal of geophysical Research*, *75*, 2625-2647.

Forshee, E. J., & Yin, A. (1994). Evolution of monolithological breccia deposits in supradetachment basins, Whipple Mountains, California. *Basin Research*, *7*(2), 181-197.

Gans, P. B., & Gentry, B. J. (2016). Dike emplacement, footwall rotation, and the transition from magmatic to tectonic extension in the Whipple Mountains metamorphic core complex, southeastern California. *Tectonics*, *35*(11), 2564-2608.

Glaessner, M. F., & Teichert, C. (1947). Geosynclines, a fundamental concept in geology. *American Journal of Science*, *245*(8), 465-482.

Gregory, J. W. (1925). The Origin of Continents and Oceans.

Hacker, B. R., Yin, A., Christie, J. M., & Davis, G. A. (1992). Stress magnitude, strain rate, and rheology of extended middle continental crust inferred from quartz grain sizes in the Whipple Mountains, California. Tectonics, 11(1), 36-46.

Hall, J. (1882). *Contributions to the Geological History of the American Continent.* Salem Press. 71 p.

Hall, J. (1852). *Paleontology of New York; Vol. 6*. C. van Benthuysen.

Hess, H. H. (1954). Geological hypotheses and the earth's crust under the oceans. *Proceedings of the Royal Society of London. Series A, Mathematical and Physical Sciences*, 341-348.

Hess, H. H. (1962). History of ocean basins.

Howard, K. A., & John, B. E. (1987). Crustal extension along a rooted system of imbricate low-angle faults: Colorado River extensional corridor, California and Arizona. Geological Society, London, Special Publications, 28(1), 299-311.

Hutton, J. (1788). X. Theory of the Earth; or an Investigation of the Laws observable in the Composition, Dissolution, and Restoration of Land upon the Globe. *Earth and Environmental Science Transactions of The Royal Society of Edinburgh*, *1*(2), 209-304.

Knopf, A. (1948). The geosynclinal theory. *Geological Society of America Bulletin*, *59*(7), 649-670.

Knopf, A. (1960). Analysis of some recent geosynclinal theory. *American Journal of Science*, *258*, 126-136.

Lister, G. S., & Davis, G. A. (1989). The origin of metamorphic core complexes and detachment faults formed during Tertiary continental extension in the northern Colorado River region, USA. *Journal of Structural Geology*, *11*(1-2), 65-94.

Morgan, W. J. (1968). Rises, trenches, great faults, and crustal blocks. *Journal of Geophysical Research*, *73*(6), 1959-1982.

Noël, C., Passelègue, F. X., & Violay, M. (2021). Brittle faulting of ductile rock induced by pore fluid pressure build-up. *Journal of Geophysical Research: Solid Earth*, *126*(3), e2020JB021331.

Seymour, N. M., Strickland, E. D., Singleton, J. S., Stockli, D. F., & Wong, M. S. (2018). Laramide subduction and metamorphism of the Orocopia Schist, northern Plomosa Mountains, west-central Arizona: Insights from zircon U-Pb geochronology. *Geology*, *46*(10), 847-850.

Spencer, J. E., & Reynolds, S. J. (1990). Relationship between Mesozoic and Cenozoic tectonic features in west central Arizona and adjacent southeastern California. *Journal of Geophysical Research: Solid Earth*, *95*(B1), 539-555.

van Waterschoot, W. A. J. M., & der Gracht, V. (1928). *Theory of Continental Drift; a Symposium on the Origin and Movement of Land Masses, Both Inter-continental and Intra-continental, as Proposed by Alfred Wegener*. American Association of Petroleum Geologists.

Vine, F. J., & Matthews, D. H. (1963). *Magnetic anomalies over oceanic ridges*. Nature Publishing.

Wilson, J. T. (1963). Continental drift. *Scientific American*, *208*(4), 86-103.

Yin, A. (1989). Origin of regional, rooted low-angle normal faults: A mechanical model and its tectonic implications. *Tectonics*, *8*(3), 469-482.

Yin, A. (1991). Mechanisms for the formation of domal and basinal detachment faults: A three-dimensional analysis. *Journal of Geophysical Research: Solid Earth*, *96*(B9), 14577-14594.

Yin, A., & Dunn, J. F. (1992). Structural and stratigraphic development of the Whipple-Chemehuevi detachment fault system, southeastern California: Implications for the geometrical evolution of domal and basinal low-angle normal faults. *Geological Society of America Bulletin*, *104*(6), 659-674.

2 Root Problem of Mid-Tertiary Cordilleran Detachment Faults: Deciphering the Evolution of the Whipple Mountains Detachment Shear Zone in Southeastern California

Note: This chapter is modified from **Jaramillo, V**., Yin, A., Catlos, E.J., Bell. E.A., Schmidt, A. 2024. Root Problem of Mid-Tertiary Cordilleran Detachment Faults: Deciphering the evolution of the Whipple Mountains detachment shear zone in southeastern California. *Extensional Tectonics: Continental Breakup to Formation of Oceanic Basins - Volume 1.* AGU Books. *Accepted March 2024 – in press.*

2.1 Abstract

The North American Cordilleran metamorphic core-complex belt provides insight into the tectonometamorphic evolution of North America. Garnet-bearing assemblages have been used to generate pressure-temperature (P-T) constraints on the metamorphic history in its northern and central segments. Such datasets are scarce in its southern segment. We review existing metamorphic conditions and timing for these core complexes. Conditions from the Whipple detachment shear zone in southeastern California were also ascertained using conventional and isopleth thermobarometry. A sample from the easternmost Whipple Mountains shows monazite in reaction with allanite trapped in garnet. The monazite was dated in situ using an ion microprobe and yielded 62 ± 9 Ma, 67 ± 7 Ma, and 80 ± 6 Ma (Th-Pb dates, ±1σ). P-T conditions recorded by garnet and matrix minerals from an adjacent rock are high-grade (rim, 680–750 °C and 7–9.4 kbar; core, 750–800 °C and 6.2–7.8 kbar). The results suggest exhumation from depths deeper than previously thought. With this new information, a new P-T-t path may be established for the rocks in the Whipple detachment and may suggest a deeper initiation or multiple metamorphic events not previously analyzed.

2.2 Introduction

The North American Cordillera hosts a suite of metamorphic core complexes that extend from Canada to northern Mexico (Figures 2.1–2.3) (Armstrong, 1982). The orogenic nature of the North American Cordillera Anatectic Belt provides insights into the interaction between plutons, metamorphosed country rocks, and tectonics (Coney et al., 1980; Armstrong, 1982; Chapman et al., 2021). The various competing models for the initiation, style, and kinematic evolution of detachment-fault systems 2.4) make testable predictions on the pressure-temperature-time (P-T-t) paths, timing and duration of faulting, and structural associations requiring specific fault geometry and kinematics can be tested by using field-based investigations coupled with geochemical and geochronological analytical methods.

In this chapter, we review existing P-T-t data from the North American Cordilleran metamorphic core complexes (Table 2.1; Figure 2.1). Core-complex extension and timing of metamorphism are well-constrained in the northern and central segments of the North American Cordillera; however, the southern segment lacks this data (Table 2.1; Chapman et al., 2021). One core complex in particular, the Whipple Mountains, contains amenable assemblages for P-T-t determinations. The Whipple detachment fault system consists of a regionally extensive detachment fault (the Whipple detachment fault; Dickey et al., 1980), a metamorphic footwall, and a highly extended hanging wall (Davis et al., 1980, 1982; Davis, 1988; Figure 2.3). The Whipple mylonitic shear zone is capped by the Whipple detachment fault on top without exposing its base (Davis et al., 1980, 1982). The Whipple detachment fault system has been studied extensively, yet how the detachment roots into the crust is poorly understood (Behr & Platt, 2011; Gans & Gentry, 2016; Axen, 2020). Here we present newly acquired P-T-t data from a rock from the mid-Tertiary Whipple detachment shear zone in the Whipple Mountains core complex. Thermodynamic modeling of garnet-bearing

rocks allows for the acquisition of precise and reliable metamorphic records (de Capitani & Petrakakis, 2010; Moynihan & Pattison, 2013; Gaidies et al., 2008), including those exposed in extended terranes (Etzel et al., 2019; Etzel & Catlos, 2021). The objectives of this chapter are to highlight the lack of such data in the southern North American Cordillera metamorphic core complexes and to present a petrochronological approach to developing P-T-t data in the Whipple Mountains using thermodynamic modeling of garnet-bearing rocks and in situ (in thin section) monazite geochronology.

2.3 Geologic and Regional Background

2.3.1 Problems and Models for Continental Extension in North America

Continental extension is an integral part of plate tectonics, in part because of its role in the spatiotemporal transition from continental rifting to mid-ocean-ridge spreading, leading to the creation of new oceanic lithosphere (e.g., Wilson, 1966; Sleep, 1971; Lister et al., 1986; Hempton, 1987; White & McKenzie, 1989; Bosworth et al., 2005; Brothers et al., 2009). In addition, continental extension is a crucial stage of mountain building expressed by topographic collapse (Molnar & Tapponnier, 1978; Coney & Harms, 1984; Dewey, 1988), typically accommodated by distributed intraplate deformation (e.g., Molnar & Tapponnier, 1975; Atwater & Stock, 1998). Despite its importance, how continental extension operates in the ductile middle and lower crust remains poorly understood. This issue is well illustrated by the debate on how the brittle detachment faults extend downward into the deeper ductile crust during the development of the ~2,000-km-long and 100–200-km-wide mid-Tertiary North American metamorphic core complexes (Figure 2.1).

Low-angle detachment faulting is a global phenomenon documented in the North American Cordillera and many other parts of the world (Davis & Coney, 1979; Çemen et al., 2006; Coney et

al., 1980; Whitney et al., 2013; Gibbs, 1984; Lister et al., 1984; Morley, 1989; Lister et al., 1991; Harrison et al., 1995; Reston et al., 1996; Davis, 1996; Gessner et al., 2001; Murphy et al., 2002; McNulty & Farber, 2002; Robinson et al., 2004; Kapp et al., 2000, 2008; Chen et al., 2013; Worthington et al., 2020). However, despite its wide occurrence, the mechanical origin of low-angle detachment faults with their average dip in the upper crust at ~30° or lower is poorly understood. Specifically, it is unclear whether subhorizontal midcrustal flow (Yin, 1989; Melosh, 1990; Westaway, 1999), thermally triggered gravitational spreading (Coney & Harms, 1984; Coney, 1987), fault-zone mechanics (Axen, 1992, 2004; Axen & Selverstone, 1994; Selverstone et al., 2012), or crustal-scale anisotropies (Axen, 2020) has played a controlling role in initiating regionally extensive, crustal-scale, low-angle extensional detachment faults.

Figure 2.4 illustrates competing detachment-fault models. Differentiating which applies to the Cordilleran metamorphic core complexes is difficult because these conceptual kinematic models are qualitative, and their space-time predictions of fault-system evolution are ambiguous. Figure 2.4a predicts that the mid-Tertiary Cordilleran detachment faults become horizontal decollement zones along the base of the upper crust (Miller et al., 1983; Gans et al., 1985; Lee et al., 2017). Figure 2.4b suggests that these faults flatten into midcrustal ductile-shear zones (Davis et al., 1986; Wernicke & Axen, 1988; Lister & Davis, 1989; Cooper et al., 2017; Lutz et al., 2021). Alternatively, Figure 2.4c shows that they cut obliquely across the entire lithosphere (Wernicke, 1985). Differentiating these models assesses whether extensional detachment faulting occurs under normal or abnormal continental-strength-profile conditions (Behr & Platt, 2011; Brun et al., 2018). The abnormal strength profile assumes an inviscid-fluid lower crust (Wernicke, 1995; Kohlstedt et al., 1995; Brun et al., 2018).

These proposed models facilitate our understanding of the fundamental mechanisms controlling continental extension. Several studies used numerical simulations assuming realistic continental thermal conditions and using laboratory-determined rheological parameters to understand their feasibility and applicability to the North American Cordillera. This class of research has been focused on whether the style of detachment faulting depends on the boundary and thermal conditions of a continental extensional system (e.g., Buck, 1991; Rey et al., 2009) or lithospheric rheology (e.g., Lavier & Manatschal, 2006; Gueydan et al., 2008; Korchinski et al., 2018). Some suggest the presence of partial crustal melting (Rey et al., 2009; Schenker et al., 2012) or lateral crustal heterogeneities in mechanical properties (e.g., Huet et al., 2011). The variability of Moho morphologies has been explored (Wu et al., 2015), as has crustal-density distributions (e.g., Tirel et al., 2008; Korchinski et al., 2018). The potential for lower-crustal flow (Block & Royden, 1990; Rey et al., 2011) and the impact of rift-basin sedimentation are also concerns (Korchinski et al., 2021). Overall, the formation of low-angle detachment faults could have been induced by diverse geodynamic processes involving various thermal, rheological, and mechanical parameters.

2.3.2 North American Cordillera Metamorphic Core Complexes

The North American Cordilleran orogen occupies a ~5,000-km-long section of the larger circum-Pacific orogenic belt (Figure 2.1; e.g., Dickinson et al., 2009). The mid-Tertiary (ca. 45–10 Ma) Cordilleran metamorphic core-complex belt extending from southern Canada to northern Mexico is part of the North American Cordilleran orogen (Davis & Coney, 1979; Coney et al., 1980). The core-complex belt consists of about 25 individual metamorphic complexes that can be divided into the northern, central, and southern segments (Table 2.1; Coney et al., 1980; Wernicke et al., 1987; Dickinson, 2004; Hildebrand, 2013; Cassel et al., 2018; Chapman et al., 2021).

The fundamental structural association of a metamorphic core complex consists of a low-angle decollement associated with mylonitic fabrics that separate a metamorphic basement in the footwall and unmetamorphosed cover rocks in the hanging wall (Figure 2.4; e.g., Coney et al., 1980; Armstrong, 1982; Brun et al., 2018). These complexes are characterized by their uplifted, dome-like detachments and metamorphic and plutonic basement rocks that are overprinted by low-dipping, lineated, and foliated mylonitic gneisses. The crystalline basement rocks are separated from the overlying, unmetamorphosed, faulted, and tilted younger strata by a subhorizontal detachment fault (Coney et al., 1980; Çemen et al., 2006; Gans & Gentry, 2016; Brun et al., 2018). The core-complex belt coincides with the root zone of the Mesozoic Cordilleran thrust belt that had a crustal thickness of 40–65 km (Coney & Harms, 1984; Chapman et al., 2015, 2020; Zuza et al., 2021), a Late Cretaceous anatectic plutonic belt that is characterized by the lack of an extrusive counterpart (Miller & Bradfish, 1980; Chapman et al., 2021), and local sites of Late Cretaceous to Paleogene metamorphism (Miller & Gans, 1989; Cooper et al., 2010; Levy et al., 2021), all in the hinterland of the Cordilleran orogen between the Cordilleran Mesozoic magmatic arc in the west and the Cordilleran Mesozoic foreland fold-thrust belt in the east (Chapman et al., 2021; Figure 2.1). Mesozoic metamorphic rocks and anatectic plutons are exposed in the footwalls of major detachment faults associated with the Cordilleran metamorphic core complexes (e.g., Anderson et al., 1988; Miller & Gans, 1989; John & Wooden, 1990; Anderson and Cullers, 1990; Zuza et al., 2021). The Cordilleran Anatectic Belt is dominated by peraluminous granitoids from partial melting of the North American crust at 675–775 °C induced by decompression, crustal thickening, fluid fluxing, or increased heat flux from the mantle (Miller & Bradfish, 1980; Anderson & Cullers, 1990; John & Wooden, 1990; Chapman et al., 2020; Chapman et al., 2021).

2.3.3 Metamorphic Core Complexes in the Southern Segment

The southern segment of the North American Cordilleran core-complex belt hosts metamorphic complexes in California, Arizona, and northern Mexico (Figure 2.2; Table 2.1). This southern segment also hosts the lower Colorado River extensional corridor, a 400-km-long section of east- and northeast-dipping extensional faults between Las Vegas, NV, and Phoenix, AZ (Spencer et al., 2018). Detachment surfaces characteristic of metamorphic core complexes here may record extension direction in the brittle hanging wall and mylonitic footwall rocks (Axen, 2020). Typical hanging-wall rocks include sedimentary or metasedimentary rocks (Buckskin-Rawhide, Whipple Mountains, Plomosa, Pinaleno) or volcanic flows (Harquahala, Whipple Mountains, Harcuvar, Picacho) (Prior et al., 2016; Gottardi et al., 2018; Strickland et al., 2018; Scoggin, 2022; Singleton et al., 2022). Most of the metamorphic core complexes in eastern California and western Arizona record NE-directed hanging-wall displacement during early Oligocene-Miocene exhumation, whereas core complexes further east record SW-directed hanging-wall displacement (Reynolds & Spencer, 1985; Dickinson et al., 1987; Spencer, 2006). In southern Arizona and northern Mexico, the transport direction of the hanging-wall rocks along the detachment faults is consistently southwestward except for the NNE-directed detachment faults in the Coyote, Pinaleno, Alvarez, Mezquital, and Tubutama core complexes (Figure 2.2; Dickinson et al., 1982; Reynolds & Spencer, 1985; Spencer, 2006).

A 70- to 100-km-wide region of extended crust from southern Nevada, eastern California, and western Arizona (Faulds et al., 2001) provides insights into the evolution of Miocene extension in the area (Howard & John, 1987; Davis, 1988; Davis & Lister, 1988; Lister & Davis, 1989). The region forms part of the southern Cordillera core-complex belt, and the onset of extension along the corridor is constrained to occur between 26–22 Ma in the south to 20–18 Ma in the north

(Foster & John, 1999; Spencer et al., 2018; Strickland et al., 2018). The extensional corridor partially overlaps the Big Maria fold-and-thrust belt (Spencer & Reynolds, 1990) and locally exposes the Orocopia schist in a few detachment-fault footwalls (Haxel et al., 2015; Jacobson et al., 2017; Seymour et al., 2018; Strickland et al., 2018). This schist consists of quartzofeldspathic, metachert (Fe- and Mn-bearing quartz), and metabasite (metabasalt), with pods of actinolite, talc, and serpentinite (Strickland et al., 2018).

The exposure of Orocopia schist in the extensional corridor has been associated with Miocene detachment faulting (e.g., Jacobson et al., 2017; Strickland et al., 2018). However, the mechanism for predetachment emplacement of the schist in the middle crust during the flat-subduction Laramide orogeny (Dickinson et al., 1978) has been attributed to eastward displacement of the lower crust and/or the mantle lithosphere of the North American plate accompanied by basal accretion of the subducted mélange complex and forearc-basin strata below the North American middle crust or the tectonically eroded/thinned North American mantle lithosphere (see Bird, 1988; Livaccari & Perry, 1993; Yin et al., 2002; Chapman, 2017; Ducea & Chapman, 2018; Axen et al., 2018; Figure 2.5a). Alternatively, the corridor may be the result of ductile injection of subducted mélange complex and forearc-basin strata as a sheet into the North American middle crust (Strickland et al., 2018; Figure 2.5b). A model of diapiric intrusion of the subduction mélange complex and forearc-basin strata has also been proposed (Figure 2.5c; Chapman et al., 2021).

The role of oceanic plateau subduction has also been invoked as the cause of Laramide flat subduction (Livaccari et al., 1981; Saleeby, 2003; Chapman, 2017). East-west extension along the axis of the Mesozoic U.S. Cordilleran orogen may have occurred immediately before (late Cretaceous) or during the flat slab subduction (Jacobson et al., 1996; Saleeby, 2003; Wells & Hoisch, 2008; Chapman et al., 2020). The cause of this extensional event has been attributed to

partial mantle-lithospheric delamination of the North American plate (Wells & Hoisch, 2008; Wells et al., 2012; Chapman et al., 2020).

A consistent finding of the exhumed Orocopia schist against the San Andreas fault in the west and those exposed in the lower Colorado River extensional corridor in the east is the presence of 65–40 Ma metamorphic zircons (Grove et al., 2003; Jacobson et al., 2017; Seymour et al., 2018). Paleogene zircon growth implies that the schist remained under amphibolite facies conditions long after underplating. The persistent heating of the schist during flat subduction is counterintuitive as the process would have exerted a refrigeration effect that cooled the overriding plate materials (Dumitru et al., 1991). The schist's unexpected and sustained Paleogene heating has been attributed to frictional heating (Jacobson et al., 2017) or extensional tectonics (Seymour et al., 2018) during the Laramide flat subduction.

2.3.4 P-T Conditions of Core-Complex Development

Although P-T constraints exist for the peak metamorphic conditions for rocks exposed in the northern segment of the North America Cordillera, conditions in the southern segment remain poorly constrained (see also Chapman et al., 2021). Table 2.1 lists the approaches to generate these conditions, which have primarily focused on applying classic thermobarometric techniques to garnet-bearing rocks, relying on exchange thermometry and net-transfer barometry.

Metamorphic core complexes in British Columbia and Washington (Figure 2.1), record peak conditions of 5–12 kbar and 700–850 °C (see Table 2.1 for references). The Frenchman's Cap metamorphic core complex records the highest conditions in the North American Cordillera of 10–12 kbar at 800 °C, whereas the Okanogan Complex records 9–10 kbar and 700–850 °C (Hansen & Goodge, 1988; Armstrong & Ward, 1991; Carlson et al., 1991; Crowley et al., 2001; Crowley et al., 2008; Kruckenberg et al., 2008; Chapman et al., 2021).

Those in the central segment from Idaho to southern Nevada record between 4–11 kbar and 500–800 °C. The lowest P recorded in this central region is in the Pioneer Mountains in Idaho at 4 kbar from the Pioneer Intrusive Suite (Silverberg, 1990; Vogl et al., 2012; Chapman et al., 2021). Estimates from the Ruby-E Humboldt complex in Nevada are 8–10 kbar and 700–800 °C using garnet rim thermobarometry with matrix minerals on pelitic samples (Hodges et al., 1992; McGrew & Snee 1994; Lee et al., 2003; Howard et al., 2011).

In contrast to the northern segment of the North American Cordillera, peak P-T conditions of the southernmost metamorphic core complexes are not clearly constrained. Foster (1989) suggests that the emplacement of the Old Woman–Piute batholith in the Old Woman Mountains, CA, triggered high-grade metamorphism and reports estimates of 3.5–4.5 kbar and 530 °C to >650 °C. Analysis of rocks from the Coyote core complex in Arizona yield 450 ± 50 °C at <5 kbar (Wright & Haxel, 1982; Gottardi et al., 2020). Recent thermobarometric studies on the Plomosa core complex (Arizona) suggest that the rocks may have reached 6 kbar and between 549 and 590 °C (Spencer et al., 2018; Singleton et al., 2022).

Core complexes may record metamorphism due to pluton emplacement or mylonitization (Anderson, 1988). For example, the Catalina, Tortolita, and Pinaleno plutons are suggested to be related to thermal conditions that range between ~650 and 800 °C (Long et al., 1995; Fayon et al., 2000; Wong and Gans, 2008). The Picacho core complex records mylonitization T in the range of 300–630 °C and the Mazatan core complex between 300 and 450 °C (Terrien, 2012; Fornash et al., 2013; Peterman et al., 2014; Schaper, 2016; Gottardi et al., 2018; Davis et al., 2019; Ducea et al., 2020). Studies from core complexes in northern Mexico, closest to the border with Arizona, indicate metamorphism at greenschist- to lower-amphibolite facies, amphibolite facies, and/or upper-amphibolite facies (Anderson et al., 1988; Goodwin and Haxel, 1990; Nourse et al., 1994;

Mallery et al., 2018). The Puerta del Sol core complex in northern Mexico reached 900 °C (Wong and Gans, 2008; Gonzalez-Becuar et al., 2017).

2.4 Whipple Detachment Fault System

The crustal thickness in the Whipple Mountains area is 26–28 km, and the lower-crust seismic velocity is consistent with a felsic composition (McCarthy et al., 1991). The Whipple Mountains and neighboring regions lack the Paleozoic strata as Tertiary volcanic and sedimentary strata lie on top of Precambrian metamorphic-basement rocks (e.g., Dickey et al., 1980; Stone et al., 1983). Spencer and Reynolds (1990) attributed the absence of Neoproterozoic-Paleozoic strata to Mesozoic crustal shortening in the region. The occurrence of Paleogene gravel deposits in an eastward-flowing drainage system (Young, 1982; Elston & Young, 1991) in the western Colorado Plateau requires a higher elevation and thicker crust in the Whipple Mountains than that of the Colorado Plateau immediately before the onset of Whipple detachment faulting. Seismic and experimental data suggest a 40–48 km crustal thickness near the Four Corners region compared to ~35 km thickness at the southern Basin and Range region (Hauser & Lundy, 1989; Bailey et al., 2012). Because the current crustal thickness of the western Colorado Plateau is ~45 km (Hauser & Lundy, 1989; Bailey et al., 2012), the higher elevation of the Whipple Mountains compared to that of the western Colorado Plateau in the Paleogene implies that the preextension Whipple crust was >45 km. Comparing the current crustal thickness (26–28 km) requires ~50% of post-Paleogene crustal extension in the Whipple Mountains area.

2.4.1 Footwall Rocks

Like all core complexes in the North American Cordilleran orogen, the Whipple detachment fault system consists of a regionally extensive detachment fault (the Whipple detachment fault, Dickey et al., 1980), a metamorphic footwall, and a highly extended hanging wall (Davis et al., 1980,

1982; Davis, 1988; Figure 2.3). The Whipple mylonitic shear zone is capped by the Whipple detachment fault on top without exposing its base, and a cross-section projection requires the shear zone to be >3.9 km thick (Davis et al., 1980, 1982). Foliation surfaces in the mylonitic shear zone are domal-shaped, expressed by a radially dipping direction from the center of the mountains; this shape mimics the geometry of the overlying Whipple detachment fault (Davis, 1988). Both the mylonitic and non mylonitic metamorphic rocks in the footwall are composed of Proterozoic gneisses (1.4–1.2 Ga) intruded by mylonitic and nonmylonitic Cretaceous and Miocene plutons/dikes/sills (Anderson & Rowley, 1981; Anderson et al., 1988; Anderson & Cullers, 1990; Gans & Gentry, 2016). The host rocks of the Mesozoic-Cenozoic intrusions in the footwall are gneisses, which are composed of interlayered amphibolite, garnet-muscovite gneiss and schist, and aluminosilicate with kyanite exposed at deeper structural levels and sillimanite at higher structural levels in the mylonitic shear zone (Anderson & Cullers, 1990). The metamorphic units are locally associated with migmatites, whereas the plutons are associated with aplite sills and dikes (Anderson & Rowley, 1981; Anderson & Cullers, 1990).

Oxygen isotopes, whole-rock major and trace element compositions, and petrological studies indicate that the Whipple mylonitic rocks experienced two episodes of hydrothermal alteration: a high-T (>~600 °C) episode involving a metamorphic or magmatic fluid and a low-T (~350 °C) episode involving meteoric fluids (Morrison, 1994; Table 2.1). Interestingly, footwall intrusions show a progressive decrease in their emplacement depths with time. Granite was emplaced at a depth of 33 ± 4 km at 89 ± 3 Ma, at 29 ± 1 km at 73 ± 3 Ma (Figure 2.6). Evidence exists for dike emplacement at a depth of ~16 km at 26 Ma and additional granites and dikes at 5–6 km at 19-17 Ma (Figure 2.6; Anderson et al., 1988; Anderson & Cullers, 1990).

Crystal-plastically deformed quartz veins in the Whipple mylonitic shear zone were used to estimate the magnitude of differential stresses during the ductile-shear deformation (Hacker et al., 1992). Their samples were collected at the two sites, with one directly below the Whipple detachment fault in the east and another directly below the Whipple mylonitic front in the west (Figure 2.3). Using grain-size piezometers and kinetic laws of thermally activated grain growth, the grain-size cluster at 32–61 μm and the cooling history of the Whipple shear zone require the formation of the mylonitic veins under ~40–150 MPa of differential stresses. The cooling history used in Hacker et al. (1992) for grain-growth calculations was obtained from the work of Anderson et al. (1988), assuming the entire mylonitic shear zone was created in the Miocene during Whipple detachment faulting.

Using updated grain-size piezometers coupled with Ti-in-quartz thermometry, Behr and Platt (2011) estimated 0.10–1.40 kbar of differential stresses over a T range of 310–550 °C from multiphase mylonitic-pluton samples across the Whipple shear zone. Their estimated stress magnitudes did not consider the grain-growth effect during post-deformation annealing (cf., Hacker et al., 1992). In addition, the potential pinning effect on quartz grain deformation and growth (Evans et al., 2001; Hiraga et al., 2010; Cross et al., 2015; Tasaka et al., 2017) was not considered. Because the timing of the measured paleo-stress magnitudes is unknown, the question remains of whether the apparent T-dependent stress magnitudes across the Whipple shear zone indicate a vertical stress profile at a particular geologic time or a composite section that different stress magnitudes related to different geologic events. Furthermore, independent P estimates under which their samples were mylonitized have not been reported.

The west-dipping, transitional boundary between mylonitized and nonmylonitized metamorphic rocks in the footwall is referred to as the “mylonitic front” by Davis et al. (1980, 1982) and Davis

(1988). This dipping contact was extrapolated westward to a depth of ~15 km based on analyzing and interpreting a seismic-reflection profile across the western Whipple Mountains (Flueh & Okaya, 1989). The Whipple shear zone imaged by seismic-reflection surveys is ca. 15 km thick above a low-reflectivity and higher seismic-velocity region in the lower crust (Henyey et al., 1987; Flueh & Okaya, 1989).

The cooling history of the Whipple footwall rocks was constrained by a 40Ar/39Ar hornblende age at ~20 Ma (DeWitt et al., 1986) and an eastward younging trend in the minimum 40Ar/39Ar K-feldspar ages from ~21 to ~15 Ma across the footwall (Foster & John, 1999). Apatite (U–Th)/He ages from the Whipple footwall rocks are 26.6 ± 1.1 Ma to 13.7 ± 0.4 Ma, and zircon (U–Th)/He ages are 46.8 ± 1.2 Ma to 13.6 ± 0.3 Ma, with an inflection point at 21.5 ± 1.0 Ma (Stockli et al., 2006).

2.4.2 Whipple Detachment Fault and Mylonitic Shear Zone

Although motion along low-angle (dip <30°) normal faults requires fault-zone weakening (e.g., Axen, 1992, 2004, 2007), patterns of syn-detachment brittle structures directly below the Whipple detachment fault are interpreted to indicate a normal coefficient of static friction and a nearly hydrostatic pore-fluid P at the time of fault motion (Axen & Selverstone, 1994; Axen et al., 2015). The Whipple fault zone consists of an alteration-induced assemblage of secondary epidote + titanite + chlorite, + calcite + feldspar formed during the terminal phase of mylonitization and cataclasis at 380–420 °C (Selverstone et al., 2012). Fluid-inclusion studies of the Whipple fault-zone rocks show that its pore-fluid P may have evolved from having a lithostatic value below and a hydrostatic value above a depth of ~10 km during its development (Selverstone et al., 2012). Oxygen isotope compositions of epidote and quartz in the Whipple fault-zone breccias require an extreme thermal gradient of 82 °C over 38 m (2,160 °C/kilometer) across the fault from the

footwall to the hanging wall, interpreted as a result of fluid-induced fault-zone refrigeration (Morrison & Anderson, 1998). The thermal gradient was determined by analyzing quartz-epidote samples and calculating the δ18O of quartz and epidote, which yield a linear relationship between the values and temperature; in this case, a steep slope represents equilibrium exchange among the two minerals, which suggests that hydrothermal fluid interaction occurred readily in the system (Matthews, 1994; Morrison & Anderson, 1998).

The Whipple mylonitic shear zone is >3.9 km thick (Davis et al., 1980) and lies directly below the Whipple detachment fault in the eastern Whipple Mountains (Figure 2.3). To the west, the mylonitic shear zone and nonmylonitic footwall metamorphic rocks are separated by a west-dipping, transitional boundary that was termed the Whipple mylonitic front (Davis et al., 1980, 1982; Davis, 1988; Anderson & Cullers, 1990). The mylonitic front is locally cut across by the ~8-km-wide, NNW-trending, 21–18 Ma Chambers Well dike swarm. Detailed mapping by Gans and Gentry (2016; (see their figure) shows that the dikes have variable northeasterly dips from 20° to 80°. The Whipple detachment truncates the Chambers Well dike swarm and its country metamorphic rocks (Davis et al., 1980, 1982; Davis, 1988; Anderson & Cullers, 1990). Their hanging-wall counterpart is interpreted to have been offset for ~ 40 km to the east (Howard et al., 1982, 1999).

2.4.3 Hanging-Wall Rocks of the Whipple Detachment Fault

The hanging wall of the Whipple detachment fault consists of Precambrian basement rocks overlain by mid-Tertiary sedimentary and volcanic strata (Davis et al., 1980, 1982; Davis, 1988). The basement rocks are dominantly banded quartzofeldspathic gneisses interlayered with amphibolite (Anderson & Cullers, 1990). The mid-Tertiary strata in the Whipple Mountains and the neighboring core complexes are 22–12 Ma syn-extension basin fills (Miller & John, 1988,

1999; Nielson & Beratan, 1990, 1995; Beratan, 1991; Fedo & Miller, 1992; Dorsey & Becker, 1995; Faulds et al., 2001; Prior et al., 2018; Spencer et al., 2018). Tertiary strata in the Whipple Mountains consist of four units (Nelson & Beratan, 1990). Unit 1 is the oldest on top of the basement rocks, and its ages range from 23 ± 2.4 Ma (zircon fission track ages) to 18.5 ± 0.5 Ma (40Ar/39Ar sanidine ages of the Peach Springs Tuff) (Beratan, 1991; Kuniyoshi & Freeman, 1974). The unit is dominated by mafic to intermediate volcanic rocks. Unit 2 consists of the regionally extensive 18.5 Ma Peach Springs Tuff. Unit 3 is equivalent to the Copper Basin Formation (Davis et al., 1980), which is composed of sedimentary strata, limestone, and minor basalt. Unit 4 is the youngest unit characterized by a bimodal suite of mostly flat-lying basaltic and rhyolitic flows with ages from 12.2 Ma (K-Ar, sanidine) to 8.6 Ma (K-Ar, whole rock) (Nielson & Beratan, 1990; Suneson & Lucchitta, 1983). The age was determined by K-Ar, whole-rock dating of one of the basalt flows (Kuniyoshi & Freeman, 1974). The sedimentology and growth-strata relationship of the mid-Tertiary strata in the northeastern Whipple Mountains were examined by Dorsey and Becker (1995). These authors show southward thickening and downward steepening of a syn-extensional sequence that was deposited before 18.5 Ma and lasted until at least ~14.5 Ma.

2.4.4 Methods

We conducted geological mapping and sampling along two traverses across the Whipple mylonitic shear zone (Figures 2.3, 2.7, and 2.8). Three samples (nomenclature of VJ-date-number) were collected at different structural levels along the Whipple ductile-shear zone (Table 2.2). Thin sections of each sample were analyzed for mineral identification and textural relationships using a petrographic microscope (Figure 2.9). Bulk rock compositions of each sample (Table 2.2) were obtained from rock chips using inductively coupled plasma (ICP) mass spectrometry at Activation

Laboratories Ltd. (Table 2.2). Elemental distributions in Mn, Mg, Ca, and Fe of each thin section were mapped using the JEOL 8200 microprobe (EMP), which is part of the Geomaterials Characterization and Imaging Facility at the Department of Earth and Planetary Sciences at the University of Texas at Austin. The X-ray maps were used to determine where garnet and matrix mineral compositions (plagioclase, biotite, chlorite, and muscovite) were obtained using the electron microprobe (Figure 2.10). All compositional data and X-ray element maps are available in the data repository.

Conventional and isochemical phase diagram approaches were used to determine the P-T conditions experienced by sample VJ-03-01-20-2. For the conventional approach, we applied garnet-biotite (GB) thermometry (Ferry & Spear, 1978; Berman, 1990) and garnet-plagioclase-biotite-muscovite (GPBM) barometry (Hoisch, 1990). We used the lowest Mn and lowest Fe/(Fe+Mg) garnet paired with matrix minerals (biotite, plagioclase, and muscovite) for these conventional rim P-T conditions. To determine the garnet core conditions, we used the program Theriak-Domino for the isochemical phase diagrams (de Capitani & Brown, 1987; de Capitani & Petrakakis, 2010) and the Holland and Powell (1998) thermodynamic dataset with updates to solution models through 2010. Relevant mixing models in the system MnO-Na2O-CaO-K2O-FeO-MgO-Al2O3-SiO2-TiO2-H2O were used. The solid-solution models pertinent in this study are biotite (Powell & Holland, 1999; White et al., 2000), chlorite (Holland et al., 1998), chloritoid (Mahar et al., 1997; White et al., 2000), feldspar (Baldwin et al., 2005; Holland & Powell, 2003), garnet (Mahar et al., 1997; Zeh & Holness, 2003), ilmenite (Ideal Mn-Mg-Fe solution), staurolite (Holland & Powell, 1998; Mahar et al., 1997), and white mica (Coggon & Holland, 2002). The system was considered to form in the presence of water (activity of H2O = 1.0), and the iron oxidation state was 2+. We assume H2O saturation (i.e., H2O (100) in Theriak-Domino). Whole-

rock molar wt% data was used as direct input for developing the isochemical phase diagrams. Primary garnet compositions are modified due to diffusion, as shown by the flat Mn zoning, but the grossular and pyrope appeared to follow trends across the garnet that may indicate some degree of primary preservation (Figure 2.10b). As Ca diffuses more slowly in garnet compared to Fe, Mn, and Mg (Spear, 1993), isopleths of grossular and pyrope (± 0.2-mole fraction) were overlain on the P-T diagrams to evaluate potential conditions of the garnet core.

Samples with monazite inclusions in garnets (VJ-03-01-20-2 and VJ-03-01-20-1A) were cut and mounted with a monazite Th-Pb age standard (554) in a 1-inch epoxy ring for secondary ion mass spectrometry (SIMS) U/Th-Pb analysis at the Institute of Earth Sciences at Heidelberg University. Monazite ages were obtained using the CAMECA ims1280-HR ion microprobe at Heidelberg University (Table 2.3). The reference used was monazite 554 (45.3 ± 1.4 Ma, ±2σ; Harrison et al., 1995). A common 204Pb correction after stripping the contribution of 144Nd232Th16O2++ estimated from 143Nd232Th16O2++ and the isotopic ratio of 144Nd/143Nd = 1.95 was applied for all grains. To test for potential matrix effects that are known for monazite with different Th abundances (Stern & Berman, 2001; Fletcher et al., 2010), a series of eight reference monazites was cross-calibrated using 44069 monazite as the primary reference. An analytical procedure using high-energy ions (−40 eV relative to the nominal accelerating voltage of +10 kV) minimized monazite matrix effects to within ±2% (relative) of reported Th-Pb ages for most reference monazites, except for very high-Th monazite. The approximately 10× lower abundance of high-energy secondary ions, however, precluded taking this approach for the comparatively young monazite samples. Instead, a conventional (Harrison et al., 1995) setup was used, for which an additional age uncertainty of ∼5% (relative) is estimated because of the slightly higher Th abundances indicated by primary-beam normalized ThO2+ count rates for the unknowns relative

to the reference monazites. This bias is typically within the stated uncertainties based on propagating counting and calibration curve uncertainties for the young monazites studied here.

2.5 Results

2.5.1 Lithologic and Structure Data

The eastern limb of the shear zone exposes banded, quartzofeldspathic gneisses locally interlayered with boudinaged amphibolite (Figure 2.7b). The shear zone also exposes garnet-bearing schist (Figure 2.7c,d) and meter-scale boudinaged gabbro blocks (Figure 2.7e). At deeper structural levels away from the overlying Whipple detachment fault, both amphiboles and feldspars are aligned in the NE-SW direction, parallel to the regional mylonitic lineation in the Whipple shear zone. In contrast, feldspars at the highest structural level directly below the Whipple detachment fault are cataclastically fractured in crystal-plastically deformed quartz-mica matrixes (Figure 2.7g).

The western limb of the Whipple shear zone exposes mylonitic, leucocratic, sheet-like granitic intrusions (feature 1 marked by white arrows in Figure 2.8a), which either truncate an older set of mylonitic foliation (feature 2 marked by yellow arrows in Figure 2.8a) or are concordant with the hosting foliation (see features 1 for the sill and 2 for the mylonitic foliation in Figure 2.8b). Leucocratic sills are isoclinally folded into parallelism to the mylonitic foliation (feature 3 in Figure 2.7b). Leucocratic intrusions that crosscut the mylonitic foliation may also be mylonitically foliated (e.g., feature 4 in Figure 2.8b). Garnet-bearing leucogranite bodies are folded and foliated in the shear zone (Figure 2.8c). Curviplanar and shear-offset leucocratic veins are present in some boudinaged but internally undeformed amphibolite bodies characterized by a salt-pepper texture (Figure 2.8d). The nonfoliated amphibolite bodies also contain pockets of coarse-grained, undeformed mafic materials (Figure 2.8d).

The rock units in this study area within the Whipple mylonitic shear zone (Figure 2.7a) include a two-mica garnet-bearing metapelite (Figure 2.7c), garnet schist (Figure 2.7d), quartzofeldspathic gneiss (Figure 2.7g), amphibolite with interlayered quartz veins (Figure 2.7f), and gabbro blocks/boudins (Figure 2.7b,e). Key mineral assemblages for some garnet-bearing metapelites include sillimanite and/or kyanite. Garnets found in metapelites throughout the Whipple mylonitic shear zone may be as large as ~1 cm across 2.7c,d); however, a leucogranite vein was found with abundant garnets >1 cm (Figure 2.8c). Feldspar crystals in the mylonitic gneiss fabric record top-to-the-northeast sense of shear, as is shown in Figure 2.8e.

Generally, the foliation along transect A-A′ (Figure 2.3) follow a continuous dome-shaped trend in dip direction. Foliation dips ~25° north-east in the northeastern section of the map, foliation flattens toward the center of the mountain range and dips radially, and foliation dips south-west in the southwestern section of the map. Stretching lineation parallel to foliation is consistent with the dip direction of the foliation. Boudinaged gabbro blocks display stretching in an east-west direction (Figure 2.7b). Figure 2.8a,b highlights mylonitic, sheet-like, granitic intrusions found throughout the entire shear zone, some of which are several meters thick; others are folded with the fold axial planes parallel to the mylonitic foliation.

Sample VJ-03-01-20-1A (Figure 2.9a) was collected from a two-mica garnet metapelite that contains garnet + biotite + muscovite + chlorite + quartz and accessory minerals xenotime + monazite + allanite + zircon + ilmenite + rutile. Petrographic images highlight zones of banded mica-rich versus quartz-rich layers (Figure 2.9c). Porphyroblastic garnets are broken and altered, have reaction rims, and appear surrounded mainly by mica layers (Figure 2.9d). Monazite inclusions in a garnet range from ~15 to 50 mm in size but appear fully inside the garnet grains with no visible traces of fluid interaction along cracks. Sample VJ-03-01-20-2 (Figure 2.9d) was

collected from a garnet schist that contains garnet + biotite + muscovite + chlorite + plagioclase + quartz and accessory minerals monazite + ilmenite + zircon. Most porphyroblastic garnet grains are surrounded by a mica matrix, and a smaller subset of garnet grains are surrounded by quartz. The garnet porphyroblasts are aligned parallel to the foliation, providing useful kinematic indicators of delta and sigma clasts (Figure 2.9a,d). Monazite inclusions in garnet are ~10–20 μm, but some were also found in the matrix within banded mica veins. Petrographic images in all samples highlighted the fine- to medium-grained lepidoblastic mica layers and banded to slightly crenulated mylonitic fabric.

2.5.2 P-T-t Data

Figure 2.7c shows sample VJ-03-01-20-1A collected from the Whipple Mountains. Garnet in the sample trapped an allanite-monazite reaction texture during crystallization (Figure 2.10a). The texture is similar to observations elsewhere that document monazite appeared after allanite decomposition (Broska et al., 2000; Catlos et al., 2002). SIMS dates from monazite grains within the center of the texture are Paleocene–Early Eocene (62 ± 9 Ma, 67 ± 7 Ma, and 80 ± 6 Ma (Th-Pb dates, ±1σ)) (Table 2.3). Th-Pb dates from another monazite inclusion in garnet from the same rock are older (1.01 ± 0.08 Ga; ±1σ).

Compositional transects across a garnet collected nearby (VJ-03-01-20-2) yield flat zoning in almandine and spessartine but high pyrope and lower grossular contents in the core than the rim (Figure 2.10b). Conventional P-T estimates (Ferry and Spear, 1978; Hoisch, 1989; Berman, 1990) using the garnet rim and matrix minerals from VJ-03-01-20-2 are rim, 680–750 °C and 7–9.4 kbar; and core, 750–800 °C and 6.2–7.8 kbar (Figure 2.10c). We overlie these conditions on the sample's isochemical phase diagram, and the predicted mineral assemblage overlaps the rock's observed major mineral assemblage (garnet + feldspar (plagioclase) + biotite + muscovite + ilmenite +

quartz + H2O) (Figure 2.10c). We also overlie the grossular and pyrope compositions from the garnet core onto the isochemical phase diagram because they may have preserved their prograde conditions best. In this case, the garnet core yields conditions of 750–800 °C and 6–7.5 kbar, consistent with the garnet crystallizing at higher-grade conditions. These conditions lack muscovite with the assemblage of garnet + feldspar (plagioclase) + biotite + ilmenite + quartz + H2O (Figure 2.10c).

2.6 Discussion

2.6.1 Magmatism and Exhumation

Each core-complex system along a narrow zone of Laramide-thickened orogenic axial zone from southern Canada to northern Mexico provides insight into the development of low-angle detachment faults (Coney & Harms, 1984). At a regional scale, there is evidence that crustal melting during the Late Cretaceous to Eocene time, extension, and core-complex formation may be linked (Chapman et al., 2021). In some cases, magmatism in the Cordilleran Anatectic Belt may be directly related to the timing of core-complex extension. For example, in the Valhalla complex (Figure 2.1), the duration of magmatism at 60–50 Ma directly overlaps with the onset of extension at 60 Ma and rapid extension at 50 ± 2 Ma, and the peak timing of metamorphism also spans that duration of time (60–57 Ma, Spear & Parrish, 1996; Holk & Taylor Jr, 2000; Spear, 2004; Gordon et al., 2008; Chapman et al., 2021; Table 2.1).

In contrast, the Cordilleran Anatectic Belt Late Cretaceous-age magmatism at 86–70 Ma recorded in plutons from the Snake Range core complex in Nevada is consistent with the timing of peak metamorphism at 90–70 Ma, different from estimates of Tertiary extension with an onset at 45 ± 3 Ma and rapid extension at 20±2 Ma (Table 2.1; Lee & Christiansen, 1983; King et al., 2004; Henry et al., 2011; Hallett & Spear, 2014, 2015; Evans et al., 2015; Gottlieb, 2017; Lee et al.,

2017; Chapman et al., 2021). Similarly, in the Whipple Mountains, the Whipple Wash granite pluton emplacement occurred at 89 ± 3 Ma and mylonitization due to extension between 26.6 ± 1.1 Ma and 13.7 ± 0.4 Ma (Anderson et al., 1988; Stockli et al., 2006). These previous estimates for the latest Tertiary mylonitization were the expected monazite-in-garnet ages that would have represented a single-phase of extension during middle to late Cenozoic time (Wong et al., 2023). However, the monazite dates from the metapelite rock yielded much older ages, which suggests a larger time span over which the deformation occurred. Thus, the monazite ages from this study suggest a Late Cretaceous to Paleogene metamorphic event that has not been accounted for in past studies. Recent studies propose a multiphase deformation history for the Whipple Mountains shear zone (Seymour et al., 2016; Flansburg & Stockli, 2023; Kapp et al., 2023; Wong et al., 2023). Thus, we tentatively interpret the younger monazite ages of 80–62 Ma to date peak metamorphism of the garnet schist in the Whipple ductile shear zone. Garnet often appears during the allanite → monazite reaction (Figure 2.10a) during the metamorphism of pelitic bulk rock compositions (e.g., Smith and Barreiro, 1990; Catlos et al., 2002). Within error, pluton emplacement in the Whipple Mountains overlaps with the monazite dates (Table 2.3) and suggests a possible relationship between crustal melting and metamorphism at depths >25 km (Anderson et al., 1988). We note that when correlating whole-rock geochemistry to crustal thickness, crustal contamination of magma bodies and their influence on quantitative outputs should be considered (Chapman et al., 2015, 2020).

2.6.2 Past Models

Models describing how low-angle detachments operate in the middle crust suggest that mylonitic zones within the detachments accommodate strain and, thus, areas of extreme extension (Singleton et al., 2022). Most of the metamorphic core complexes record NE-directed hanging-wall extension

in the southern segment of the North American Cordillera. In the northern segment, east-west extension is more prominent and is perpendicular to the N-S-trending margin of the Sevier Thrust Belt front (Figure 2.1) but parallel to shear strain and flattening direction (e.g., Frenchmans Cap) (Gervais et al., 2010). Reconstructions of detachment faulting in the North American Cordillera core complexes have been possible by examining dike swarms (Richard et al., 1990; Foster et al., 1993; Gans & Gentry, 2016). Strain alone may help determine the deformation mechanism in an area, especially if the area has undergone multiple deformation events, thus differentiating competing kinematic models have yielded ambiguous results.

Behr and Platt (2011) combined structural, thermobarometric, and geochronological data to infer differential stress versus T and differential stress versus depth profiles for samples from the Whipple detachment to constrain their profiles consistent with previously suggested P-T conditions. The thermal model assumptions include an initial geothermal gradient of 25 °C/km (Foster & John, 1999), density of upper crust of 2,700 kg/m3, density of lower crust of 2,800 kg/m3, conductivity of 2.5 W/mK, heat capacity of 1,000 J kg K−1, and heat production of 2.3e-6 W/m3. The slip rate of 5.9 mm/yr used for the Whipple fault is from average estimates reported by Foster and John (1999) and Stockli et al. (2006). The dip angle of the Whipple fault was estimated at 25° based on data from Davis (1988). Anderson et al. (1988) provided an estimate of peak metamorphism of 4.6 ± 0.9 kbar, which Behr and Platt (2011) used to constrain a stress profile through the middle crust. Their studies showed that the peak strength at the brittle-ductile transition zone in the Whipple Mountains reached stresses ranging from 1.04 to 1.36 kbar at a depth of 9 km (Anderson et al., 1988; Behr & Platt, 2011). The Behr and Platt (2011) model for determining a stress profile follows normal continental-strength profile conditions. However, a stress magnitude at its current location cannot be used as the stress value at its initial deformation location when the

P-T-time paths are unknown because maximum shear stress varies in magnitude with time and space (Behr & Platt, 2011).

2.6.3 P-T Constraints and Future Work

Our garnet rim P-T estimate from sample VJ-03-01-20-2 of 7–9.4 kbar and 680–750 °C and core condition of 6.2–7.8 kbar and 750–800 °C (Figure 2.10c) suggests that rocks now exposed at the surface were deformed at conditions close to those in the middle crust. Divalent-cation compositional zoning in garnet grains <100 μm has long been known to alter prograde compositions at T>600 °C (e.g., Tracy et al., 1976; Florence and Spear, 1991; Ganguly, 2010), which is consistent with the observation of flat garnet zoning in Mn and Fe in sample VJ-03-01-20-2 (Figure 2.10b). Conventional thermobarometry, isochemical phase diagrams, and isopleth thermobarometry approaches that are used to determine P-T conditions prescribe that the samples experienced closed system behavior and no modification of garnet chemistry after growth (e.g., Lanari & Engi, 2017). An additional assumption is that the sample experienced equilibrium, which can never be proven for any rock (Spear & Peacock, 1989; Lanari & Duesterhoeft, 2019). Sources of uncertainty for the thermobarometric approach applied here include the accuracy of electron microprobe analyses, calibration errors, variations in activity models, compositional heterogeneity, and uncertainty associated with the thermodynamic properties inherent in the choice of an internally consistent database (Kohn & Spear, 1991; White et al., 2014; Lanari & Duesterhoeft, 2019). Because the error suggested by the grid created due to overlapping mineral compositional isopleths likely underestimates the actual uncertainty, we suggest applying uncertainty values (±25 °C and ±1 kbar) to the overlapping isopleth conditions as is commonly reported for conventional thermobarometry (e.g., Spear & Peacock, 1989; Kohn, 1993; Kohn et al., 2001). The approach to generating P-T conditions discussed here transforms the sample into a

model representing the true rock and mineral assemblage. It also restricts its behavior as if it was in a closed system. Confidence in conventional P-T conditions increases when conditions agree with mineral assemblages and are consistent with garnet zoning. A value of the isopleth approach is that a user can detect when systems stray from the equilibrium and closed system assumptions (Catlos et al., 2020, 2022). The conditions obtained here are consistent with the rock's mineral assemblage and garnet zoning. If these conditions record garnet growth during metamorphism and not a previous metamorphic cycle, the results suggest that the rolling-hinge (Figure 2.1b) and simple-shear (Figure 2.1c) models are more applicable to the Whipple Mountains (Wernicke, 1985; Wernicke and Axen, 1988).

Overall, the P-T data suggests that a detachment along the base of the upper crust is too shallow. Models that place the shear zone at a depth of ~15 km, 5 kbar, and 350–400 °C, barely in the ductile deformation regime of the crust, appear inapplicable to the Whipple Mountains (Figure 2.4). The results permit the detachment fault to have extended at least into the middle crust. The data cannot address whether the fault could have extended farther into the lower crust and even the mantle lithosphere. The most important insight is that (a) the maximum shear stress varies in magnitude with time and space, and (b) a measured stress magnitude at its current location cannot be used as the stress value at its initial launching point when the P-T-t path of the hosting rock mass is unknown (cf., Behr & Platt, 2011, 2014). With this new information, a new P-T-t path may be established for the rocks in the Whipple detachment and may suggest a deeper initiation or multiple metamorphic events not previously analyzed.

It is important to note that the P-T estimates were determined by analyzing sample VJ-03-01-20-2. Meanwhile, the monazite inclusion ages were determined by analyzing sample VJ-03-01-20-1A. Both samples are collected near each other (Table 2.2), although one is structurally higher

than the other by a couple hundred meters. Abundant garnets found throughout the study area provide a starting point for determining the tectonometamorphic evolution of the Whipple ductile-shear zone. Locally, systematic sampling across the Whipple detachment shear zone has not been conducted. However, the P-T-t data from a single garnet suggests that the approach has the potential to tremendously improve existing ideas regarding the conditions experienced. New thermobarometric approaches to determine P-T estimates for the Whipple detachment shear zone garnets must be carried out. Further studies may be able to differentiate between existing models that have attempted to explain how the rocks reached said conditions (Strickland et al., 2018; Chapman et al., 2020; Chapman et al., 2021).

2.7 Conclusions

Extensive studies have been conducted on metamorphic core complexes of the northern and central segments of the North American Cordilleran metamorphic core-complex belt. However, much more work is needed in the southern segment of the belt to better constrain the mechanisms of core-complex development in this region. We present an approach to constrain the deformation history along the Whipple detachment shear zone. P-T data obtained from the Whipple detachment shear zone indicate that the mylonitic shear-zone deformation occurred under higher-grade conditions than previously thought. These P-T conditions indicate deformation at midcrustal levels, which may eliminate kinematic models that suggest deformation occurred solely in the upper crust. The monazite-in-garnet inclusion ages at 62 ± 9 Ma, 67 ± 7 Ma, and 80 ± 6 Ma (Th-Pb dates, ±1σ) do not represent Oligocene shear zone development; instead, they highlight a possible metamorphic event during Paleogene time that has not been accounted for in the models until recently. Therefore, the suggested systematic and detailed approach with these new P-T-t conditions may be used to refine previous models and continue to constrain the spatiotemporal

evolution of the Whipple mylonitic shear zone. Future work and coupled studies between P-T estimates and the age determination of the P-T history may further highlight how continental extension plays a role in low-angle detachment faulting. This approach would determine whether there have been multiple deformation events in the Whipple ductile-shear zone, plus it would apply to other shear zones across the North American Cordilleran metamorphic core complexes.

2.8 Figures

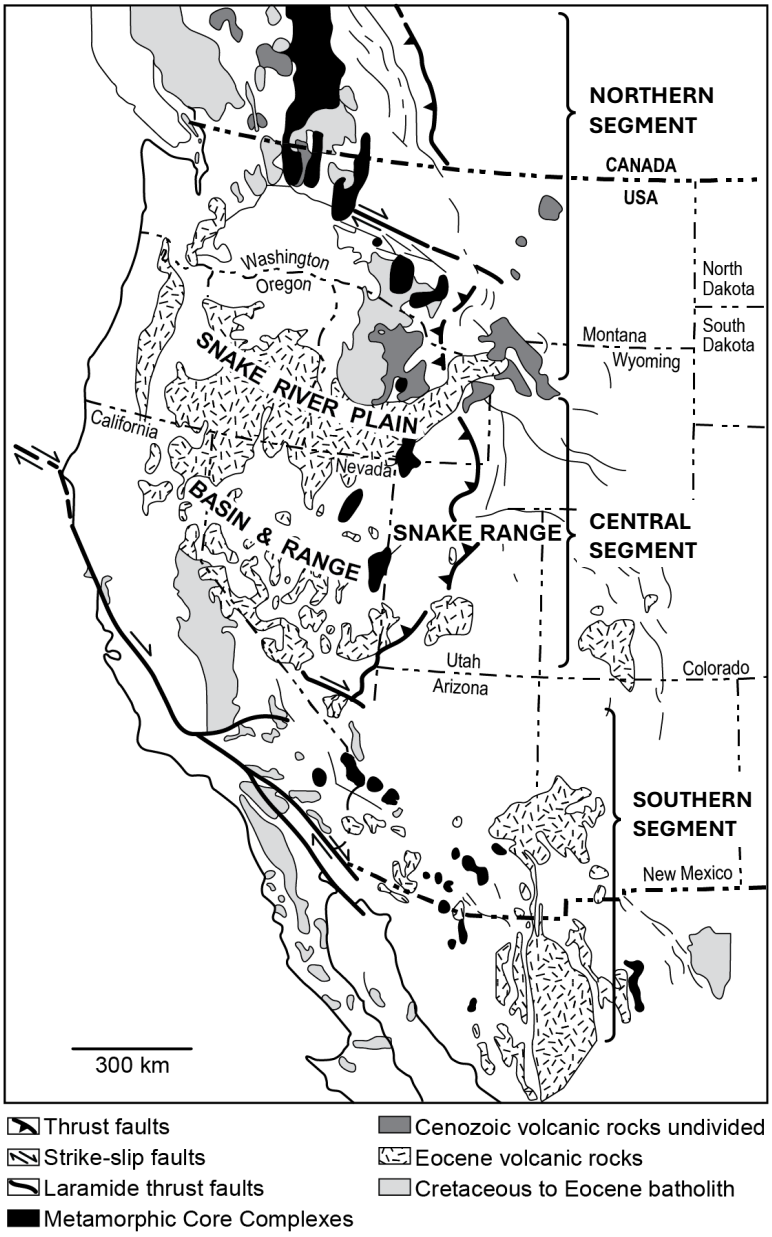

Figure 2.1. Map of the North American Cordilleran Anatectic Belt and metamorphic core complex locations, Sevier thrust belt front, and Laramide deformation front. Map projection: UTM, NAD 83 Zone 12N. From Gébelin et al., (2011).

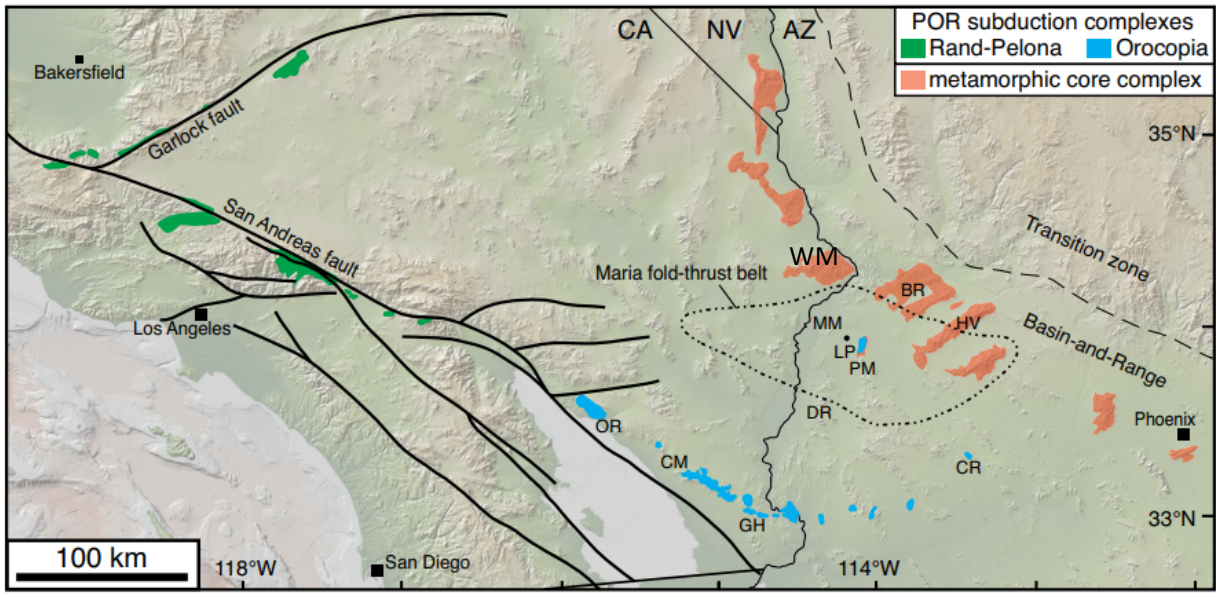

Figure 2.2. Map illustrating the distribution of Pelona-Orocopia-Rand Schists (PORS) subduction complexes in southern California and southwestern Arizona (USA), and locations of the Whipple Mountains (WM) and other ranges mentioned in the text (modified from Haxel et al., 2014). Base map is colored by elevation and derived from GeoMapApp (http://www.geomapapp.org). Maria fold-and-thrust belt dotted outline is modified from Spencer and Reynolds (1990). Orange polygons indicate Miocene metamorphic core complexes. Bold black lines are major Quaternary strike-slip faults. BR—Buckskin-Rawhide Mountains; CM—Chocolate Mountains; CR—Cemetery Ridge; DR—Dome Rock Mountains; GH—Gavilan Hills; HV—Harcuvar Mountains; MM—Mesquite Mountains; OR—Orocopia Mountains; PM—Plomosa Mountains. Modified from Strickland et al. (2018).

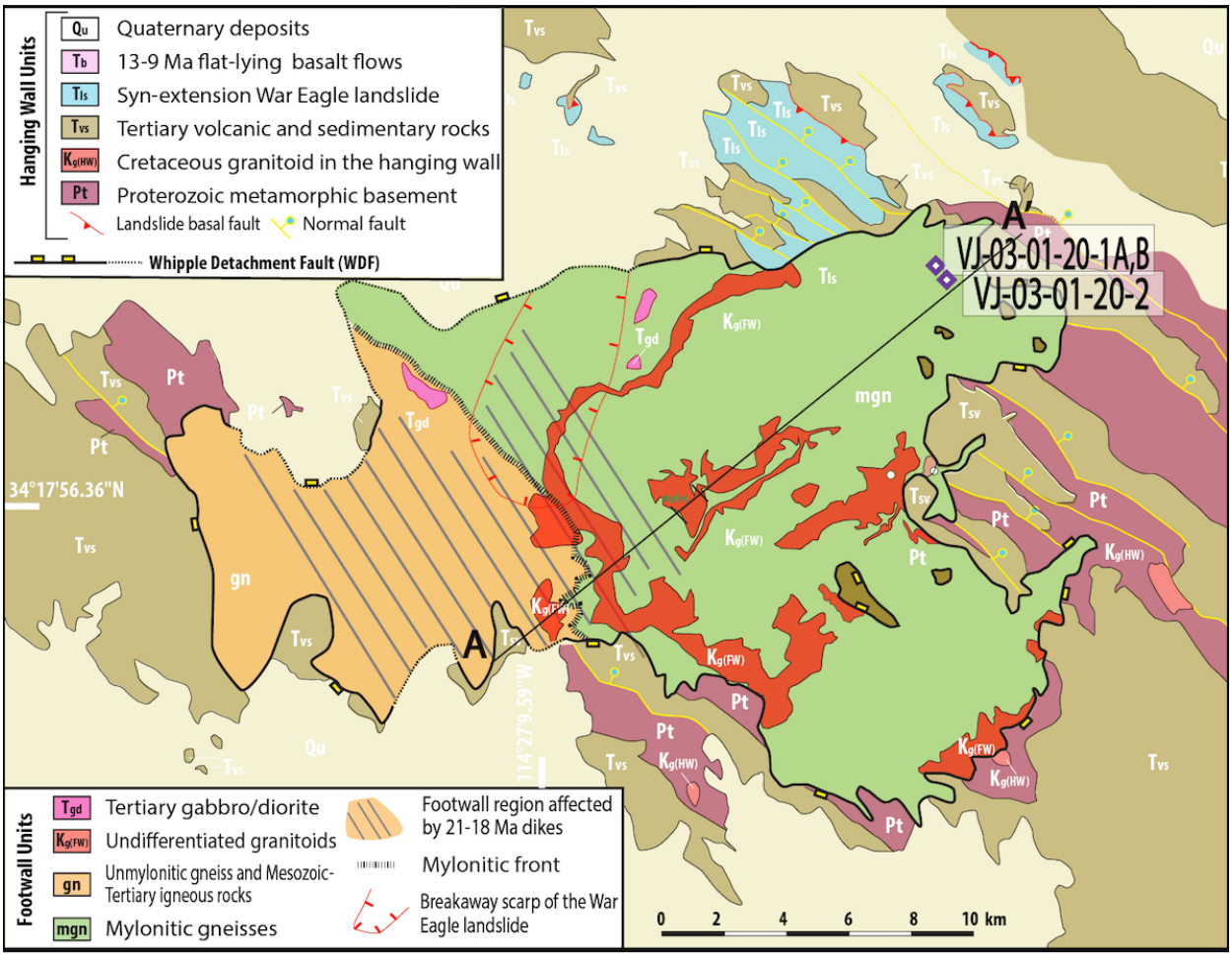

Figure 2.3. Simplified geologic map of the Whipple Mountains based on a compilation of Davis (1998), Yin & Dunn (1992), Forshee &Yin (1995), Behr &Platt (2011), and Gans & Gentry (2016). The diamond corresponds to the monazite sample location VJ-03-01-20-1A and VJ-03-01-20-2.

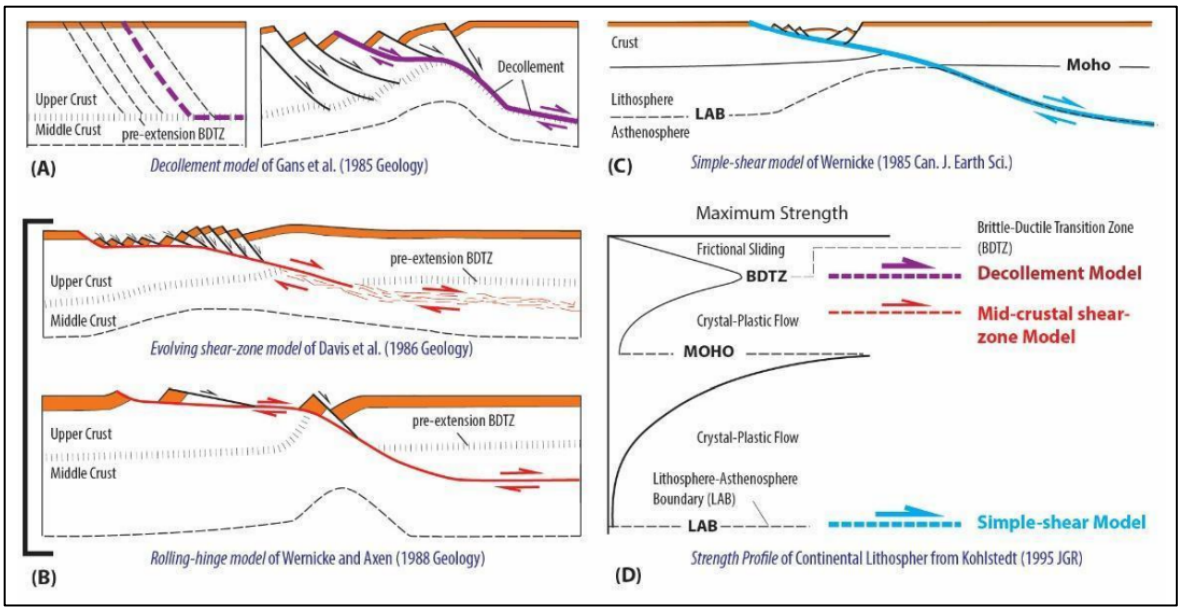

Figure 2.4. (A)-(C) Models of detachment-fault-system evolution. (D) Inferred strength profile of the continental lithosphere.

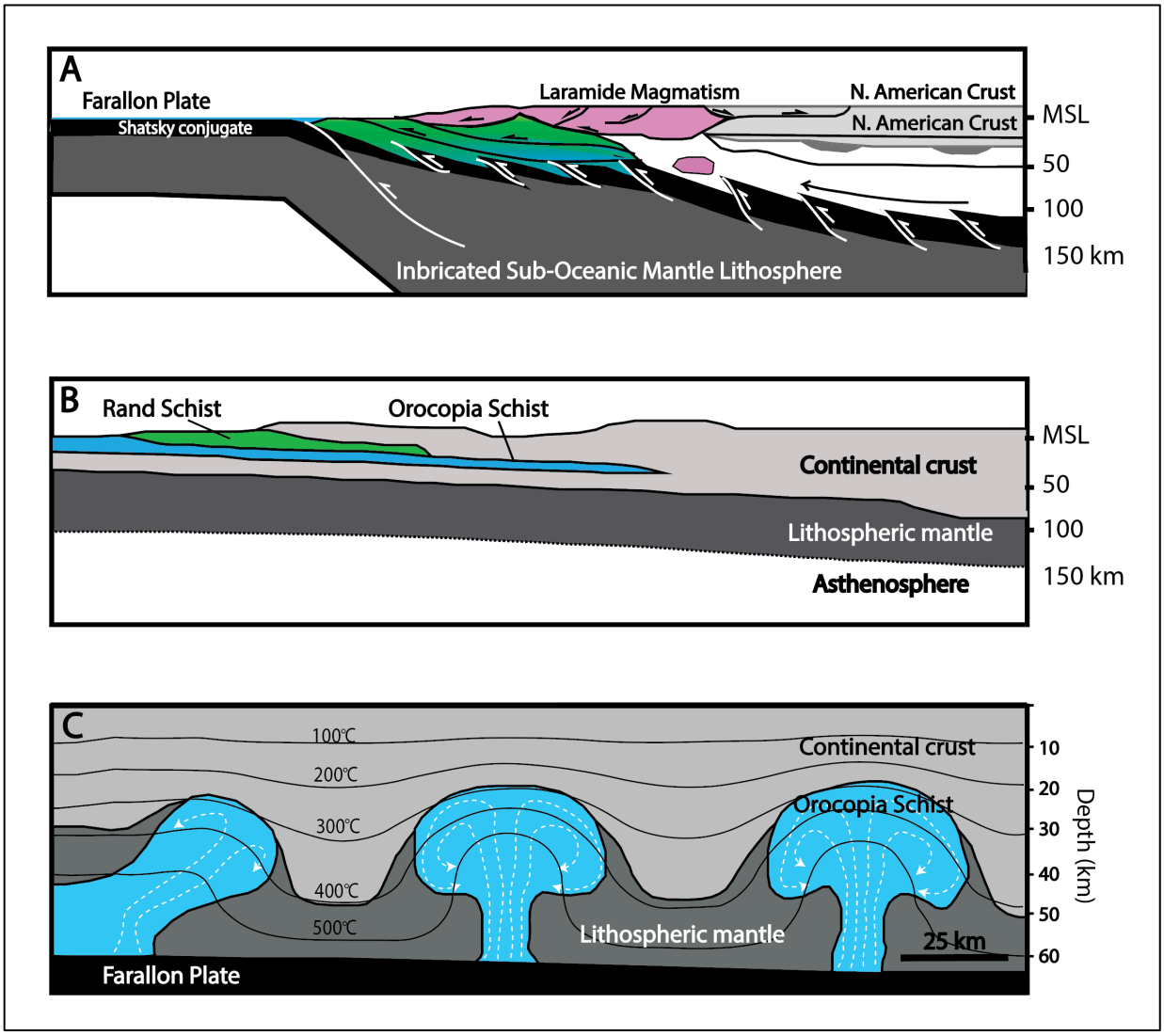

Figure 2.5. Three end-member models for the emplacement of the Orocopia schist below Mojave Desert. (A) Shallow-angle subduction and schist underplating (A.D. Chapman et al., 2020) (B) Proposed mechanism of underplating of the Orocopia Schist without subduction (S Strickland et al., 2018) **(C)** Diapiric-style emplacement of Orocopia Schist (J.B. Chapman, 2021).

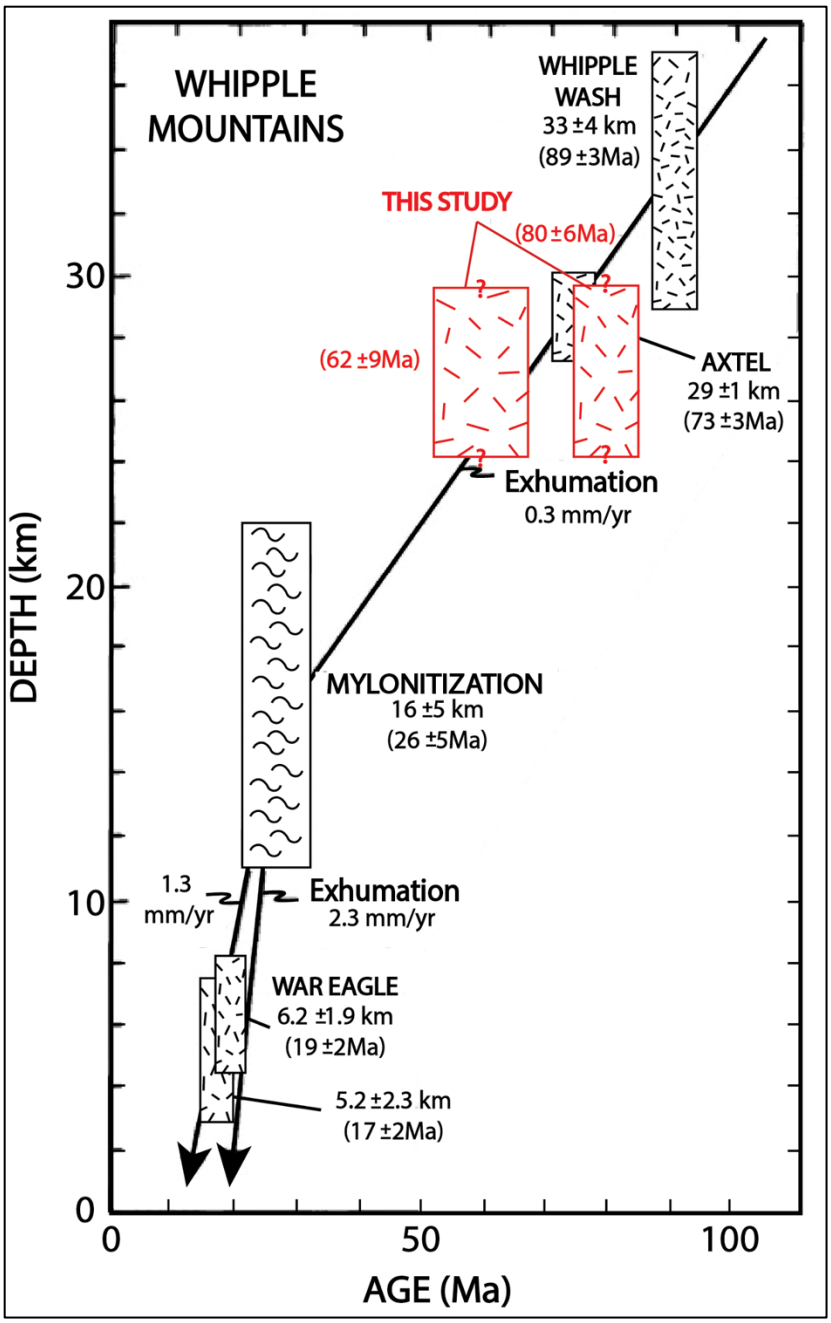

Figure 2.6. Transport of crustal sections in the Whipple Mountains as a function of age. The old 16 ± 5 Ma age is refined to 24.1 ± 0.5 Ma by Foster & John (1999). Red boxes illustrate the monazite ages and their approximate depth. Modified from Anderson et al. (1988).

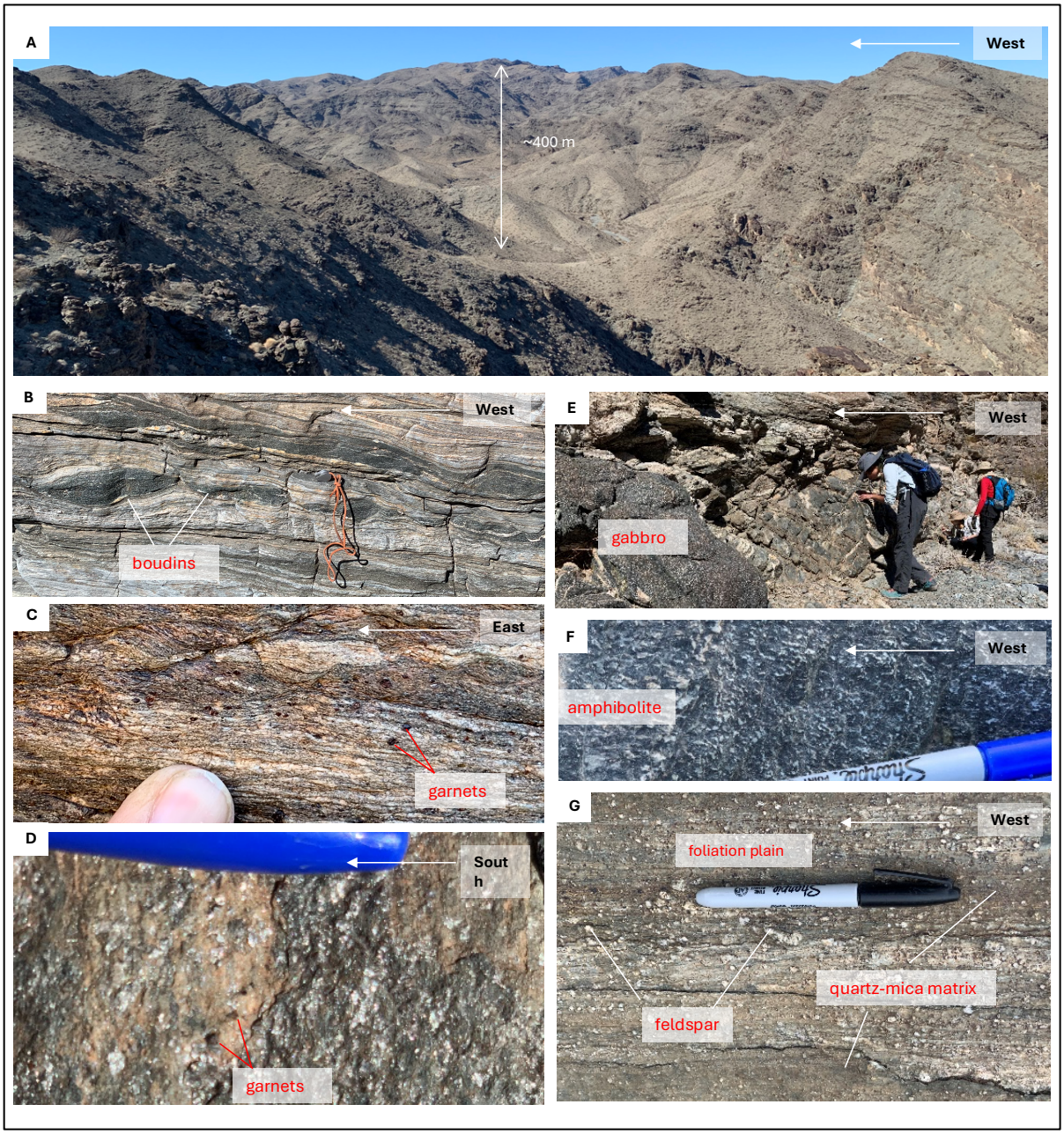

Figure 2.7. **(A)** Landscape photograph of the Whipple Mountains highlighting a 400-meter-thick section of exposed shear zone rocks. Outcrop photographs of **(B)** boudinage **(C)** garnets in foliated **(D)** garnets in a mica schist **(E)** gabbro blocks **(F)** amphibolite **(G)** mylonitic gneiss with blocky feldspar grains as kinematic indicators.

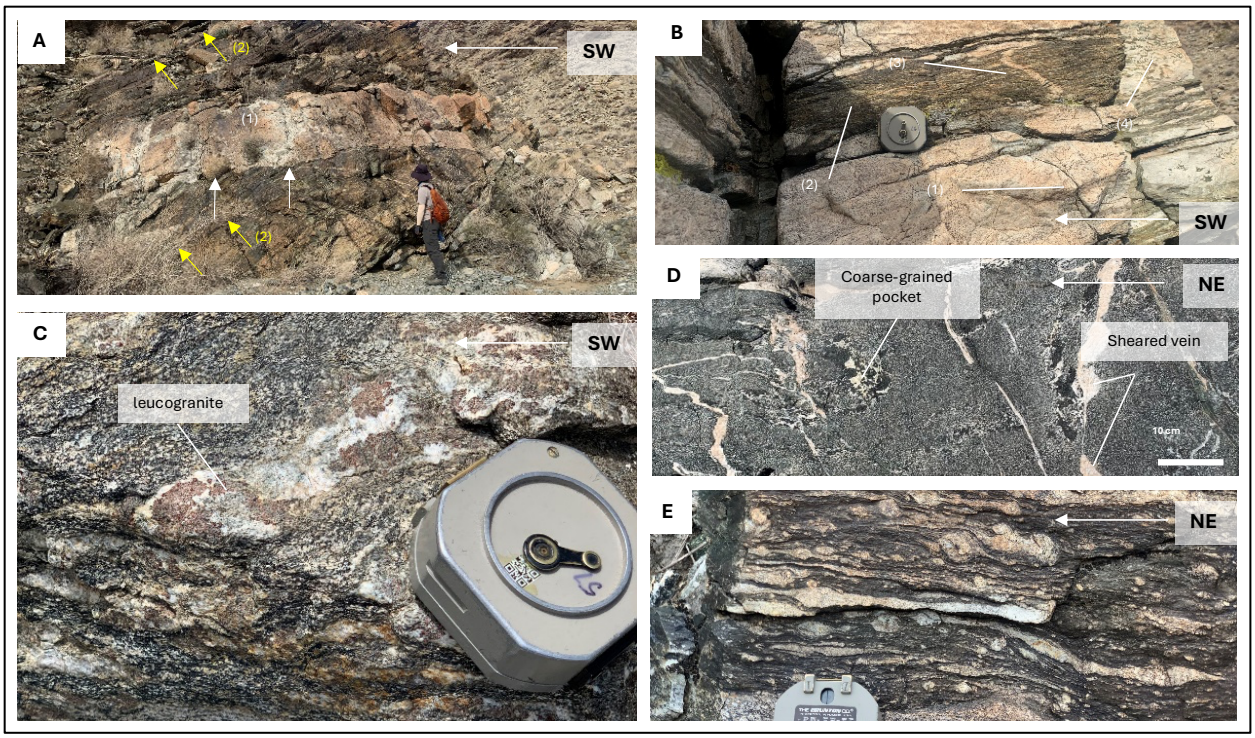

Figure 2.8. **(A)** Mylonitic, leucocratic, ~1.5-meter-thick, sheet-like granitic intrusion **(B)** Leucocratic sills are locally isoclinally folded into parallelism to the mylonitic foliation **(C)** Folded and foliated garnet-bearing leucogranite bodies **(D)** Curviplanar and shear-offset leucocratic veins are present in some boudinaged, but internally undeformed amphibolite bodies characterized by a salt-pepper texture **(E)** Unfoliated amphibolite bodies also contain pockets of coarse-grained, undeformed mafic materials.

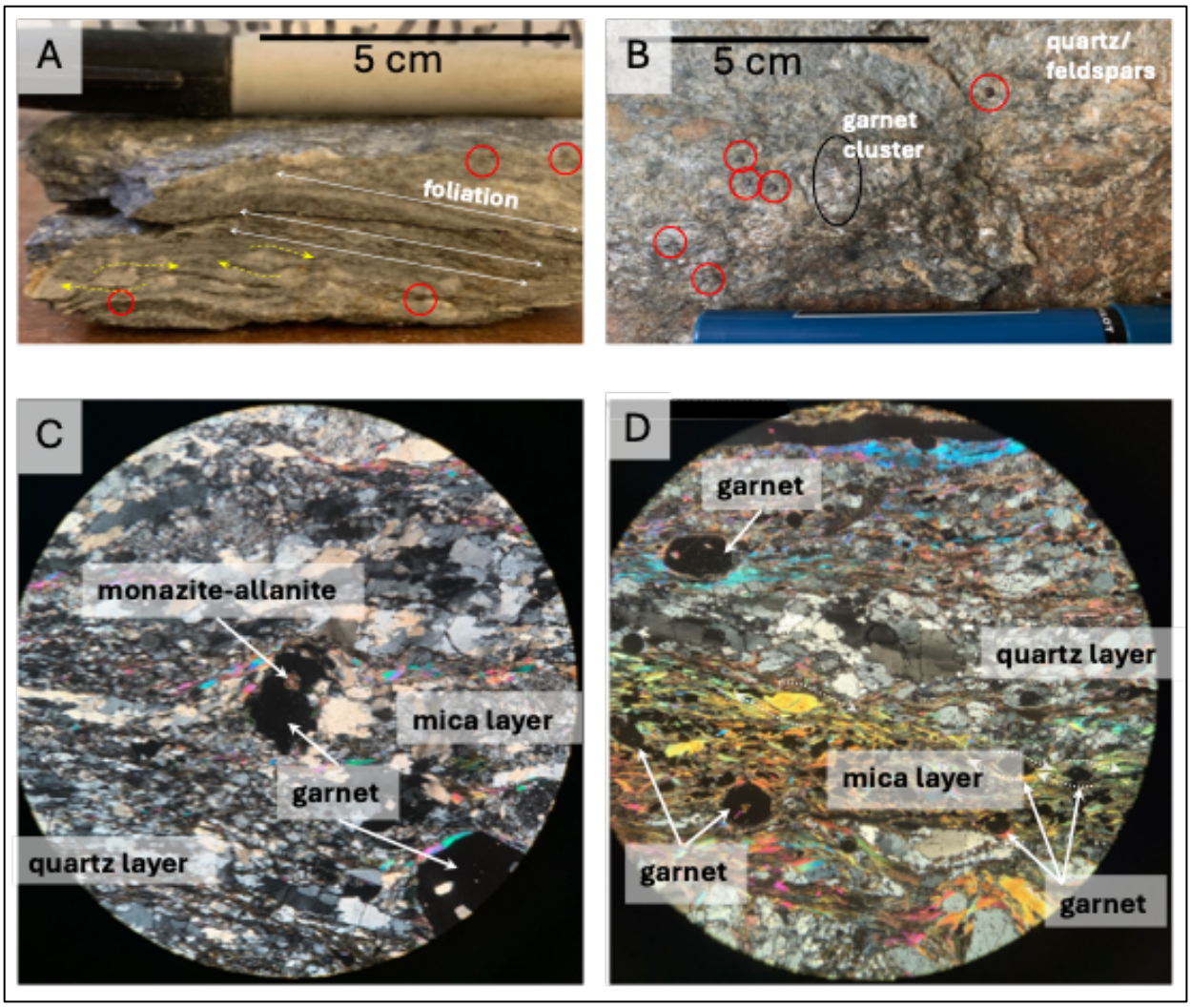

Figure 2.9. Garnet-bearing metapelite samples used to determine thermobarometric constraints. (A) Sample VJ-03-01-20-1A, a two-mica, garnet-bearing metapelite. The white lines with arrows on both ends illustrate the foliation direction in the sample, crenulated cleavage is visible in between the bottom two white lines. The dashed yellow lines highlight feldspar kinematic indicators with top-to-the-right sense of shear. Garnet grains are enclosed in the red circles. (B) Sample VJ-03-01-20-2, a garnet schist. Individual garnet grains are enclosed in red circles. A cluster of garnet grains is enclosed in the black oval. The matrix is composed of mica, quartz, and feldspar grains. (C) Petrographic image of sample VJ-03-01-20-1A. Monazite-allanite reaction texture enclosed in a garnet was used for Th-Pb age data. Bottom-right garnet grain highlights various inclusions. Oriented quartz grains are visible in the quartz layer and mica layer surrounding the top of the garnet grain. (D) Petrographic image of sample VJ-03-01-20-2. Garnet grain at the top-left contains various inclusion including a ~10-micron sized monazite grain used for Th-Pb age data. Mica (muscovite, biotite, chlorite) and quartz banding clearly visible. Garnet grains in the bottom-right are deformed and appear to have top-to-the-right sense of shear as highlighted by the dotted white arrows.

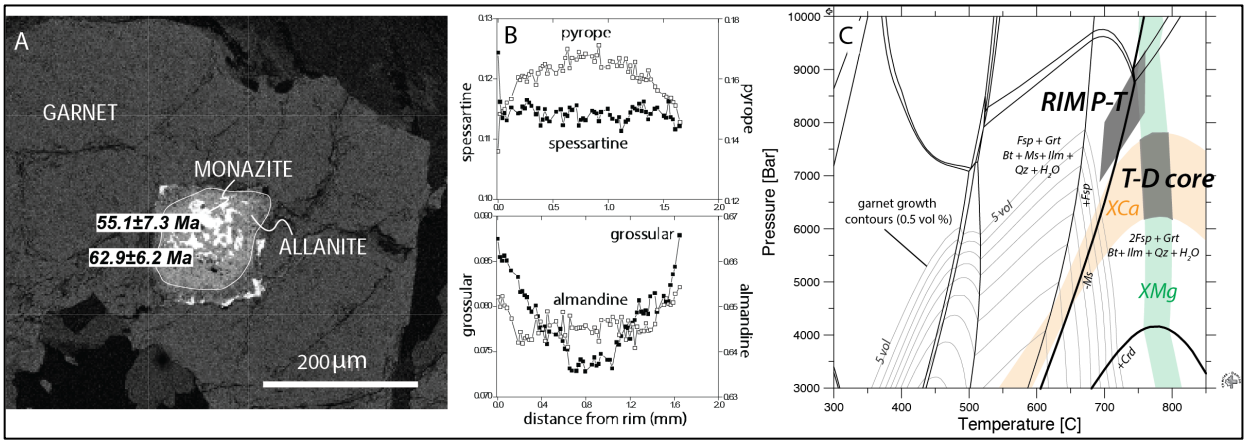

Figure 2.10. (A) Backscattered electron (BSE) image of a Whipple Mountains garnet with an allanite-monazite reaction texture occluded. Th-Pb SIMS ages are indicated (±1σ). (B) Compositional transects of Mn, Mg, Ca, and Fe from garnet in the same sample show trends from rim to rim. **(C)** The sample's isochemical phase diagram using the rock bulk composition and the program Theriak-Domino (see proposal text). Garnet growth contours (0.5 vol %) and the conventional rim P-T estimate are overlain on the diagram. Colored bars are the garnet mole fraction Mg (XMg) and Ca (XCa) from the garnet core (±0.2 mole fraction). These bars intersect at lower P but higher T than the garnet rim and yield our best estimate for the garnet core conditions, assuming equilibrium conditions and lack of retrogression since metamorphism and garnet growth.

2.9 Tables

Table 2.1. List of metamorphic core complexes associated with the southwestern portion of the North American Cordillera [a].

Core complex	Reference[b]	Core complex extension Timing		Metamorphism Timing and Peak Conditions		
Name		**Rapid Extension (Ma) (±1σ)**	**Extension onset (Ma)**	**Peak Timing (Ma)**	**Peak P (kbar)**	**Peak T (°C)**
		California				
Whipple	Anderson & Cullers, 1990; Gans & Gentry, 2016	19(1)	20	-	~ 4.5	~ 450
Sacramento	Carter et al., 2006; Pease et al., 1999; Foster et al., 1990; Campbell-Stone et al., 2000	18 (2)	23	-	-	500
Chemehuevi	John & Foster, 1993; Carter et al., 2006	18 (2)	23	-	3.5-4.5	450-500
Iron Mountain	Boettcher & Walker, 1993; Wells et al., 2002	24	21	-	4.8	< ~ 670
Old Woman-Piute	Miller et al., 1990; Miller & Wooden, 1994	-	-	-	4-5	~ 650
		Arizona				
Mesquite		-	-	-	-	-
Buckskin-Rawhide	Singleton et al., 2014	19(2)	21	-	-	450-500
Plomosa	Spencer et al., 2018; Singleton et al 2022	18(2)	19	-	4.6-6	459-590
Harcuvar	Bryant & Wooden, 2008; Wong et al., 2011; DeWitt & Reynolds, 1990	17 (3)	24	-	-	-
Harquahala	Isachsen et al., 1999; Prior et al., 2016; Richard et al., 1990	19(2)	21	-	-	> 300
White tank	Shafiqullah et al., 1980; Prior et al., 2016	20(5)	-	-	-	-
South Mountain	Fitzgerald et al., 1993	20(5)	22	-	-	-
Picacho	Gottardi et al., 2018; Spencer et al., 2003 Schaper, 2016 (thesis)	20(2)	-	-	-	-
Tortolita	Creasey et al., 1977	22(3)	-	-	1.4-2.2	~ 661-682

Gunnery Range	Arnold, 1986	-	-	-	-	> 225
Pinaleno	Long et al., 1995	25(5)	-	-	-	300 – 415; 673-802
Santa Catalina	Fornash et al., 2013; Fayon et al., 2000; Terrien, 2012; Peterman et al., 2014; Davis et al., 2019; Ducea et al., 2020	25(2)	-	-	1.4-2.2	~ 661-682
Rincon		-	-	-	-	-
Texas Canyon	Chapman et al., 2018; Shafiqullah et al., 1980					> 225
Coyote	Wright & Haxel, 1982; Gottardi et al., 2020	29(2)	30	-	< 5	~ 400-500
		Northern Mexico				
Pozo Verde	Goodwin & Haxel, 1990	-	25	-	UG – LA	UG – LA
Guacomea	Anderson et al., 1980; Nourse et al., 1994	-	-	-	LA	LA
Tubutama-Mezquital	Mallery et al., 2018; Nourse et al., 1994	-	-	-	A	A
Carnero	Hayama et al., 1984; Jacobson et al., 2019	17(1)	-	-	LA	350-400
Jarillas Portrero-Tortuga		-	-	-	UA	UA
Magdalena Madera	Salas, 1968	23.5(1.5)	25	-	LA	> 500
El Babizo	González-León et al., 2011	-	-	-	A	A
Aconchi	Wong et al., 2010; Roldán-Quintana, 1991; González-León et al., 2011	23(3)	26	-	-	250-400
Puerto del Sol	Gonzalez-Becuar et al., 2017; Wong et al., 2008	-	-	-	> 5	900
Sierra Mazatan	Wong and Gans, 2008; Anderson, 1980	18(2)	25	-	> 5	-

Table 2.2. Bulk rock compositions (molar wt %) from samples analyzed in this study.

Sample/analysis	**VJ-03-01-20-1A**	**VJ-03-01-20-1B**	**VJ-03-01-20-2**
Latitude	34°22’34.41’’N	34°22’34.41’’N	34°22’32.98’’N
Longitude	114°19’24.30’’W	114°19’24.30’’W	114°19’16.00’’W
SiO_2	48.127	78.333	46.559
Al_2O_3	22.788	7.463	28.608
Fe_2O_3	8.602	6.873	7.834
MnO	0.466	0.587	0.165
MgO	4.858	3.549	3.370
CaO	3.173	0.517	2.146
Na_2O	5.443	0.298	3.960
K_2O	5.764	2.199	6.438
TiO_2	0.755	0.154	0.887
P_2O_5	0.024	0.026	0.034
Total	100.0	100.0	100.0

Table 2.3. Results of Th-Pb monazite ages for samples analyzed in this study.

Sample	Age (Ma)	Age (Ma)	% Radiogenic	Age (Ma)	Age (Ma)
	$^{208}Pb/^{232}Th$	$^{208}Pb/^{232}Th$	^{208}Pb	$^{207}Pb/^{206}Pb$	$^{207}Pb/^{206}Pb$
		1 s.e.			1 s.e.
VJ-03-01-20-2_VJ1_2.ais	79.8	6.0	81.5	-	-
VJ-03-01-20-1A_ VJ2_1a_1.ais	1011.0	82.3	99.1	1684	57
VJ-03-01-20-1A_ VJ2_1a_2.ais	62.1	9.1	81.2	-	-
VJ-03-01-20-1A_ VJ2_1a_2b.ais	66.5	6.8	86.4	-	-

2.10 References

Anderson, T. H., Sílver, L. T., Salas, G. A., Crittenden, J. M., Coney, P. J., & Davis, G. H. (1980). Cordilleran metamorphic core complexes. Geological Society of America Memoir, (153), 269-283.

Anderson, J. L., Barth, A. P., & Young, E. D. (1988). Mid-crustal Cretaceous roots of Cordilleran metamorphic core complexes. Geology, 16(4), 366-369.

Anderson, J. L. (1988). Core complexes of the Mojave-Sonoran Desert: Conditions of plutonism, mylonitization, and decompression. Metamorphism and Crustal Evolution of the Western United States, Rubey, 7, 503-525.

Anderson, J. L., & Cullers, R. L. (1990). Middle to upper crustal plutonic construction of a magmatic arc; An example from the Whipple Mountains metamorphic core complex. The Nature and Origin of Cordilleran Magmatism: Geological Society of America Memoir, 174 (1990), pp. 47-69

Anderson, J. L., & Rowley, M. C. (1981). Synkinematic intrusion of peraluminous and associated metaluminous granitic magmas, Whipple Mountains, California. The Canadian Mineralogist, 19(1), 83-101.

Armstrong, R. L. (1982). Cordilleran metamorphic core complexes-from Arizona to southern Canada. Annual Review of Earth and Planetary Sciences, 10, 129.

Armstrong, R.L., & Ward, P. (1991). Evolving geographic patterns of Cenozoic magmatism in the North American Cordillera: The temporal and spatial association of magmatism and metamorphic core complexes. Journal of Geophysical Research: Solid Earth, 96(B8), 13201-13224.

Atwater, T., & Stock, J. (1998). Pacific-North America plate tectonics of the Neogene

southwestern United States: an update. International Geology Review, 40(5), 375-402.

Axen, G. J. (1992). Pore pressure, stress increase, and fault weakening in low-angle normal faulting. Journal of Geophysical Research: Solid Earth, 97(B6), 8979-8991.

Axen, G. J. (2004). 3. Mechanics of low-angle normal faults. In G. D. Karner et al. (Eds.), Rheology and deformation of the lithosphere at continental margins (pp. 46-91). Columbia University Press.

Axen, G. J. (2007). Research focus: Significance of large-displacement, low-angle normal faults. Geology, 35(3), 287-288.

Axen, G. J. (2020). How a strong low-angle normal fault formed: The Whipple detachment, southeastern California. GSA Bulletin, 132(9–10), 1817-1828.

Axen, G. J., Taylor, W. J., & Bartley, J. M. (1993). Space-time patterns and tectonic controls of Tertiary extension and magmatism in the Great Basin of the western United States. *Geological Society of America Bulletin*, *105*(1), 56-76.

Axen, G. J., & Selverstone, J. (1994). Stress state and fluid-pressure level along the Whipple detachment fault, California. Geology, 22(9), 835-838.

Axen, G. J., Luther, A., & Selverstone, J. (2015). Paleostress directions near two low-angle normal faults: Testing mechanical models of weak faults and off-fault damage. Geosphere, 11(6), 1996-2014.

Axen, G. J., van Wijk, J. W., & Currie, C. A. (2018). Basal continental mantle lithosphere displaced by flat-slab subduction. Nature Geoscience, 11(12), 961-964.

Bailey, I. W., Miller, M. S., Liu, K., & Levander, A. (2012). VS and density structure beneath the Colorado Plateau constrained by gravity anomalies and joint inversions of receiver function and phase velocity data. Journal of Geophysical Research: Solid Earth, 117(B2).

Baldwin, J. A., Powell, R., Brown, M., Moraes, R., & Fuck, R. A. (2005). Modelling of mineral equilibria in ultrahigh-temperature metamorphic rocks from the Anápolis–Itauçu Complex, central Brazil. Journal of Metamorphic Geology, 23(7), 511-531.

Behr, W. M., & Platt, J. P. (2011). A naturally constrained stress profile through the middle crust in an extensional terrane. Earth and Planetary Science Letters, 303(3–4), 181-192. Bulletin, 105(1), 56-76.

Behr, W. M., & Platt, J. P. (2014). Brittle faults are weak, yet the ductile middle crust is strong: Implications for lithospheric mechanics. Geophysical Research Letters, 41(22), 8067-8075.

Beratan, K. K. (1991). Miocene synextension sedimentation patterns, Whipple Mountains, southeastern California: implications for the geometry of the Whipple detachment system. Journal of Geophysical Research: Solid Earth, 96(B7), 12425-12442.

Berman, R. G. (1990). Mixing properties of Ca-Mg-Fe-Mn garnets. American Mineralogist, 75(3–4), 328-344.

Bird, P. (1988). Formation of the Rocky Mountains, western United States: A continuum computer model. Science, 239(4847), 1501-1507.

Block, L., & Royden, L. H. (1990). Core complex geometries and regional scale flow in the lower crust. Tectonics, 9(4), 557-567.

Boettcher, S. S., & Walker, J. D. (1993). Geologic evolution of Iron Mountain, central Mojave Desert, California. Tectonics, 12(2), 372-386.

Bosworth, W., Huchon, P., & McClay, K. (2005). The red sea and gulf of aden basins. Journal of African Earth Sciences, 43(1–3), 334-378.

Broska, I., Petrík, I., & Williams, C. T. (2000). Coexisting monazite and allanite in peraluminous

granitoids of the Tribec Mountains, Western Carpathians. American Mineralogist, 85(1), 22-32.

Brothers, D. S., Driscoll, N. W., Kent, G. M., Harding, A. J., Babcock, J. M., & Baskin, R. L. (2009). Tectonic evolution of the Salton Sea inferred from seismic reflection data. Nature Geoscience, 2(8), 581-584.

Brun, J. P., Sokoutis, D., Tirel, C., Gueydan, F., Van Den Driessche, J., & Beslier, M. O. (2018). Crustal versus mantle core complexes. Tectonophysics, 746, 22-45.

Buck, W. R. (1991). Modes of continental lithospheric extension. Journal of Geophysical Research: Solid Earth, 96(B12), 20161-20178.

Campbell-Stone, E., John, B. E., Foster, D. A., Geissman, J. W., & Livaccari, R. F. (2000). Mechanisms for accommodation of Miocene extension: Low-angle normal faulting, magmatism, and secondary breakaway faulting in the southern Sacramento Mountains, southeastern California. Tectonics, 19(3), 566-587.

Carlson, D. H., Fleck, R., Moye, F. J., & Fox, K. F. (1991). Geology, geochemistry, and isotopic character of the Colville Igneous Complex, northeastern Washington. Journal of Geophysical Research: Solid Earth, 96(B8), 13313-13333.

Carter, T. J., Kohn, B. P., Foster, D. A., Gleadow, A. J., & Woodhead, J. D. (2006). Late-stage evolution of the Chemehuevi and Sacramento detachment faults from apatite (U-Th)/He thermochronometry—Evidence for mid-Miocene accelerated slip. Geological Society of America Bulletin, 118(5-6), 689-709.

Cassel, E. J., Smith, M. E., & Jicha, B. R. (2018). The impact of slab rollback on Earth's surface: Uplift and extension in the hinterland of the North American Cordillera. Geophysical Research Letters, 45(20), 10-996.

Catlos, E. J., Gilley, L. D., & Harrison, T. M. (2002). Interpretation of monazite ages obtained via in situ analysis. Chemical Geology, 188(3–4), 193-215.

Catlos, E. J., Perez, T. J., Lovera, O. M., Dubey, C. S., Schmitt, A. K., & Etzel, T. M. (2020). High-Resolution P-T-Time Paths Across Himalayan Faults Exposed Along the Bhagirathi Transect NW India: Implications for the Construction of the Himalayan Orogen and Ongoing Deformation. Geochemistry, Geophysics, Geosystems, 21(12), e2020GC009353.

Catlos, E. J., Dubey, C. S., & Etzel, T. M. (2022). Imbrication and Erosional Tectonics Recorded by Garnets in the Sikkim Himalayas. Geosciences, 12(4), 146.

Çemen, I., Catlos, E. J., Göğüs, O., & Özerdem, C. (2006). Postcollisional extensional tectonics and exhumation of the Menderes massif in the Western Anatolia extended terrane, Turkey. In Y. Dilek & S. Pavlides (Eds.), Postcollisional tectonics and magmatism in the Mediterranean region and Asia. Geological Society of America. Special Paper, 409 (2006), pp. 353-379 Doi: 10.1130/2006.2409(18)

Chapman, A. D. (2017). The Pelona–Orocopia–Rand and related schists of southern California: A review of the best-known archive of shallow subduction on the planet. International Geology Review, 59(5–6), 664-701.

Chapman, A. D., Rautela, O., Shields, J., Ducea, M. N., & Saleeby, J. (2020). Fate of the lower lithosphere during shallow-angle subduction: The Laramide example. GSA Today, 30(1), 4-10. Cordillera. Geology, 43(10), 919-922.

Chapman, J. B., Ducea, M. N., DeCelles, P. G., & Profeta, L. (2015). Tracking changes in crustal thickness during orogenic evolution with Sr/Y: An example from the North American Cordillera. Geology 2015;; 43 (10): 919–922.

Chapman, J. B., Greig, R., & Haxel, G. B. (2020). Geochemical evidence for an orogenic plateau in the southern US and northern Mexican Cordillera during the Laramide orogeny. Geology, 48(2), 164-168.

Chapman, J. B., Runyon, S. E., Shields, J. E., Lawler, B. L., Pridmore, C. J., Scoggin, S. H., ... & Haxel, G. B. (2021). The north American cordilleran anatectic belt. Earth-Science Reviews, 215, 103576.

Chen, L., Gerya, T., Zhang, Z., Zhu, G., Duretz, T., & Jacoby, W. R. (2013). Numerical modeling of eastern Tibetan-type margin: Influences of surface processes, lithospheric structure and crustal rheology. Gondwana Research, 24(3-4), 1091-1107.

Coney, P. J., Crittenden, M. D., & Davis, G. H. (1980). Cordilleran metamorphic core complexes: An overview. Cordilleran metamorphic core complexes: Geological Society of America Memoir, 153, 7-31.

Coney, P. J., & Harms, T. A. (1984). Cordilleran metamorphic core complexes: Cenozoic extensional relics of Mesozoic compression. Geology, 12(9), 550-554.

Coney, P. J. (1987). The regional tectonic setting and possible causes of Cenozoic extension in the North American Cordillera. Geological Society, London, Special Publications, 28(1), 177-186.

Cooper, F. J., Platt, J. P., Platzman, E. S., Grove, M. J., & Seward, G. (2010). Opposing shear senses in a subdetachment mylonite zone: Implications for core complex mechanics. Tectonics, 29(4).

Cooper, F. J., Platt, J. P., & Behr, W. M. (2017). Rheological transitions in the middle crust: insights from Cordilleran metamorphic core complexes. Solid Earth, 8(1), 199-215.

Coggon, R., & Holland, T. J. B. (2002). Mixing properties of phengitic micas and revised garnet-

phengite thermobarometers. Journal of Metamorphic Geology, 20(7), 683-696.

Cross, A. J., Kidder, S., & Prior, D. J. (2015). Using microstructures and TitaniQ thermobarometry of quartz sheared around garnet porphyroclasts to evaluate microstructural evolution and constrain an Alpine Fault Zone geotherm. Journal of Structural Geology, 75, 17-31.

Crowley, J. L., Brown, R. L., & Parrish, R. R. (2001). Diachronous deformation and a strain gradient beneath the Selkirk allochthon, northern Monashee complex, southeastern Canadian Cordillera. Journal of Structural Geology, 23(6–7), 1103-1121.

Crowley, J. L., Brown, R. L., Gervais, F., & Gibson, H. D. (2008). Assessing inheritance of zircon and monazite in granitic rocks from the Monashee Complex, Canadian Cordillera. Journal of Petrology, 49(11), 1915-1929.

Davis, G. A., Anderson, J. L., Frost, E. G., & Shackelford, T. J. (1980). Mylonitization and detachment faulting in the Whipple-Buckskin-Rawhide Mountains terrane, southeastern California and western Arizona. Geological Society of America Mem., 153, 79–130.

Davis, G. A., Anderson, J. L., Martin, D. L., Krummenacher, D., Frost, E. G., & Armstrong, R. L. (1982). Geologic and geochronologic relations in the lower plate of the Whipple detachment fault, Whipple Mountains, southeastern California: A progress report. In E. G. Frost & D. L. Martin (Eds.), Mesozoic-Cenozoic tectonic evolution of the Colorado River region, California, Arizona, and Nevada (pp. 408–432). San Diego, CA: Cordilleran Publishers.

Davis, G. A., Lister, G. S., & Reynolds, S. J. (1986). Structural evolution of the Whipple and South Mountains shear zones, southwestern United States. Geology, 14(1), 7-10.

Davis, G. A., & Lister, G. S. (1988). Detachment faulting in continental extension; perspectives

from the southwestern US Cordillera. Special Paper. Geological Society of America. 218, 133–159

Davis, G. A. (1988). Rapid upward transport of mid-crustal mylonitic gneisses in the footwall of a Miocene detachment fault, Whipple Mountains, southeastern California. Geologische Rundschau, 77(1), 191-209.

Davis, G. A. (1996). Mesozoic deformation and plutonism in the Yunmeng Shan: A metamorphic core complex north of Beijing, China. Tectonic Evolution of Asia, 253-280.

Davis, G. H., & Coney, P. J. (1979). Geologic development of the Cordilleran metamorphic core complexes. Geology, 7(3), 120-124.

Davis, G. H., Spencer, J. E., & Gehrels, G. E. (2019). Field-trip guide to the Catalina-Rincon metamorphic core complex, Tucson, Arizona. Geologic Excursions in Southwestern North America: Geological Society of America Field Guide, 55, 1-38.

de Capitani, C., & Brown, T. H. (1987). The computation of chemical equilibrium in complex systems containing non-ideal solutions. Geochimica et Cosmochimica Acta, 51(10), 2639-2652.

de Capitani, C., & Petrakakis, K. (2010). The computation of equilibrium assemblage diagrams with Theriak/Domino software. American Mineralogist, 95(7), 1006-1016.

Dewey, J. F. (1988). Extensional collapse of orogens. Tectonics, 7(6), 1123-1139.

DeWitt, E., Sutter, J. F., Davis, G. A., & Anderson, J. L. (1986). 40Ar/39Ar age-spectrum dating of Miocene mylonitic rocks, Whipple Mountains, southeastern California. Geological Society of America Abstracts with Programs (Vol. 18, No. 6, p. 584).

DeWitt, E., & Reynolds, S. J. (1990). Late Cretaceous plutonism and cooling in the Maria fold

and thrust belt, west-central Arizona. In Geol. Soc. Am. Abstr. Programs (Vol. 22, No. 3, p. 18).

Dickey, D. D., Carr, W. J., & Bull, W. B. (1980). Geologic map of the Parker NW, Parker, and parts of the Whipple Mountains SW and Whipple Wash quadrangles, California and Arizona (No. 1124). U.S. Geological Survey

Dickinson, W. R., Ingersoll, R. V., Cowan, D. S., Helmold, K. P., & Suczek, C. A. (1982). Provenance of Franciscan graywackes in coastal California. Geological Society of America Bulletin, 93(2), 95-107.

Dickinson, W. R. (2004). Evolution of the North American Cordillera. Annual Review of Earth and Planetary Sciences, 32, 13-45.

Dickinson, W. R., Kay, S. M., & Ramos, V. A. (2009). Anatomy and global context of the North American Cordillera. Backbone of the Americas: Shallow subduction, plateau uplift, and ridge and terrane collision: Geological Society of America Memoir, 204, 1-29.

Dickinson, W. R., Goodlin, T. C., Grover, J. A., Mark, R. A., & Shafiqullah, M. (1987). Low-angle normal-fault system along the range front of the southwestern Galiuro Mountains in southeastern Arizona. Geology, 15(8), 727-730.

Dickinson, W. R., Snyder, W. S., & Matthews, V. (1978). Plate tectonics of the Laramide orogeny. In V. Matthews III (Ed.), Laramide folding associated with basement block faulting in the western United States (Memoir 151, pp. 355–366). Geological Society of America.

Dorsey, R. J., & Becker, U. L. F. (1995). Evolution of a large Miocene growth structure in the upper plate of the Whipple detachment fault, northeastern Whipple Mountains, California. Basin Research, 7(2), 151-163.

Ducea, M. N., & Chapman, A. D. (2018). Sub-magmatic arc underplating by trench and forearc materials in shallow subduction systems; A geologic perspective and implications. Earth-Science Reviews, 185, 763-779.

Ducea, M. N., Triantafyllou, A., & Krcmaric, J. (2020). New timing and depth constraints for the Catalina metamorphic core complex, southeast Arizona. Tectonics, 39(8), e2020TC006383.

Dumitru, T. A., Gans, P. B., Foster, D. A., & Miller, E. L. (1991). Refrigeration of the western Cordilleran lithosphere during Laramide shallow-angle subduction. Geology, 19(11), 1145-1148.

Elston, D. P., & Young, R. A. (1991). Cretaceous-Eocene (Laramide) landscape development and Oligocene-Pliocene drainage reorganization of transition zone and Colorado Plateau, Arizona. Journal of Geophysical Research: Solid Earth, 96(B7), 12389-12406.

Etzel, T. M., Catlos, E. J., Ataktürk, K., Lovera, O. M., Kelly, E. D., Çemen, I., & Diniz, E. (2019). Implications for thrust-related shortening punctuated by extension from P-T paths and geochronology of garnet-bearing schists, Southern (Çine) Menderes Massif, SW Turkey. Tectonics, 38(6), 1974-1998.

Etzel, T. M., & Catlos, E. J. (2021). Garnet Chemical Zoning Based Thermobarometry: Method evaluation and applications in the Menderes Massif, Western Turkey. Geosciences, 11(12), 505.

Evans, B., Renner, J., & Hirth, G. (2001). A few remarks on the kinetics of static grain growth in rocks. International Journal of Earth Sciences, 90(1), 88-103.

Evans, S. L., Styron, R. H., van Soest, M. C., Hodges, K. V., & Hanson, A. D. (2015). Zircon

and apatite (U-Th)/He evidence for Paleogene and Neogene extension in the southern Snake Range, Nevada, USA. Tectonics, 34(10), 2142-2164.

Faulds, J. E., Feuerbach, D. L., Miller, C. F., & Smith, E. I. (2001). Cenozoic evolution of the northern Colorado River extensional corridor, southern Nevada and northwest Arizona. Pacific Section of the American Association of Petroleum Geologists Publication GB 78. (2001): 239-272.

Fayon, A. K., Peacock, S. M., Stump, E., & Reynolds, S. J. (2000). Fission track analysis of the footwall of the Catalina detachment fault, Arizona: Tectonic denudation, magmatism, and erosion. Journal of Geophysical Research: Solid Earth, 105(B5), 11047-11062.

Fedo, C. M., & Miller, J. M. (1992). Evolution of a Miocene half-graben basin, Colorado River extensional corridor, southeastern California. Geological Society of America Bulletin, 104(4), 481-493.

Ferry, J. T., & Spear, F. S. (1978). Experimental calibration of the partitioning of Fe and Mg between biotite and garnet. Contributions to Mineralogy and Petrology, 66(2), 113-117.

Flansburg, M. E., & Stockli, D. F. (2023). Progressive Miocene unroofing of the Big Maria and Riverside Mountains (southeastern California, USA) along the southwestern margin of the Colorado River extensional corridor. Geosphere, 19(3), 676-694.

Fletcher, I. R., McNaughton, N. J., Davis, W. J., & Rasmussen, B. (2010). Matrix effects and calibration limitations in ion probe U–Pb and Th–Pb dating of monazite. Chemical Geology, 270(1-4), 31-44.

Florence, F. P., & Spear, F. S. (1991). Effects of diffusional modification of garnet growth zoning on PT path calculations. Contributions to Mineralogy and Petrology, 107(4), 487-500.

Flueh, E. R., & Okaya, D. A. (1989). Near-vertical and intermediate offset seismic reflection data from west of the Whipple Mountains, SE California. Journal of Geophysical Research: Solid Earth, 94(B1), 625-636.

Fornash, K. F., Patchett, P. J., Gehrels, G. E., & Spencer, J. E. (2013). Evolution of granitoids in the Catalina metamorphic core complex, southeastern Arizona: U–Pb, Nd, and Hf isotopic constraints. Contributions to Mineralogy and Petrology, 165(6), 1295-1310.

Foster, D. A. (1989). Mesozoic and Cenozoic thermal history of the eastern Mojave Desert, California and western Arizona, with emphasis on the Old Woman Mountains area and the Chemehuevi metamorphic core complex. State University of New York, Albany, NY (United States).

Foster, D. A., Gleadow, A. J., Reynolds, S. J., & Fitzgerald, P. G. (1993). Denudation of metamorphic core complexes and the reconstruction of the transition zone, west central Arizona: Constraints from apatite fission track thermochronology. Journal of Geophysical Research: Solid Earth, 98(B2), 2167-2185.

Foster, D. A., & John, B. E. (1999). Quantifying tectonic exhumation in an extensional orogen with thermochronology: examples from the southern Basin and Range Province. Geological Society, London, Special Publications, 154(1), 343-364.

Gaidies, F., De Capitani, C., & Abart, R. (2008). THERIA_G: a software program to numerically model prograde garnet growth. Contributions to Mineralogy and Petrology, 155, 657-671.

Ganguly, J. (2010). Cation diffusion kinetics in aluminosilicate garnets and geological applications. Reviews in Mineralogy and Geochemistry, 72(1), 559-601.

Gans, P., Miller, E. L., McCarthy, J., & Ouldcott, M. L. (1985). Tertiary extensional faulting and

evolving ductile-brittle transition zones in the northern Snake Range and vicinity: New insights from seismic data. Geology, 13(3), 189-193.

Gans, P. B., & Gentry, B. J. (2016). Dike emplacement, footwall rotation, and the transition from magmatic to tectonic extension in the Whipple Mountains metamorphic core complex, southeastern California. Tectonics, 35(11), 2564-2608.

Gibbs, A. D. (1984). Structural evolution of extensional basin margins. Journal of the Geological Society, 141(4), 609-620.

Gervais, F., Brown, R. L., & Crowley, J. L. (2010). Tectonic implications for a Cordilleran orogenic base in the Frenchman Cap dome, southeastern Canadian Cordillera. Journal of Structural Geology, 32(7), 941-959.

Gessner, K., Ring, U., Johnson, C., Hetzel, R., Passchier, C. W., & Güngör, T. (2001). An active bivergent rolling-hinge detachment system: Central Menderes metamorphic core complex in western Turkey. Geology, 29(7), 611-614.

Gébelin, A., Mulch, A., Teyssier, C., Heizler, M., Vennemann, T., & Seaton, N. C. (2011). Oligo-Miocene extensional tectonics and fluid flow across the Northern Snake Range detachment system, Nevada. Tectonics, 30(5).

Goodwin, L. B., & Haxel, G. B. (1990). Structural evolution of the Southern Baboquivari Mountains, south-central Arizona and north-central Sonora. Tectonics, 9(5), 1077-1095.

González-Becuar, E., Pérez-Segura, E., Vega-Granillo, R., Solari, L., González-León, C. M., Solé, J., & López Martínez, M. (2017). Laramide to Miocene syn-extensional plutonism in the Puerta del Sol area, central Sonora, Mexico. Revista Mexicana de Ciencias Geológicas, 34(1), 45-61.

González-León, C. M., Solari, L., Solé, J., Ducea, M. N., Lawton, T. F., Bernal, J. P., &

Santacruz, R. L. (2011). Stratigraphy, geochronology, and geochemistry of the Laramide magmatic arc in north-central Sonora, Mexico. Geosphere, 7(6), 1392-1418.

Gordon, S. M., Whitney, D. L., Teyssier, C., Grove, M., & Dunlap, W. J. (2008). Timescales of migmatization, melt crystallization, and cooling in a Cordilleran gneiss dome: Valhalla complex, southeastern British Columbia. Tectonics, 27(4).

Gottlieb, E. S. (2017). Geologic insights from zircon inheritance (Doctoral dissertation). Stanford University.

Gottardi, R., Schaper, M. C., Barnes, J. D., & Heizler, M. T. (2018). Fluid–rock interaction and strain localization in the Picacho Mountains detachment shear zone, Arizona, USA. Tectonics, 37(9), 3244-3260.

Gottardi, R., McAleer, R., Casale, G., Borel, M., Iriondo, A., & Jepson, G. (2020). Exhumation of the Coyote Mountains metamorphic core complex (Arizona): Implications for orogenic collapse of the southern North American Cordillera. Tectonics, 39(8), e2019TC006050.

Grove, M., Jacobson, C. E., Barth, A. P., Vucic, A., Johnson, S. E., Paterson, S. R., et al. (2003). Temporal and spatial trends of Late Cretaceous-early Tertiary underplating of Pelona and related schist beneath southern California and southwestern Arizona. Geological Society of America Special Papers, 374: 381–406.

Gueydan, F., Morency, C., & Brun, J. P. (2008). Continental rifting as a function of lithosphere mantle strength. Tectonophysics, 460(1–4), 83-93.

Hacker, B. R., Yin, A., Christie, J. M., & Davis, G. A. (1992). Stress magnitude, strain rate, and rheology of extended middle continental crust inferred from quartz grain sizes in the Whipple Mountains, California. Tectonics, 11(1), 36-46.

Hallett, B. W., & Spear, F. S. (2014). The P–T history of anatectic pelites of the Northern East

Humboldt Range, Nevada: Evidence for tectonic loading, decompression, and anatexis. Journal of Petrology, 55(1), 3-36.

Hallett, B. W., & Spear, F. S. (2015). Monazite, zircon, and garnet growth in migmatitic pelites as a record of metamorphism and partial melting in the East Humboldt Range, Nevada. American Mineralogist, 100(4), 951-972.

Hansen, V. L. & Goodge, J. W. (1988). Metamorphism, structural petrology, and regional evolution of the Okanogan complex, northeastern Washington. Paper presented at the Rubey Colloquium on Metamorphism and Crustal Evolution of the Western United States.

Harrison, T. M., Copeland, P., Kidd, W. S. F., & Lovera, O. M. (1995). Activation of the Nyainqentanghla shear zone: Implications for uplift of the southern Tibetan Plateau. Tectonics, 14(3), 658-676.

Hauser, E. C., & Lundy, J. (1989). COCORP deep reflections: Moho at 50 km (16 s) beneath the Colorado Plateau. Journal of Geophysical Research: Solid Earth, 94(B6), 7071-7081.

Haxel, G. B., Jacobson, C. E., & Wittke, J. H. (2015). Mantle peridotite in newly discovered far-inland subduction complex, southwest Arizona: Initial report. International Geology Review, 57(5–8), 871-892.

Hayama, Y., Shibata, K., & Takeda, H. (1984). K-Ar ages of the low-grade metamorphic rocks in the Altar massif, northwest Sonora, Mexico. Chishitsugaku Zasshi;(Japan), 90(8). 589-596

Hempton, M. R. (1987). Constraints on Arabian plate motion and extensional history of the Red Sea. Tectonics, 6(6), 687-705.

Henry, C. D., McGrew, A. J., Colgan, J. P., Snoke, A. W., & Brueseke, M. E. (2011). Timing,

distribution, amount, and style of Cenozoic extension in the northern Great Basin. Field Guides, v. 21." (2011): 27-66.

Henyey, T. E., Okaya, D. A., Frost, E. G., & McEvilly, T. V. (1987). CALCRUST (1985) seismic reflection survey, Whipple Mountains detachment terrane, California: an overview. Geophysical Journal International, 89(1), 111-118.

Hildebrand, R. S. (2013). Mesozoic assembly of the North American cordillera (Vol. 495). Geological society of America.shear zone: Implications for uplift of the southern Tibetan Plateau. Tectonics, 14(3), 658-676.

Hiraga, T., Tachibana, C., Ohashi, N., & Sano, S. (2010). Grain growth systematics for forsterite±enstatite aggregates: Effect of lithology on grain size in the upper mantle. Earth and Planetary Science Letters, 291(1–4), 10-20.

Hodges, K. V., Snoke, A. W., & Hurlow, H. A. (1992). Thermal evolution of a portion of the Sevier hinterland: The northern Ruby Mountains-East Humboldt range and Wood Hills, northeastern Nevada. Tectonics, 11(1), 154-164.

Hoisch, T. D. (1989). A muscovite-biotite geothermometer. American Mineralogist, 74(5–6), 565-572.

Hoisch, T. D. (1990). Empirical calibration of six geobarometers for the mineral assemblage quartz+ muscovite+ biotite+ plagioclase+ garnet. Contributions to Mineralogy and Petrology, 104(2), 225-234.

Holk, G. J., & Taylor Jr, H. P. (2000). Water as a petrologic catalyst driving 18O/16O homogenization and anatexis of the middle crust in the metamorphic core complexes of British Columbia. International Geology Review, 42(2), 97-130.

Holland, E. C., Hively, W. P., DePinho, R. A., & Varmus, H. E. (1998). A constitutively active

epidermal growth factor receptor cooperates with disruption of G1 cell-cycle arrest pathways to induce glioma-like lesions in mice. Genes & Development, 12(23), 3675-3685.

Holland, T. J. B., & Powell, R. T. J. B. (1998). An internally consistent thermodynamic data set for phases of petrological interest. Journal of Metamorphic Geology, 16(3), 309-343.

Holland, T., & Powell, R. (2003). Activity–composition relations for phases in petrological calculations: an asymmetric multicomponent formulation. Contributions to Mineralogy and Petrology, 145(4), 492-501.

Howard, K. A., Goodge, J. W., & John, B. E. (1982). Detached crystalline rocks of the Mohave, Buck, and Bill Williams mountains, western Arizona. E.G Frost, D.L Martin (Eds.), Mesozoic-Cenozoic Tectonic Evolution of the Colorado River Region, California, Arizona and Nevada, Cordilleran Publishers, San Diego, California (1982), pp. 377-390

Howard, K. A., & John, B. E. (1987). Crustal extension along a rooted system of imbricate low-angle faults: Colorado River extensional corridor, California and Arizona. Geological Society, London, Special Publications, 28(1), 299-311.

Howard, K. A., Nielson, J. E., Wilshire, W. G., Nakata, J. K., Goodge, J. W., Reneau, S. L., et al. (1999). Geologic map of the Mohave Mountains area, Mohave County, western Arizona (Map I-2308, scale 1: 48,000). U.S. Geological Survey.

Howard, K. A., Wooden, J. L., Barnes, C. G., Premo, W. R., Snoke, A. W., & Lee, S. Y. (2011). Episodic growth of a Late Cretaceous and Paleogene intrusive complex of pegmatitic leucogranite, Ruby Mountains core complex, Nevada, USA. Geosphere, 7(5), 1220-1248.

Huet, B., Le Pourhiet, L., Labrousse, L., Burov, E., & Jolivet, L. (2011). Post-orogenic extension

and metamorphic core complexes in a heterogeneous crust: The role of crustal layering inherited from collision. Application to the Cyclades (Aegean domain). Geophysical Journal International, 184(2), 611-625.

Jacobson, C. E., Oyarzabal, F. R., & Haxel, G. B. (1996). Subduction and exhumation of the Pelona-Orocopia-Rand schists, southern California. Geology, 24(6), 547-550.

Jacobson, C. E., Hourigan, J. K., Haxel, G. B., & Grove, M. (2017). Extreme latest Cretaceous–Paleogene low-angle subduction: Zircon ages from Orocopia Schist at Cemetery Ridge, southwestern Arizona, USA. Geology, 45(10), 951-954.

Jacobson, C. E., Jacques-Ayala, C., Barth, A. P., y Barragán, J. C. G., Pedrick, J. N., & Wooden, J. L. (2019). Protolith age of the Altar and Carnero complexes and Late Cretaceous–Miocene deformation in the Caborca–Altar region of northwestern Sonora, Mexico. Revista Mexicana de Ciencias Geológicas, 36(1), 95-109. https://doi.org/10.22201/cgeo.20072902e.2019.1.784

John, B. E., & Wooden, J. (1990). Petrology and geochemistry of the metaluminous to peraluminous Chemehuevi Mountains Plutonic Suite, southeastern California. The Nature and Origin of Cordilleran Magmatism. Geological Society of America Memoirs, 174, 71-98.

Kapp, P., Yin, A., Manning, C. E., Murphy, M., Harrison, T. M., Spurlin, M., ... & Cun-Ming, W. (2000). Blueschist-bearing metamorphic core complexes in the Qiangtang block reveal deep crustal structure of northern Tibet. Geology, 28(1), 19-22.

Kapp, P., Taylor, M., Stockli, D., & Ding, L. (2008). Development of active low-angle normal fault systems during orogenic collapse: Insight from Tibet. Geology, 36(1), 7-10.

Kapp, P., Jepson, G., Carrapa, B., Schaen, A. J., He, J. J., & Wang, J. W. (2023). Laramide

bulldozing of lithosphere beneath the Arizona transition zone, southwestern United States. Geology, 51(10), 952-956.

King, E. M., Valley, J. W., Stockli, D. F., & Wright, J. E. (2004). Oxygen isotope trends of granitic magmatism in the Great Basin: Location of the Precambrian craton boundary as reflected in zircons. Geological Society of America Bulletin, 116(3–4), 451-462.

Kohlstedt, D. L., Evans, B., & Mackwell, S. J. (1995). Strength of the lithosphere: Constraints imposed by laboratory experiments. Journal of Geophysical Research: Solid Earth, 100(B9), 17587-17602.

Kohn, M. J. (1993). Uncertainties in differential thermodynamic (Gibbs' method) PT paths. Contributions to Mineralogy and Petrology, 113(1), 24-39.

Kohn, M. J., & Spear, F. S. (1991). Error propagation for barometers; 1, Accuracy and precision of experimentally located end-member reactions. American Mineralogist, 76(1–2), 128-137.

Kohn, M. J., Catlos, E. J., Ryerson, F. J., & Harrison, T. M. (2001). Pressure-temperature-time path discontinuity in the Main Central thrust zone, central Nepal. Geology, 29(7), 571-574.

Korchinski, M., Rey, P. F., Mondy, L., Teyssier, C., & Whitney, D. L. (2018). Numerical investigation of deep-crust behavior under lithospheric extension. Tectonophysics, 726, 137-146.

Korchinski, M., Teyssier, C., Rey, P. F., Whitney, D. L., & Mondy, L. (2021). Single-phase vs two-phase rifting: numerical perspectives on the accommodation of extension during continental break-up. Marine and Petroleum Geology, 123, 104715.

Kuniyoshi, S., & Freeman, T. (1974). Potassium-argon ages of Tertiary volcanic rocks from the

eastern Mojave Desert. Geological Society of America Abstracts with Programs (Vol. 6, No. 3, p. 204).

Kruckenberg, S. C., Whitney, D. L., Teyssier, C., Fanning, C. M., & Dunlap, W. J. (2008). Paleocene-Eocene migmatite crystallization, extension, and exhumation in the hinterland of the northern Cordillera: Okanogan dome, Washington, USA. Geological Society of America Bulletin, 120(7–8), 912-929.

Lavier, L. L., & Manatschal, G. (2006). A mechanism to thin the continental lithosphere at magma-poor margins. Nature, 440(7082), 324-328.

Lanari, P., & Engi, M. (2017). Local bulk composition effects on metamorphic mineral assemblages. Reviews in Mineralogy and Geochemistry, 83(1), 55-102.

Lanari, P., & Duesterhoeft, E. (2019). Modeling metamorphic rocks using equilibrium thermodynamics and internally consistent databases: Past achievements, problems and perspectives. Journal of Petrology, 60(1), 19-56.

Lee, D. E., & Christiansen, E. H. (1983). The granite problem as exposed in the southern Snake Range, Nevada. Contributions to Mineralogy and Petrology, 83(1–2), 99-116.

Lee, S. Y., Barnes, C. G., Snoke, A. W., Howard, K. A., & Frost, C. D. (2003). Petrogenesis of Mesozoic, peraluminous granites in the Lamoille Canyon area, Ruby Mountains, Nevada, USA. Journal of Petrology, 44(4), 713-732.

Lee, J., Blackburn, T., & Johnston, S. (2017). Timing of mid-crustal ductile extension in the northern Snake Range metamorphic core complex, Nevada: Evidence from U/Pb zircon ages. Geosphere, 13(2), 439-459.

Levy, D. A., Zuza, A. V., Haproff, P. J., & Odlum, M. L. (2021). Early Permian tectonic

evolution of the Last Chance thrust system: An example of induced subduction initiation along a plate boundary transform. GSA Bulletin, 133(5–6), 1105-1127.

Livaccari, R. F., Burke, K., & Şengör, A. M. C. (1981). Was the Laramide orogeny related to subduction of an oceanic plateau?. Nature, 289(5795), 276-278.

Livaccari, R. F., & Perry, F. V. (1993). Isotopic evidence for preservation of Cordilleran lithospheric mantle during the Sevier-Laramide orogeny, western United States. Geology, 21(8), 719-722.

Lister, G. S., Banga, G., & Feenstra, A. (1984). Metamorphic core complexes of Cordilleran type in the Cyclades, Aegean Sea, Greece. Geology, 12(4), 221-225.

Lister, G. S., Etheridge, M. A., & Symonds, P. A. (1986). Detachment faulting and the evolution of passive continental margins. Geology, 14(3), 246-250.

Lister, G. S., & Davis, G. A. (1989). The origin of metamorphic core complexes and detachment faults formed during Tertiary continental extension in the northern Colorado River region, USA. Journal of Structural Geology, 11(1–2), 65-94.

Lister, G. S., Etheridge, M. A., & Symonds, P. A. (1991). Detachment models for the formation of passive continental margins. Tectonics, 10(5), 1038-1064.

Long, K. B., Gehrels, G. E., & Baldwin, S. L. (1995). Tectonothermal evolution of the Pinaleno-Jackson Mountain core complex, southeast Arizona. Geological Society of America Bulletin, 107(10), 1231-1240.

Lutz, B. M., Ketcham, R. A., Axen, G. J., Beyene, M. A., Wells, M. L., van Wijk, J. W., & Ross, J. I. (2021). Thermo-kinematic modeling of detachment-dominated extension, northeastern Death Valley area, USA: Implications for mid-crustal thermal-rheological evolution. Tectonophysics, 808, 228755.

Mahar, E. M., Baker, J. M., Powell, R., Holland, T. J. B., & Howell, N. (1997). The effect of Mn on mineral stability in metapelites. Journal of Metamorphic Geology, 15(2), 223-238.

Mallery, C., Barth, A., Roldan-Quintana, J., Haxel, G., Wooden, J., & Jacobson, C. (2018). A geochemical model for the origin of the Pan Tak granite, the granite of Presumido Peak & the granite of Sierra San Juan during the laramide orogeny, Southern Arizona & Northern Sonora. Paper presented at the GSA Annual Meeting in Indianapolis, Indiana.

Matthews, A. (1994). Oxygen isotope geothermometers for metamorphic rocks. Journal of Metamorphic Geology, 12(3), 211-219.

McCarthy, J., Larkin, S. P., Fuis, G. S., Simpson, R. W., & Howard, K. A. (1991). Anatomy of a metamorphic core complex: Seismic refraction/wide-angle reflection profiling in southeastern California and western Arizona. Journal of Geophysical Research: Solid Earth, 96(B7), 12259-12291.

McGrew, A. J., & Snee, L. W. (1994). 40Ar/39Ar thermochronologic constraints on the tectonothermal evolution of the northern East Humboldt Range metamorphic core complex, Nevada. Tectonophysics, 238(1–4), 425-450.

McNulty, B., & Farber, D. (2002). Active detachment faulting above the Peruvian flat slab. Geology, 30(6), 567-570.

Melosh, H. J. (1990). Mechanical basis for low-angle normal faulting in the Basin and Range province. Nature, 343(6256), 331-335.

Miller, C. F., & Bradfish, L. J. (1980). An inner Cordilleran belt of muscovite-bearing plutons. Geology, 8(9), 412-416.

Miller, E. L., Gans, P. B., & Garing, J. (1983). The Snake Range decollement: An exhumed mid-Tertiary ductile-brittle transition. Tectonics, 2(3), 239-263.

Miller, E. L., & Gans, P. B. (1989). Cretaceous crustal structure and metamorphism in the hinterland of the Sevier thrust belt, western US Cordillera. Geology, 17(1), 59-62.

Miller, J. M., & John, B. E. (1988). Detached strata in a Tertiary low-angle normal fault terrane, southeastern California: A sedimentary record of unroofing, breaching, and continued slip. Geology, 16(7), 645-648.

Miller, J. M., & John, B. E. (1999). Sedimentation patterns support seismogenic low-angle normal faulting, southeastern California and western Arizona. Geological Society of America Bulletin, 111(9), 1350-1370.

Molnar, P., & Tapponnier, P. (1975). Cenozoic Tectonics of Asia: Effects of a Continental Collision: Features of recent continental tectonics in Asia can be interpreted as results of the India-Eurasia collision. Science, 189(4201), 419-426.

Molnar, P., & Tapponnier, P. (1978). Active tectonics of Tibet. Journal of Geophysical Research: Solid Earth, 83(B11), 5361-5375.

Morley, C. K. (1989). Extension, detachments, and sedimentation in continental rifts (with particular reference to East Africa). Tectonics, 8(6), 1175-1192.

Morrison, J. (1994). Downward circulation of meteoric water into the lower plate of the Whipple Mountains metamorphic core complex, California. Journal of Metamorphic Geology, 12, 827-840.

Morrison, J., & Anderson, J. L. (1998). Footwall refrigeration along a detachment fault: Implications for the thermal evolution of core complexes. Science, 279(5347), 63-66.

Moynihan, D. P., & Pattison, D. R. M. (2013). An automated method for the calculation of P–T paths from garnet zoning, with application to metapelitic schist from the Kootenay Arc, British Columbia, Canada. Journal of Metamorphic Geology, 31(5), 525-548.

Murphy, M. A., Yin, A., Kapp, P., Harrison, T. M., Manning, C. E., Ryerson, F. J., ... & Jinghui, G. (2002). Structural evolution of the Gurla Mandhata detachment system, southwest Tibet: Implications for the eastward extent of the Karakoram fault system. Geological Society of America Bulletin, 114(4), 428-447.

Nielson, J. E., & Beratan, K. K. (1990). Tertiary basin development and tectonic implications, Whipple detachment system, Colorado River extensional corridor, California and Arizona. Journal of Geophysical Research: Solid Earth, 95(B1), 599-614.

Nielson, J. E., & Beratan, K. K. (1995). Stratigraphic and structural synthesis of a Miocene extensional terrane, southeast California and west-central Arizona. Geological Society of America Bulletin, 107(2), 241-252.

Nourse, J. A., Anderson, T. H., & Silver, L. T. (1994). Tertiary metamorphic core complexes in Sonora, northwestern Mexico. Tectonics, 13(5), 1161-1182.

Pease, V., Foster, D., Wooden, J., O'Sullivan, P., Argent, J., & Fanning, C. (1999). The Northern Sacramento Mountains, southwest United States. Part II: Exhumation history and detachment faulting. Geological Society, London, Special Publications, 164(1), 199-238.

Peterman, E. M., Hourigan, J. K., & Grove, M. (2014). Experimental and geologic evaluation of monazite (U–Th)/He thermochronometry: Catnip Sill, Catalina Core Complex, Tucson, AZ. Earth and Planetary Science Letters, 403, 48-55.

Powell, R., & Holland, T. (1999). Relating formulations of the thermodynamics of mineral solid solutions; activity modeling of pyroxenes, amphiboles, and micas. American Mineralogist, 84(1–2), 1-14.

Prior, M. G., Stockli, D. F., & Singleton, J. S. (2016). Miocene slip history of the Eagle Eye

detachment fault, Harquahala Mountains metamorphic core complex, west-central Arizona. Tectonics, 35(8), 1913-1934.

Prior, M. G., Singleton, J. S., & Stockli, D. F. (2018). Late-stage slip history of the Buckskin-Rawhide detachment fault and temporal evolution of the Lincoln Ranch supradetachment basin: New constraints from the middle Miocene Sandtrap Conglomerate. GSA Bulletin, 130(9–10), 1747-1760.

Reston, T. J., Krawczyk, C. M., & Klaeschen, D. (1996). The S reflector west of Galicia (Spain): Evidence from prestack depth migration for detachment faulting during continental breakup. Journal of Geophysical Research: Solid Earth, 101(B4), 8075-8091.

Robinson, D., Bevins, R. E., Aguirre, L., & Vergara, M. (2004). A reappraisal of episodic burial metamorphism in the Andes of central Chile. Contributions to Mineralogy and Petrology, 146(4), 513-528.

Rey, P. F., Teyssier, C., & Whitney, D. L. (2009). Extension rates, crustal melting, and core complex dynamics. Geology, 37(5), 391-394.

Rey, P. F., Teyssier, C., Kruckenberg, S. C., & Whitney, D. L. (2011). Viscous collision in channel explains double domes in metamorphic core complexes. Geology, 39(4), 387-390.

Reynolds, S. J., & Spencer, J. E. (1985). Evidence for large-scale transport on the Bullard detachment fault, west-central Arizona. Geology, 13(5), 353-356.

Richard, S. M., Fryxell, J. E., & Sutter, J. F. (1990). Tertiary structure and thermal history of the Harquahala and Buckskin Mountains, west central Arizona: Implications for denudation by a major detachment fault system. Journal of Geophysical Research: Solid Earth, 95(B12), 19973-19987.

J. Roldán-Quintana. (1991). Geology and chemical composition of the Jaralito and Aconchi

batholiths in east-central Sonora, México E. Perez-Segura, C. Jacques-Ayala (Eds.), Studies of Sonoran Geology: Geological Society of America Special Paper, 254, 69-80

Saleeby, J. (2003). Segmentation of the Laramide slab—Evidence from the southern Sierra Nevada region. Geological Society of America Bulletin, 115(6), 655-668.

Schaper, M. C. (2016). Fluid-rock Interaction within the Picacho Mountains Detachment Shear Zone. University of Louisiana at Lafayette. Proquest Dissertations and Theses, 91.

Schenker, F. L., Gerya, T., & Burg, J. P. (2012). Bimodal behavior of extended continental lithosphere: Modeling insight and application to thermal history of migmatitic core complexes. Tectonophysics, 579, 88-103.

Scoggin, S. H. (2022). Cenozoic tectonic evolution of the Pinaleño Mountains region, Southeastern Arizona (Doctoral dissertation). University of Wyoming.

Selverstone, J., Axen, G. J., & Luther, A. (2012). Fault localization controlled by fluid infiltration into mylonites: Formation and strength of low-angle normal faults in the midcrustal brittle-plastic transition. Journal of Geophysical Research: Solid Earth, 117(B6).

Seymour, N. M., Strickland, E. D., Singleton, J. S., Stockli, D. F., & Wong, M. S. (2018). Laramide subduction and metamorphism of the Orocopia Schist, northern Plomosa Mountains, west-central Arizona: Insights from zircon U-Pb geochronology. Geology, 46(10), 847-850.

Seymour, N. M., Wong, M., & Singleton, J. S. (2016). TitaniQ analyses of mylonites from metamorphic core complexes in west-central Arizona: implications for two phases of extension in the lower Colorado River Extensional Corridor. Paper presented at the AGU Fall Meeting.

Shafiqullah, M., Damon, P. E., Lynch, D. J., Reynolds, S. J., Rehrig, W. A., & Raymond, R. H. (1980). K-Ar geochronology and geologic history of southwestern Arizona and adjacent areas. Studies in western Arizona: Arizona Geological Society Digest, 12, 201-260.

Silverberg, D. S. (1990). The tectonic evolution of the Pioneer metamorphic core complex, south-central Idaho (Doctoral dissertation). Massachusetts Institute of Technology.

Singleton, J. S., Seymour, N. M., & Strickland, E. D. (2022). The Buckskin-Rawhide and northern Plomosa Mountains metamorphic core complexes, west-central Arizona, USA. (Vol. 63). Field Excursions from Las Vegas, Nevada: Guides to the 2022 GSA Cordilleran and Rocky Mountain Joint Section Meeting, Ganqing Jiang, Carol Dehler

Sleep, N. H. (1971). Thermal effects of the formation of Atlantic continental margins by continental break up. Geophysical Journal International, 24(4), 325-350.

Smith, H. A., & Barreiro, B. (1990). Monazite U-Pb dating of staurolite grade metamorphism in pelitic schists. Contributions to Mineralogy and Petrology, 105(5), 602-615.

Spear, F. S. (1993). Metamorphic phase equilibria and pressure-temperature-time paths. Mineralogical Society of America Monograph, 352-356.

Spear, F. S., & Peacock, S. M. (1989). Metamorphic pressure-temperature-time paths (Vol. 7). American Geophysical Union.

Spear, F. S., & Parrish, R. R. (1996). Petrology and cooling rates of the Valhalla complex, British Columbia, Canada. Journal of Petrology, 37(4), 733-765.

Spear, F. S. (2004). Fast cooling and exhumation of the Valhalla metamorphic core complex, southeastern British Columbia. International Geology Review, 46(3), 193-209.

J.E. Spencer, C.E. Isachsen, C.A. Ferguson, S.M. Richard, S.J. Skotnicki, J. Wooden, N.R. Riggs

U-Pb isotope geochronologic data from 23 igneous rock units in cenrtal and southeastern Arizona. Arizona Geol. Surv. Open File Rep. (2003), p. 40

Spencer, J. E. (2006). Application of critical-taper theory to Oligo-Miocene extension and core-complex exhumation in Western Arizona, USA. Paper presented at the AGU Fall Meeting.

Spencer, J. E., & Reynolds, S. J. (1990). Relationship between Mesozoic and Cenozoic tectonic features in west central Arizona and adjacent southeastern California. Journal of Geophysical Research: Solid Earth, 95(B1), 539-555.

Spencer, J. E., Singleton, J. S., Strickland, E., Reynolds, S. J., Love, D., Foster, D. A., & Johnson, R. (2018). Geodynamics of Cenozoic extension along a transect across the Colorado River extensional corridor, southwestern USA. Lithosphere, 10(6), 743-759.

Stern, R. A., & Berman, R. G. (2001). Monazite U–Pb and Th–Pb geochronology by ion microprobe, with an application to in situ dating of an Archean metasedimentary rock. Chemical Geology, 172(1-2), 113-130.

Stockli, D. F., Brichau, S., Dewane, T. J., Hager, C., & Schroeder, J. (2006). Dynamics of large-magnitude extension in the Whipple Mountains metamorphic core complex. Geochimica et Cosmochimica Acta. Supplement., 70(18), A616-A616.

Stone, P., Howard, K.A & Hamilton, W. (1983) Correlation of metamorphosed Paleozoic strata of the southeastern Mojave Desert region, California and Arizona, Geological Society of America Bulletin, 94, 1135-1147.

Strickland, E. D., Singleton, J. S., & Haxel, G. B. (2018). Orocopia Schist in the northern Plomosa Mountains, west-central Arizona: A Laramide subduction complex exhumed in a Miocene metamorphic core complex. Lithosphere, 10(6), 723-742.

Suneson, N. H., & Lucchitta, I. (1983). Origin of bimodal volcanism, southern Basin and Range

province, west-central Arizona. Geological Society of America Bulletin, 94(8), 1005-1019.

Tasaka, M., Zimmerman, M. E., & Kohlstedt, D. L. (2017). Rheological weakening of olivine+ orthopyroxene aggregates due to phase mixing: 1. Mechanical behavior. Journal of Geophysical Research: Solid Earth, 122(10), 7584-7596.

Terrien, J. J. (2012). The role of magmatism in the Catalina metamorphic core complex, Arizona: insights from integrated thermochronology, gravity and aeromagnetic data (Doctoral dissertation). Syracuse University.

Tirel, C., Brun, J. P., & Burov, E. (2008). Dynamics and structural development of metamorphic core complexes. Journal of Geophysical Research: Solid Earth, 113(B4), B04403

Tracy, R. J., Robinson, P., & Thompson, A. B. (1976). Garnet composition and zoning in the determination of temperature and pressure of metamorphism, central Massachusetts. American Mineralogist, 61(7–8), 762-775.

Vogl, J. J., Foster, D. A., Fanning, C. M., Kent, K. A., Rodgers, D. W., & Diedesch, T. (2012). Timing of extension in the Pioneer metamorphic core complex with implications for the spatial-temporal pattern of Cenozoic extension and exhumation in the northern US Cordillera. Tectonics, 31(1), 31

Wells, M. L., & Hoisch, T. D. (2008). The role of mantle delamination in widespread Late Cretaceous extension and magmatism in the Cordilleran orogen, western United States. Geological Society of America Bulletin, 120(5–6), 515-530.

Wells, M. L., Hoisch, T. D., Cruz-Uribe, A. M., & Vervoort, J. D. (2012). Geodynamics of synconvergent extension and tectonic mode switching: Constraints from the Sevier-Laramide orogen. Tectonics, 31(1).

Wernicke, B. (1985). Uniform-sense normal simple shear of the continental lithosphere.

Canadian Journal of Earth Sciences, 22(1), 108-125.

Wernicke, B. P., England, P. C., Sonder, L. J., & Christiansen, R. L. (1987). Tectonomagmatic evolution of Cenozoic extension in the North American Cordillera. Geological Society, London, Special Publications, 28(1), 203-221.

Wernicke, B., & Axen, G. J. (1988). On the role of isostasy in the evolution of normal fault systems. Geology, 16(9), 848-851.

Wernicke, B. (1995). Low-angle normal faults and seismicity: A review. Journal of Geophysical Research: Solid Earth, 100(B10), 20159-20174.

Westaway, R. (1999). The mechanical feasibility of low-angle normal faulting. Tectonophysics, 308(4), 407-443.

White, R., & McKenzie, D. (1989). Magmatism at rift zones: the generation of volcanic continental margins and flood basalts. Journal of Geophysical Research: Solid Earth, 94(B6), 7685-7729.

White, R. W., Powell, R., Holland, T. J. B., & Worley, B. A. (2000). The effect of TiO2 and Fe2O3 on metapelitic assemblages at greenschist and amphibolite facies conditions: mineral equilibria calculations in the system K2O-FeO-MgO-Al2O3-SiO2-H2O-TiO2-Fe2O3. Journal of Metamorphic Geology, 18(5), 497-511.

White, R. W., Powell, R., & Johnson, T. E. (2014). The effect of Mn on mineral stability in metapelites revisited: New a–x relations for manganese-bearing minerals. Journal of Metamorphic Geology, 32(8), 809-828.

Whitney, D. L., Teyssier, C., Rey, P., & Buck, W. R. (2013). Continental and oceanic core complexes. Bulletin, 125(3–4), 273-298.

Wilson, J. T. (1966). Did the Atlantic close and then re-open? London, Macmillan & Co, 1966. Royal8vo. Bound in contemporary full cloth. In "Nature", Vol. 211, 1966. Bookplate to front free end-paper and library stamp to title page. A very fine and clean copy. pp. 676-81. [Entire volume: LV, (1), 1432 pp.]

Wong, M. S., & Gans, P. B. (2008). Geologic, structural, and thermochronologic constraints on the tectonic evolution of the Sierra Mazatán core complex, Sonora, Mexico: New insights into metamorphic core complex formation. Tectonics, 27(4): TC4013.

Wong, M. S., Gans, P. B., & Scheier, J. (2010). The 40Ar/39Ar thermochronology of core complexes and other basement rocks in Sonora, Mexico: Implications for Cenozoic tectonic evolution of northwestern Mexico. Journal of Geophysical Research: Solid Earth, 115(B7): B07414.

Wong, M. S., O'Brien, H. P., Bunting, K. C., & Gans, P. B. (2011). 40Ar/39Ar K-feldspar thermochronology of the Harcuvar core complex, western Arizona: New insight into the timing of extension and degree of footwall tilt. In Geol. Soc. Am. Abstr. Program (Vol. 43, p. 53).

Wong, M. S., Singleton, J. S., Seymour, N. M., Gans, P. B., & Wrobel, A. J. (2023). Late Cretaceous-Early Paleogene Extensional Ancestry of the Harcuvar and Buckskin-Rawhide Metamorphic Core Complexes, Western Arizona. Tectonics, 42(2), e2022TC007656.

Worthington, J. R., Ratschbacher, L., Stübner, K., Khan, J., Malz, N., Schneider, S., ... & Gadoev, M. (2020). The Alichur dome, South Pamir, western India–Asia collisional zone: Detailing the Neogene Shakhdara–Alichur syn-collisional gneiss-dome complex and connection to lithospheric processes. Tectonics, 39(1), e2019TC005735.

Wright, J. E., & Haxel, G. (1982). A garnet-two-mica granite, Coyote Mountains, southern Arizona: Geologic setting, uranium-lead isotopic systematics of zircon, and nature of the granite source region. Geological Society of America Bulletin, 93(11), 1176-1188.

Wu, G., Lavier, L. L., & Choi, E. (2015). Modes of continental extension in a crustal wedge. Earth and Planetary Science Letters, 421, 89-97.

Yin, A. (1989). Origin of regional, rooted low-angle normal faults: A mechanical model and its tectonic implications. Tectonics, 8(3), 469-482.

Yin, A., & DUNN, J. F. (1992). Structural and stratigraphic development of the Whipple-Chemehuevi detachment fault system, southeastern California: Implications for the geometrical evolution of domal and basinal low-angle normal faults. Geological Society of America Bulletin, 104(6), 659-674.

Yin, A., Rumelhart, P. E., Butler, R., Cowgill, E., Harrison, T. M., Foster, D. A., ... & Raza, A. (2002). Tectonic history of the Altyn Tagh fault system in northern Tibet inferred from Cenozoic sedimentation. Geological Society of America Bulletin, 114(10), 1257-1295.

Young, R. A. (1982). Paleogeomorphic evidence for the structural history of the Colorado Plateau margin in western Arizona. In E. G. Frost & D. L. Martin (Eds.), Mesozoic–Cenozoic Tectonic Evolution of the Colorado River Region, California, Arizona, and Nevada (pp. 29–39). San Diego: Cordilleran.

Zeh, A., & Holness, M. B. (2003). The effect of reaction overstep on garnet microtextures in metapelitic rocks of the Ilesha Schist Belt, SW Nigeria. Journal of Petrology, 44(6), 967-994.

Zuza, A. V., Henry, C. D., Dee, S., Thorman, C. H., & Heizler, M. T. (2021). Jurassic–Cenozoic tectonics of the Pequop Mountains, NE Nevada, in the North American Cordillera hinterland. Geosphere, 17(6), 2078-2122.

3 Pore-fluid Pressure Ratio in Whipple Ductile Shear Zone

3.1 Abstract

The brittle-ductile transition zone is as interesting as it is enigmatic. Numerous studies have attempted to understand the deformation mechanisms that control rock behavior at brittle-ductile transition depths, yet there is little known about the pore-fluid pressure ratios at those same depths (Byerlee, 1968; Hobbs et al., 1986; Hacker et al., 1992; Jaoul et al., 1984; Behr and Platt, 2011; Moulas et al., 2019; Lusk et al., 2021; Noël et al., 2021). The Whipple Mountains brittle-ductile shear zone located in southeastern California hosts a suite of rocks that preserve both brittle and ductile processes that are interpreted to have occurred simultaneously. By combining rock mechanics for cataclastic deformation to and dislocation creep flow laws for crystal-plastic deformation, the pore-fluid pressure ratio (λ) at ~20 km depth can be calculated. The results yielded λ values close to 1 where the lithostatic pressure and pore-fluid pressure are almost equal, which may result in fluid flow and quartz-vein formation. Pore-fluid pressure ratios at the brittle-ductile transition zone have not been calculated using values derived from the rocks and are presented here.

3.2 Introduction

Pore-fluid pressure is a key factor controlling the stress state, rock failure and fault reactivation in Earth's crust (Wang et al., 2020). Its role in brittle deformation in the shallow crust (< 1-3 km) has been extensively examined, and in some cases quantified by direct bore-hole measurements; however, how pore-fluid pressure affects crustal deformation at brittle-ductile-transition depths (~15-25 km) remains poorly constrained (Nüchter & Stöckhert, 2008). Deformation that occurred at brittle-ductile transition depths is commonly expressed by the development of semi-brittle shear zones characterized by coeval cataclastic (frictional sliding and fracturing) and crystal-plastic

(dislocation and diffusion creep) deformation (Hirsch and Roberts, 1997). The distinct deformation styles within the same shear zone require stress continuity across the contact between brittle and ductile structures. This stress-continuity condition in turn allows us to use paleobarometry and paleopiezometry to determine the stress state (i.e., the differential stress and mean stress) during semi-brittle deformation. Because the frictional coefficient (~0.6–0.85) and cohesive strength of crystalline rocks (<50 MPa) are well-known from laboratory experiments (i.e., Byerlee's Law), it is possible to use the estimated differential and mean stresses to determine the ratio between pore-fluid pressure and lithostatic pressure for a shear zone characterized by simultaneous cataclastic and crystal-plastic deformation. In this work, I show that such features are characteristic of the Whipple detachment shear zone, which allows estimation of the stress state during shear zone development.

3.2.1 Geologic Background

The domal structure of exhumed rocks in metamorphic core complexes along the North American Cordillera provides insights into the tectonometamorphic history of upper and lower crustal rocks (e.g., Crittenden et al., 1980; Whitney et al., 2013). In the Whipple Mountains metamorphic core complex, the upper crustal rocks include Tertiary metamorphosed sedimentary and volcanic rocks while the basement rocks consist of Proterozoic gneisses and granitoids (Davis, 1988; Gans and Gentry, 2016). The ~3.9 km thick Whipple Mountains brittle-ductile shear zone provides a snapshot of physical processes occurring at depths (Davis, 1980; Davis, 1988). The mylonitic gneisses record metamorphism in their consistently northeast-dipping, foliated and lineated rocks (Davis, 1988). Prograde metamorphic reactions at increasing pressure and temperature may result in dehydration reactions and release fluids into the rocks at depth as

evidence by quartz veins found in metamorphic rocks and high P-T mineral assemblages (Twiss and Moores, 1992; Jaramillo et al., 2024, in press).

Despite extensive studies of fluids, porosity, and rock strength in the brittle upper crust, the role of fluids in the lower crust structures is not well understood. A significant factor influencing rock strength is the presence of fluids in the rocks (Tajčmanová et al., 2014). Veins and hydraulic breccias found in Earth's crust provide evidence of fluid interactions sometimes in the form of microstructures with a characteristic "crack-seal mechanism" (Sachau et al., 2015). The crack-sealing suggests repeated opening and closing of the veins as pressure builds up to open the vein and rock failure releases pressure and to reseal the vein (Hirsch and Roberts, 1997; Ramsay, 1980; Sachau et al., 2015). Studies have attempted to constrain timing of fluid flow during fracturing as well as possible sources of fluids in the lower crust (Nunn, 1996; Sachau et al., 2015).

3.2.2 Governing Equations

3.2.2.1 Background

For a preserved brittle-ductile transition zone, there must be evidence of both brittle and ductile styles of deformation (Figure 3.1). If the Whipple Mountains shear zone displays two different deformation mechanism within the same outcrop we can calculate the stress state. The compressive strength of a rock at shallow depths is a function of the confining pressure, as the confining pressure increase, the strength of the rock also increases (Fredrich et al., 1989; Noël et al., 2021). When the rock reaches the brittle-ductile transition zone, the shear strength of the rock decreases due to shifting deformation mechanisms (Sibson, 1977, 1986; Fossen, 2016; Noël et al., 2021). At this point, deformation is accommodated by ductile deformation (i.e. dislocation and/or diffusion creep) which is a temperature-dependent process (Sibson, 1977, 1986; Noël et al., 2021). Outcrops throughout the Whipple Mountains shear zone highlight both brittle and ductile deformation

occurring at the same place and very likely simultaneously, consistent with Tijoe and Borja (2015) studies that expect both ductile and brittle responses for quasi-brittle materials. Under this assumption, both brittle and ductile deformation share the same state of stress. Thus, we can use the governing equation for each deformation mechanism, set them equal to each other, and calculate the pore-fluid pressure ratio at the brittle-ductile transition zone which has not been done before.

3.2.2.2 Mohr-Coulomb Fracture Criterion

Brittle deformation in the upper crust is characterized by cataclastic deformation (i.e. frictional sliding and fracturing). It is well-known that the strength of brittle rock linearly increases with depth (Fossen, 2016; Noël et al., 2021). How and when fractures occur depends on the strength of the rock and the compressive stresses acting on the rocks (Jaeger and Cook, 1979). The Mohr circle is used to graphically represent the relationship between normal and shear stresses on a plane (Labuz and Zang, 2014; Jaeger and Cook, 1979). To understand how the maximum shear stress relates to cataclastic deformation, we use Byerlee's law:

$$\tau = \mu(\sigma_n - P_f) \tag{1}$$

where τ is the shear stress, μ is the coefficient of static friction with ranging values of 0.6-0.85, σ_n is the normal stress, and P_f is the pore fluid pressure (Byerlee, 1978, Seno, 2009). Byerlee's law, which assumes no cohesion, can be rewritten to satisfy the Mohr-Coulomb fracture criterion (Shen et al., 2012):

$$|\tau_n| = S + \bar{\mu}_\varphi(1 - \lambda)\sigma_n \tag{2}$$

where $|\tau_n|$ is the critical shear stress causing new fractures, S is the cohesive strength of the intact rock, $\bar{\mu}_\varphi$ is the coefficient of internal friction, $\bar{\varphi}$ is the angle of internal friction, σ_n is the normal stress on a newly created fracture plane, and λ is the pore-fluid pressure ratio.

Additionally, $\bar{\varphi}(\lambda) = arctan\,[\bar{\mu}_\varphi\,(1-\lambda)]$ is the angle of the linear envelope of failure that the horizontal principal stress axis makes with the plane of failure (Figure 3.2). Thus, $\tan[\bar{\varphi}(\lambda)] = \bar{\mu}_\varphi(1-\lambda)$ is the slope of the line. It is common to assume a "two-dimensional mean stress", σ_m, to determine when a rock will fracture or fail (Jaeger et. al., 2009). For example, if the principal stresses acting on the system form a Mohr's circle that falls below the failure envelope, the rock will not fracture or fail along any plane (Jaeger et. al., 2009). Once the stresses form a Mohr's circle that intersects the failure envelope, the rock will shear along a new fracture plane (Jaeger et. al., 2009).

The mean stress and maximum shear stress may be expressed as $\sigma_m = \frac{1}{2}(\sigma_1 + \sigma_3)$ and $\tau_{max} = \frac{1}{2}(\sigma_1 - \sigma_3)$, respectively. Thus, the Mohr Coulomb failure criterion can be rewritten in terms of maximum shear and mean stress, which are functions of the angle of internal friction:

$$\tau_{max} = \sigma_m \sin\overline{\varphi}\,(\lambda) + Sco\,s\big(\overline{\varphi}\;(\lambda)\big) \tag{3}$$

where τ_{max} is the maximum shear stress, S is the cohesive strength of the rock, $\overline{\varphi}$ is the effective angle of internal friction, σ_m is the mean stress, λ, is the pore-fluid pressure ratio. The symbol $\bar{\varphi}(\lambda)$ as a function of lambda represents the slope angle of the linear envelope of failure.

3.2.3 Dislocation Creep

Crystal-plastic (i.e. ductile) flow is the main deformation mechanism at high confining pressures in the middle and lower crust (Byerlee, 1968; Tijoe and Borja, 2015). Ductile deformation is governed by processes such as dislocation and/or diffusion creep (Schueller and Davy, 2008; Warren and Hansen, 2023). Deformation occurring in the mid- to lower crust is a temperature-dependent process and thus we can use constitutive relations to infer insights about how temperature affects other physical properties of the deformed material (Schueller and Davy, 2008; Warren and Hansen, 2023). Specifically, due to the high abundance of quartz-rich rocks and the governing role that quartz plays in rock deformation in the crust, the properties of quartzites have been used constrain geodynamic and rheologic parameters in the crust (Hirth et al. 2001; Lusk et al. 2021). For example, Hobbs et al. (1986) analyzed how deep the seismogenic zone extends based on what they refer to as ductile instabilities in rocks at specific temperatures, Kohlstedt and Weathers (1980) studied crustal strength up to 200 MPa, and experimental studies using quartzite flow laws have provided constraints on rheological properties in the crust (Dresen et al. 1997; Stipp et al., 2002; Stipp and Kunze, 2008; Stöckhert et al. 1999). The flow law used to analyze rheological properties of quartzite is given as:

$$\dot{\varepsilon} = A f_{H_2O}^{m} \, \sigma_{\text{diff}}{}^{n} exp(-Q/RT) \qquad (4)$$

where $\dot{\varepsilon}$ is the strain rate, A is a material constant, f_{H_2O} is the fugacity of water, σ_{diff} is the differential stress, m and n are material constants related to fugacity and differential stress, respectively, Q is the activation energy, R is the universal gas constant, and T is the temperature (Hirth et al. 2001). When combined with microstructural observations, laboratory experiments and petrological data, the flow laws provide useful constraints on rheologic parameters deep in the crust (Hirth et al. 2001).

3.3 Methods

The two governing equations are the Mohr-Coulomb fracture criterion for cataclastic deformation (Eq. 3) and the dislocation-creep flow law for crystal-plastic deformation (Eq. 4). Under the assumption that the shear zone contains evidence of both deformation mechanisms operating simultaneously – i.e., under the same stress state – the two equations can be solved simultaneously. Given adequate constraints on the other variables, the pore-fluid pressure ratio can be obtained.

Apparent brittle normal faults in mafic rocks terminating into coeval felsic mylonitic foliations or into mini detachments are long known in the Cordilleran core complexes and are commonly referred to as "ductile normal faults" (Davis, 1980; Davis et al., 1980). Because the *P*-*T* path at each sample site can be acquired in our work, the temperature of a syn-brittle-faulting mylonitic quartz-vein, T_{qtz}, must correspond to a pressure, P_{qtz}. The value of P_{qtz} is the same as the lithostatic pressure P_{lith}, which is related to the maximum brittle shear stress for faulting, τ_{max}, (Jaeger et al., 2009). This allows Eq. (3) to be rewritten as:

$$\tau_{max} = P_{lith} \sin\bar{\varphi} + S0 \cos\bar{\varphi} \quad (5)$$

where S_0 = ~50 MPa is the cohesive strength, $\bar{\mu} = tan\ \bar{\varphi} = \mu(1 - \lambda)$ is the effective coefficient of friction, μ = ~0.6 is the coefficient of friction, $\lambda = P_f / P_{lith}$ is the pore-fluid-pressure ratio, and P_f is the pore-fluid pressure (Byerlee, 1978). Stress continuity (e.g., Kohlstedt et al., 1995) requires that the maximum ductile-creep shear stress (τ_d) equals the maximum brittle shear stress (τ_{max}), which gives,

$$\tau_d = \tau_{max} = P_{qtz} \sin\bar{\varphi}(\lambda) + 50(\mathrm{MPa})\cos\bar{\varphi}(\lambda) \quad (6)$$

where $\bar{\varphi}(\lambda) = arctan\,[\mu(1-\lambda)]$. The above relationship shows that given τ_d and P_{qtz} obtained from coupled paleobarometry and paleopiezometry, we can determine λ value. When $\lambda > 1.0$, the pore-fluid pressure (P_f) locally exceeds the lithostatic pressure ($P_{lith} = P_{qtz}$). Also note that ($P_{lith} - P_f$) $>T_0$, where T_0 is the rock tensile strength (~5 MPa) (see Jaeger et al., 2009), leads to hydraulic fracturing. Walther and Orville (1982) calculated the volume of volatiles produced during metamorphism and determined that fluid escape in pelitic rocks results in quartz vein formation due to localized pressure gradients. During metamorphism, while neglecting non-uniform lithostatic pressure, the pore-fluid pressure and lithostatic pressure will be close, or almost equal, to each other (Walther and Orville, 1992). As the fluid pressure exceeds the rock pressure, a pressure gradient in excess of the local hydrostatic gradient causes upward fluid flow which results in quartz veins (Walther and Orville, 1982). The presence of multiple sets of brittle faults terminating at multiple sets of mylonitic quartz veins in the Whipple mylonitic shear zone would allow us to convert P_{qtz} (x,y,t) and τ_d (x,y,t) data to λ (x,y,t) data in a vertical section.

The P-T-τ_d data to be collected will also allow us to determine the strain rate $\dot{\varepsilon}$ during mylonitization using the Hirth et al. (2001) quartz flow law Eq. (4). Given $logA$ =−11.2MPa-n/s, Q=135kJ/mol, m=1, n= 4, and $f_{H_2O}^m$ is the water fugacity that is a function of P and T (in Kelvin) (Sterner and Pitzer, 1994) under which the stress magnitude is recorded, $\sigma = 2\ \tau_d$ is the differential ductile-creep stress, and R. Because P, T, and τ_d all vary with time and space, the estimated strain rate from Eq. (4) will also vary with time and space. Behr and Platt (2014) took a similar approach to estimate strain rates by converting paired T-τ_d data to the corresponding paired P-τ_d data assuming a constant geothermal gradient in a single shear zone. The advective effect of detachment-fault footwall deformation (e.g., Lavier and Manatschal, 2006) would create a

complex thermal structure that cannot be captured by a single constant geothermal gradient across the entire shear zone as assumed in Behr and Platt (2014).

Oriented samples collected across the Whipple Mountains shear zone were used to collect microstructural observational analysis as well as electron backscattered diffraction (EBSD) data. Recrystallized and relict grains are differentiated following Cross et al. (2017) using EBSD-determined grain orientation spreads (GOS). Final stress-magnitude estimates will consider the effect of post-kinematic annealing (Hacker et al., 1991) and coeval cooling and dynamic recrystallization (Soleymani et al., 2020).

EBSD analyses were conducted to obtain high-resolution phase maps, sense of shear, crystallographic preferred orientations (CPOs), mineral orientations related to dominant slip mechanisms, and grain-size (e.g., Zuza et al. 2022; Chapman et al., 2010; Cross et al., 2017; Kruhl and Vernon, 2005). Polished thin sections were vibrationally polished for ~8 h with 0.02 μm colloidal silica suspension to remove near-surface crystal lattice imperfections (Zuza et al., 2022). EBSD mapping included collection of EBSD patterns from each section of a defined orthogonal grid using a Nordlys Nano high-resolution detector (Zuza et al., 2022). The Oxford Instruments Aztec 3.3 acquisition software package on a JEOL 7100 field emission Scanning Electron Microscope (SEM) was also used in the data collection process (Zuza et al., 2022). Step size during mapping varied slightly depending on the individual sample's grain size but remained significantly lower than the recrystallized grain size to ensure grain-size analysis was consistent with the Cross et al., (2017) piezometer. Estimated grain-size data based on an internal misorientation-of-grains threshold differentiates recrystallized grains from relict grains (Zuza et al., 2022). Since quartz grains from target areas appear recrystallized, we can use the root mean square (RMS) of all quartz data with the Cross et al. (2017) quartz piezometer. Data were analyzed using MTEX 5.2.1

(Bachmann et al., 2010) in MATLAB. EBSD data were collected at the Mackay Microbeam Laboratory at the University of Nevada, Reno.

3.4 Results

The Whipple Mountains ductile shear zone consists of amphibolites, quartzofeldspathic gneisses, gabbro blocks, and garnet-bearing schists that encompass large parts below the Whipple detachment (Figure 3.3A-E). The characteristic gneissic banding highlights areas of both brittle and ductile deformation. Fig. 3.3B provides an example of boudinaged gabbro blocks (above the rock hammer) that appear to be brittlely deforming within the broader, ductilely deforming amphibolite and quartz-rich units. Figure 3.3.C highlights areas where the felsic rocks appear to be brittlely deforming along small faults within the mafic unit. Figure 3.4 highlights the observed structures in outcrops throughout the Whipple Mountains shear zone; apparent brittle faults are highlighted in red lines and form at ~45-degree angles. Pure quartz veins are present both in the quartzite layers and in the amphibolite or gneiss layers both parallel and non-parallel to foliation. Figure 3.5 (A) shows a typical outcrop cross section where the quartz-rich layers (lighter color material) are cut by brittle faults while synchronously being deformed by apparent ductile deformation within the same 2x3 m outcrop.

The Mohr-Coulomb fracture criterion Eq. (6) is used to represent brittle deformation in the Whipple Mountains brittle-ductile shear zone. The cohesive strength of the rock, S, and the effective angle of internal friction, $\bar{\varphi}$, are known from extensive laboratory experiments (Byerlee, 1978). To calculate the pore-fluid pressure ratio (λ), we must determine the values for the other unknown variables (e.g., τ_{max}, σ_m) in the Mohr-Coulomb fracture criterion equation.

The presence of faults that accommodated brittle deformation formed between the maximum compressive stress, σ_1, (i.e. the vertical lithostatic pressure) and the least compressive

stress direction, σ_3, (i.e. the horizontal foliation direction), which produced a fault plane at approximately $\theta = 45°$, relative to both stresses. The angle, θ, that the normal to the fault plane makes with the vertical direction, σ_1, in physical space is half of that in Mohr's circle space (Figure 3.2). In continuum mechanics and metamorphic recrystallization calculations, the mean stress (σ_m) may be used to estimate the hydrostatic pressure or thermodynamic pressure (*P*) (Moulas et al, 2019). Since we assume the stress at a single point was constant and that both brittle and ductile deformation mechanisms operated simultaneously at this point, we can relate variables from both Eq. (4) and (6) to constrain the values of unknown variables. The quartz dislocation-creep flow law that we use for our samples has its own set of known variables and material constants (i.e., A, m, n, Q, and R) (Gleason and Tullis, 1995) and unknowns (i.e., $\dot{\varepsilon}$, σ_{diff}, P_{TD}, *T*, and f_{H_2O}) for our specific sample conditions.

Using thermobarometry is the first step to finding the unknowns in the dislocation creep flow law equation and determining the *P-T* conditions of the rocks in the Whipple Mountains brittle-ductile shear zone (see Chapter 2, Methods). The *P-T* conditions estimated via garnet-plagioclase-biotite-muscovite (GPBM) barometry (Hoisch, 1990) and garnet-biotite (GB) thermometry (Ferry & Spear, 1978; Berman, 1990) resulted in thermodynamic pressures, P_{TD}, of 0.7-0.9 GPa (garnet rim and matrix mineral assemblage) and 0.6-0.8 GPa (garnet core) and temperatures, *T,* of 680-750°C (rim) and 750-800°C (core).

To explore the feasibility of a paleo-piezometry study, we obtained a "mis2mean" map (i.e., misorientation with respect to the grain's mean orientation) from a mylonitic quartz vein (Fig. 3.6, 3.7), which differentiates recrystallized grains (blue) from relic grains (red) (Cross et al., 2017). Using EBSD-based quartz recrystallized grain size paleopiezometry (Cross et al., 2017) we determined that the mean recrystallized grain size averaged ~38 microns for our samples (Figure

3.8). The recrystallized mean grain size is plotted against differential stress (Figure 3.9) in which using the sliding piezometer yields a differential stress, σ_{diff} ~ 40 MPa (Cross et al., 2017; Stipp and Tullis 2003). The last unknown variable of the quartz dislocation creep flow law is the strain rate, calculated to have a magnitude of $\dot{\varepsilon} \sim 10^{-12}$ s^{-1}.

Having constrained values for the unknowns in the quartz dislocation creep flow law, we can use the equivalent values in the Mohr-Coulomb fracture criterion equation to calculate the pore-fluid pressure ratios. In this model (Figure 3.10), we plot equation (1) to illustrate the relationship between ductile shear stress and pore-fluid pressure ratios. Data from Hacker et al. (1992) and Behr and Platt (2011) are shown to compare estimates from previous work and how they intercept the lower and upper pressure estimates with respect to the shear stress and pore-fluid pressure ratio. Half of the calculated differential stress of ~40 MPa for the Whipple samples are equivalent to shear stresses of τ_{max} = 20 MPa, which falls within the estimated pore-fluid pressure ratio range λ = 0.89-1.07.

3.5 Discussion

Outcrop observations throughout the Whipple Mountains shear zone support the "crack-seal" method (Ramsay, 1980), through evidence of opening and closing of veins within the quartzofeldspathic rocks. What is meant by the opening and closing of veins is the continuous change in local pore pressure that contributes to fluid flow which is consistent with the idea that the quartz veins in the Whipple Mountains shear zone are accommodating the deformation (Walther and Orville, 1982). Furthermore, quartz veins found throughout the shear zone highlight areas where both brittle and ductile deformation are assumed to have been occurring contemporaneously. This approach combined rock mechanics and flow laws to calculate the pore-fluid pressure ratios of λ = 0.89-1.07, where λ values close to 1 suggest that the pore-fluid pressure

is near the lithostatic pressure at the brittle-ductile transition zone thus making it possible for quartz vein formation.

For this study and to highlight the feasibility of obtaining a constraint on pore-fluid pressure values an EBSD-calibrated (Cross et al., 2017) dynamically recrystallized quartz-grainsize piezometers of Stipp and Tullis (2003) and Stipp et al. (2006) was used. Figure 3.8 illustrates the distribution of grain sizes and the relative frequency of grains sizes in sample VJ-02-19-22-4B, where blue represents recrystallized grains and red represents relict grains. The mean grain size used in Figure 3.9 represents the mean average recrystallized grain size, which changes slightly per sample, but provides a starting point for the calculations. From the Cross et al. (2017) calibration, using a "sliding" piezometer allows for a better representation of grain density and mean grain size. If the mean grain size was <10 μm a 1-μm calibration may not capture all recrystallized grains and would overestimate a mean grain size (Cross et al., 2017). On the other hand, a 200-nm calibration is useful in samples where mean recrystallized grain size <10 μm, but requires more time and more grains to be analyzed (Cross et al., 2017). While both calibrations target specific characteristics of the sample, there is only a 10% difference if recrystallized mean grain size is 10-100 μm (Cross et al. (2017), which is the range for the Whipple Mountains shear zone samples.

To highlight the ranges in values in the calculations, shear stresses were plotted against pore-fluid pressure ratio values while varying *P*, S, and μ (Figure 3.11). To constrain between the maximum shear stress previously reported (i.e., tan line at 68 MPa), (Behr and Platt, 2011) and the maximum shear stress in this study (i.e., grey line at 20 MPa), the horizontal lines were plotted. Note that half of the differential stress from the calibrations is the maximum shear stress plotted. The shallow-dipping curves represent conditions at ~9 km-depth or 250 MPa (Axen, 2020; Behr

and Platt, 2011) with varying cohesion values (i.e.,10 MPa, green; 50 MPa, purple). At higher stress conditions and shallower depths where the green and purple lines intersect the tan line, lambda values range from 0.6 – 0.9. The steep curves represent the calculated thermodynamic pressure (P = 750 MPa, Jaramillo et al., 2024, in press) with cohesion values of 10 MPa (blue curve) and 50 MPa (orange curve). At deeper, lower stress conditions, the lambda values are ~0.9 – 1.1, where the blue and orange lines intersect the grey line. Not plotted are a curve with cohesion of 10 MPa, pressure of 250 MPa, and μ=0.3 that yielded lambda values between 0.5 – 0.9 and a curve with cohesion of 50 MPa, pressure of 800 MPa, and μ=0.8 that yielded lambda values of 0.95 – 1.05 as they intersect the horizontal lines. Even at the lowest stress conditions, λ values do not fall below 0.5 and thus suggest overpressurization. An interpretation for the deeper, hotter, lower stress conditions may be that they represent older prograde metamorphism deformation, whereas shallower, colder, and higher stress conditions may represent younger exhumation-related deformation.

The method of simultaneously determining creep-stress magnitude and temperature was pioneered by Behr and Platt (2011), with important implications for inferring the strength profile of the continental lithosphere (Behr and Platt, 2014). Note that Behr and Platt (2014) took a similar approach to estimate strain rates by converting paired T-τ data to the corresponding paired P-τ data assuming a constant geothermal gradient in a single shear zone. The advective effect of detachment-fault footwall deformation (e.g., Lavier and Manatschal, 2006) would create a complex thermal structure that cannot be captured by a single constant geothermal gradient across the entire shear zone as assumed in Behr and Platt (2014). Our EBSD data are shown in Fig. 3.7, where the quartz CPO pole figures and topologies are consistent with the intermedia-temperature deformation regime of Hirth and Tullis (1992). The pole figures are similar to those obtained by

Behr and Platt (2011) from the Whipple mylonitic shear zone. Tullis et al. (1979) demonstrated that quartzite yield strength decreases after reaching temperatures of ~750°C which is at the cusp of *P-T* estimates for the brittle-ductile shear zone of the Whipple Mountains shear zone (Jaramillo et al., 2024, in press).

Furthermore, the strain rate estimates are consistent with dynamic recrystallization of quartz via dislocation creep occurring in granulite conditions in rocks from the eastern Nusfjord region in Lofoten, Norway (Campbell and Menegon, 2019). Given the high temperature and the calculated shear stress in the mylonitic ductile shear zone, it is important to consider the potential for anatexis under these conditions (Harrison et al., 1998). Numerical simulations conducted by Harrison et al. (1998) determined that shear heating of pelitic rocks may be linked to partial melting in an active thrust system; a minimum shear stress of 10 MPa caused 4% melt. Keeping this in mind, the observed partial melt relationships within the Whipple ductile shear zone may be evidence of shear heating as suggested by previous models. Regardless, the calculation of pore-fluid pressure ratios provides insights into the role of fluids at depths. The approach has the potential for wide use in metamorphic core complexes worldwide.

3.6 Conclusions

The proposed method of calculating pore-fluid pressure ratios at the brittle-ductile transition zone yielded λ = 0.89-1.07, consistent with quartz-vein formation at high pore-fluid pressures throughout the Whipple Mountains brittle-ductile shear zone. This research supports efforts to understand the permeability of rocks (Patterson & Wong, 2005; Yin, 2018) at the brittle-ductile transition zone and overall tectonometamorphic evolution of the middle-lower crustal rocks. Strain rates are consistent with high *P-T* conditions and depths of ~20 km (Campbell and Menegon, 2019). The values calculated at each step contain uncertainties and ranges that add to the

uncertainty of the results and running Monte Carlo simulations may enhance the results. However, method may be used across metamorphic core complexes and provide insights into the evolution of the North American Cordillera Anatectic Belt at depths not previously studied. Future work is necessary to determine whether melting occurred during Cenozoic extension, Mesozoic mylonitization, or other Precambrian events.

3.7 Figures

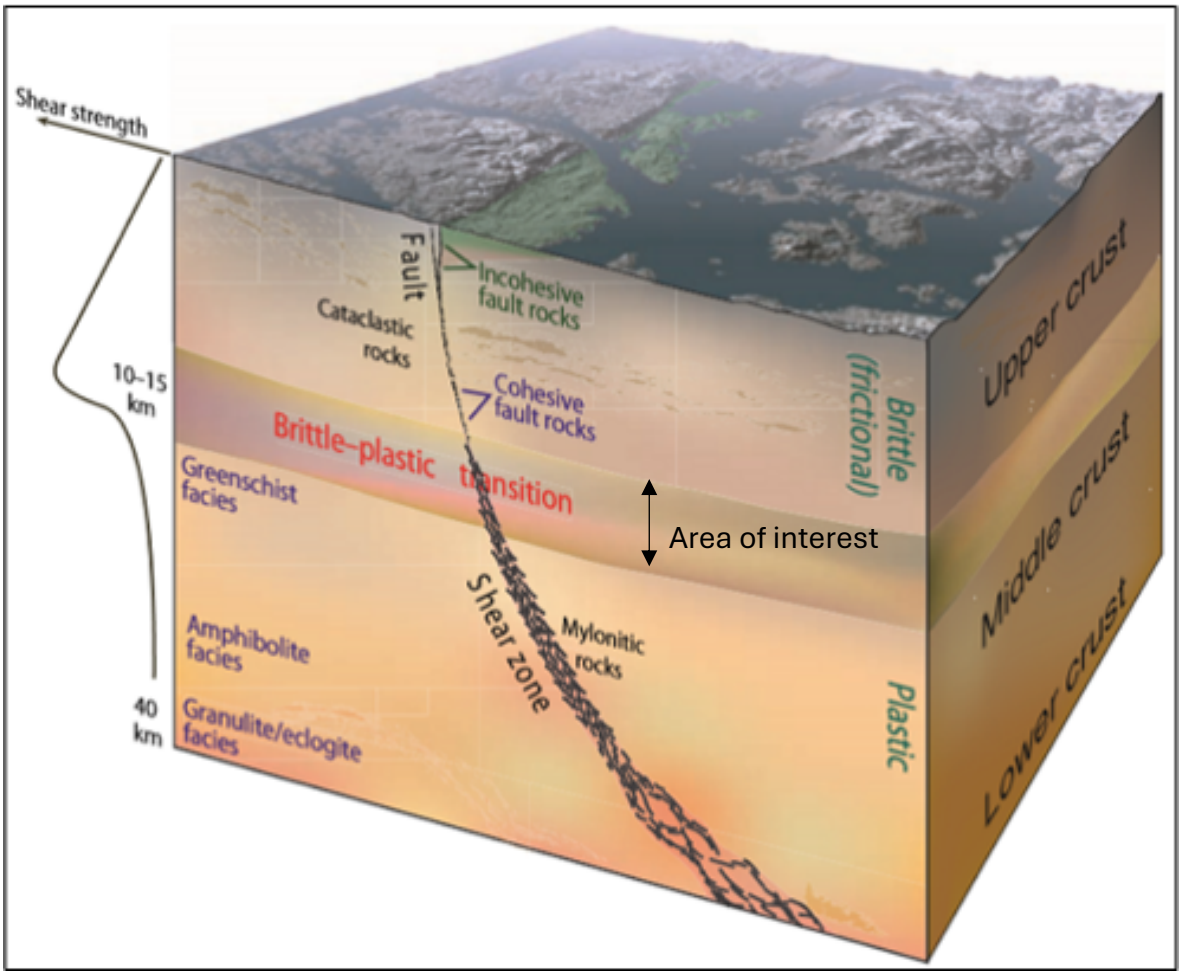

Figure 3.1. Model interpretation of the different deformation regimes at various depth estimates in the crust. Shear strength profile highlights linear increase in strength with depth until the brittle-plastic transition zone (10-15 km depth) (Modified from Fossen, 2016).

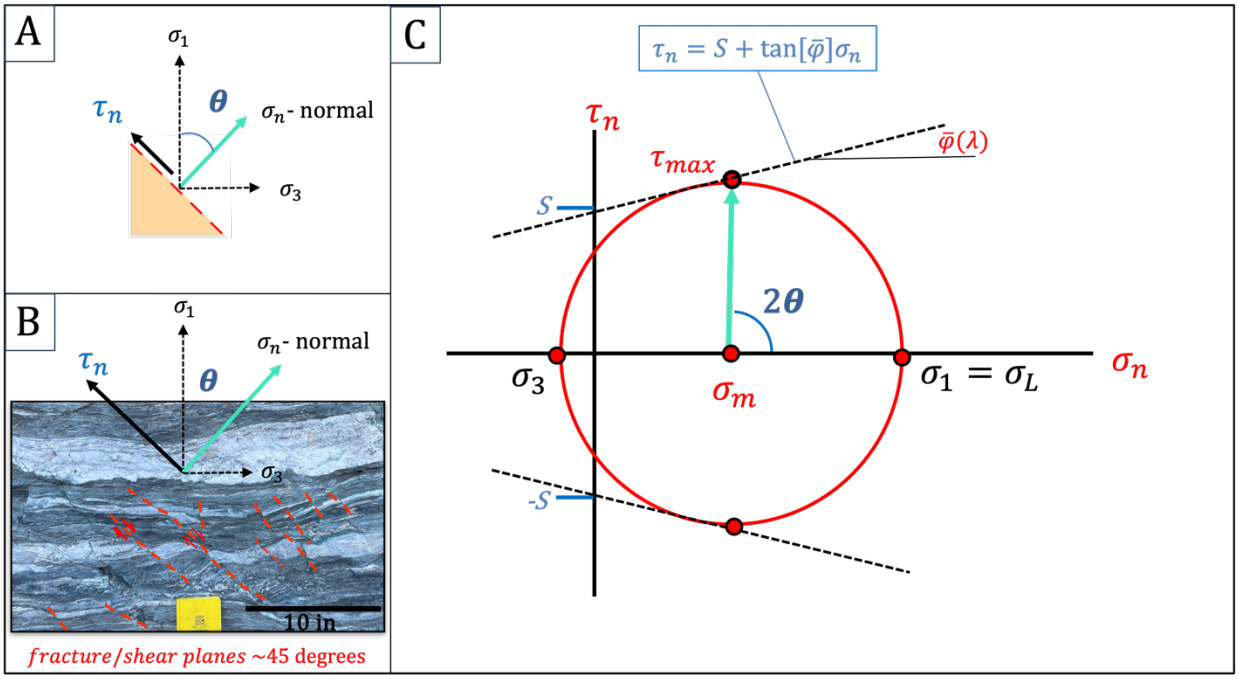

Figure 3.2. (A) Diagram of a fracture or shear plane, τ_n, with a vertical, principal compressive stress, $\sigma_1 = \sigma_L$, a minimum compressive stress, σ_3, the normal to the fracture plane, σ_n, and θ which is the angle that the principal stress makes with the normal to the plane. (B). Outcrop photo of foliated gneiss unit with observed brittle-ductile behavior present where faults are accommodating brittle deformation in the more felsic layers and those faults taper into the ductile fabrics. The angles that the faults planes make with respect to the foliation direction and the vertical lithostatic pressure are approximately 45°. (C) Mohr's circle representing the shear (τ_n) and normal stresses (σ_n). S—cohesive strength of the rock; τ_{max}—maximum shear strength. $\bar{\varphi}(\lambda)$ – slope angle of the linear envelope of failure.

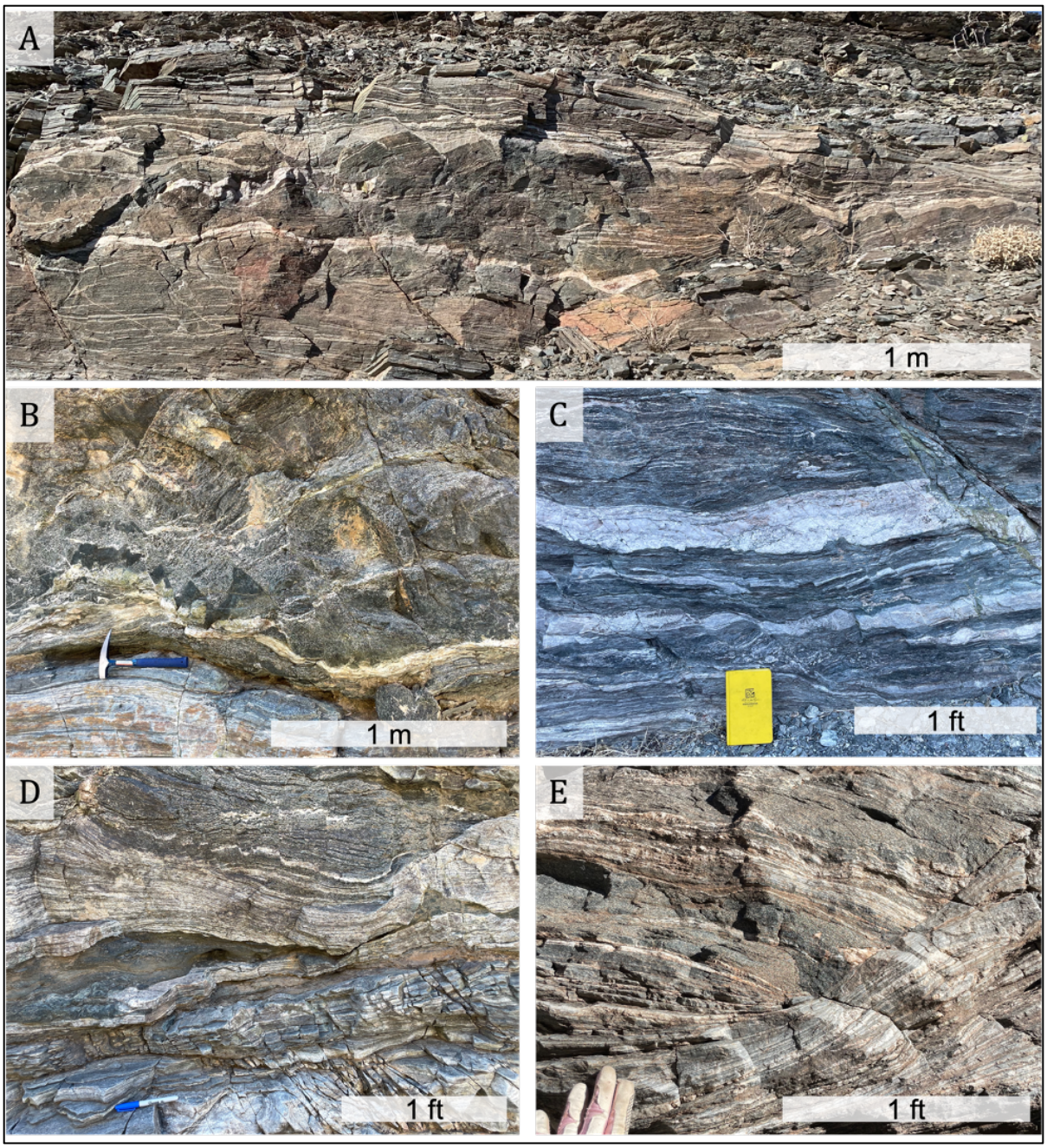

Figure 3.3. (A) Outcrop photo within the Whipple Mountains shear zone highlighting brittle-ductile deformation of a quartz-rich layer within the mafic unit. (B) Boudinaged gabbro block bounded by sharp, brittle faulting (above rock hammer). (C). Foliated, quartzofeldspathic gneisses with lighter-colored, felsic layers appear to be brittely deformed along faults within the gneisses and the faults terminate in the more ductile layers below. The fault located in the top-right corner appears distinctly younger and filled with epidote veins. (D) Interlayered amphibolite, gneiss, and quartz-rich layers including an elongated gabbro block. Light-colored thick unit at the center appears to wrap around mafic gabbro block (above Sharpie marker). (E) Interlayered amphibolite and quartzite layers tilted in a top-right sense of motion along the mini detachment above the glove.

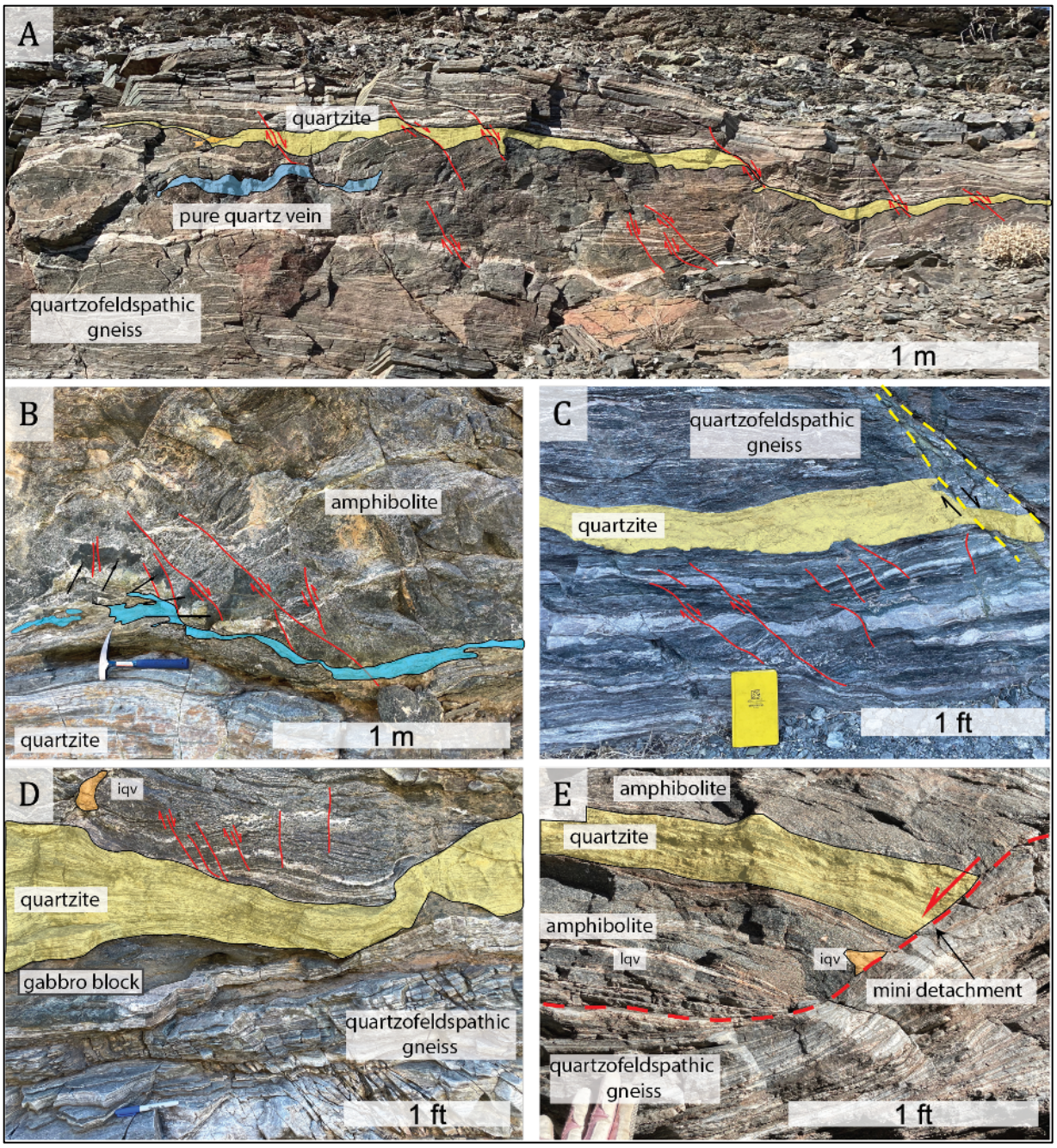

Figure 3.4. Same as Figure 3.3, where yellow polygons (A,C,D,E) highlight the quartzite layers that appear to be deforming ductilely. Brittle faults (A,B,C,D) are annotated in red with the exception of (E) that represents a mini detachment. Blue polygons represent some of the pure-quartz veins (lqv) that are parallel to foliation. Light orange polygons (A, D, E) represent irregular quartz veins (iqv) not parallel to foliation.

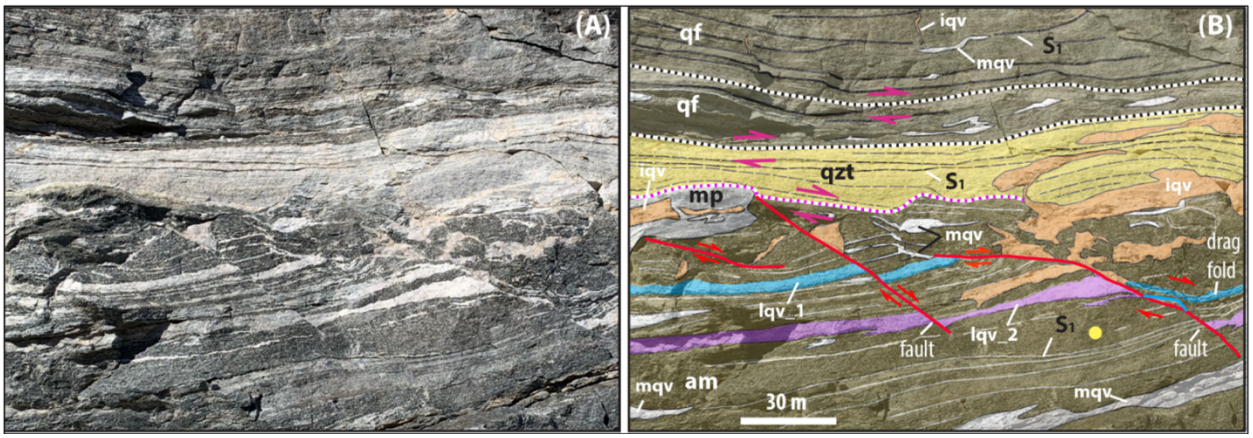

Figure 3.5. A typical outcrop of the 3.9 km thick Whipple mylonitic shear zone (A) and the corresponding geology (B) Interpretation of the brittle faults cutting across the amphibolite layer unit either terminate at sheared quartz veins (mvq) or at contacts between the amphibolite (am) and quartzite/quartzofeldspathic (qf) layers. Drag folds next to the brittle faults suggest coeval brittle and ductile deformation, consistent with the faults terminating at ductile shear planes. Lithologic units: qf, quartzofelspathic gneiss; qtz, quartzite; mp, two-mica garnet-bearing meta-pelite; am, amphibolite; mqv, mylonitic quartz vein; iqv, irregularly shaped quartz veins; lqv, foliation-parallel layered quartz veins.

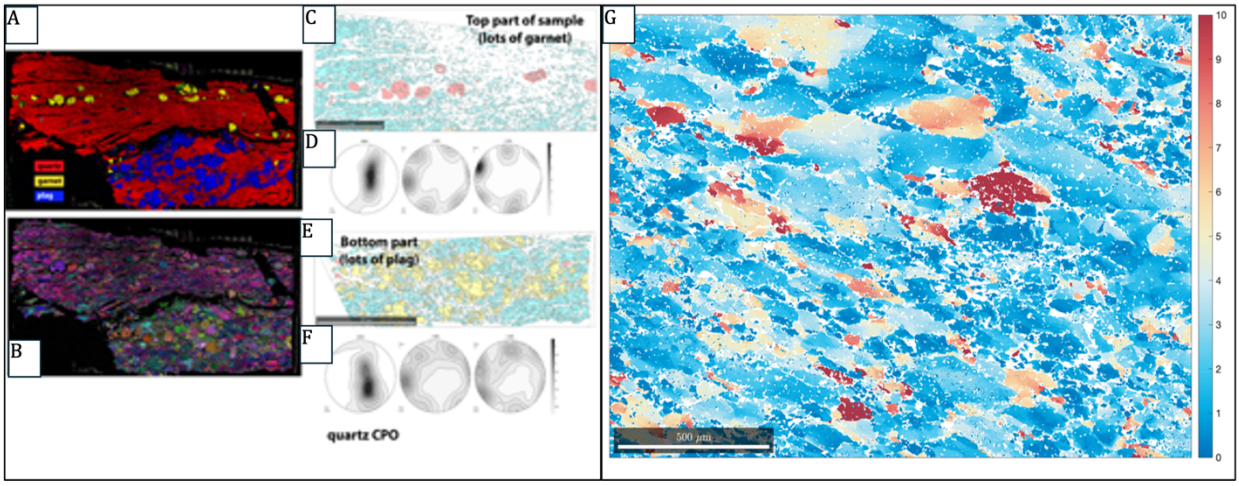

Figure 3.6. **. (A)** EBSD phase map (27x46 mm thin section) of a meta-pelite sample with a step size of 6 μm cut parallel to lineation and perpendicular to foliation**. (B)** is an All Euler angle map for the same meta-pelite sample showing the distribution of crystallographic preferred orientations in the phases of the sample. Different colors represent different crystal orientations. **(C)** Top part of the thin section containing abundant garnet porphyroclasts with corresponding quartz CPO plotted in pole figures in **(D). (E)** The bottom part of the thin section containing abundant plagioclase showing corresponding quartz CPO in pole figures in **(F)**. The quartz CPO pole figures plot the quartz c-axis and a-axis. The topology of these pole figures is consistent with medium temperature (~600 C) deformation conditions. **(G)** A "mis2mean" map (misorientation with respect to the grain's mean orientation) of quartz from a mylonitic quartz vein sample. The large grains with high mis2mean values (red and orange) represent relict porphyroclasts and the smaller grains with low mis2mean values (blue) represent recrystallized grains. EBSD analysis courtesy of Emily J. Chin.

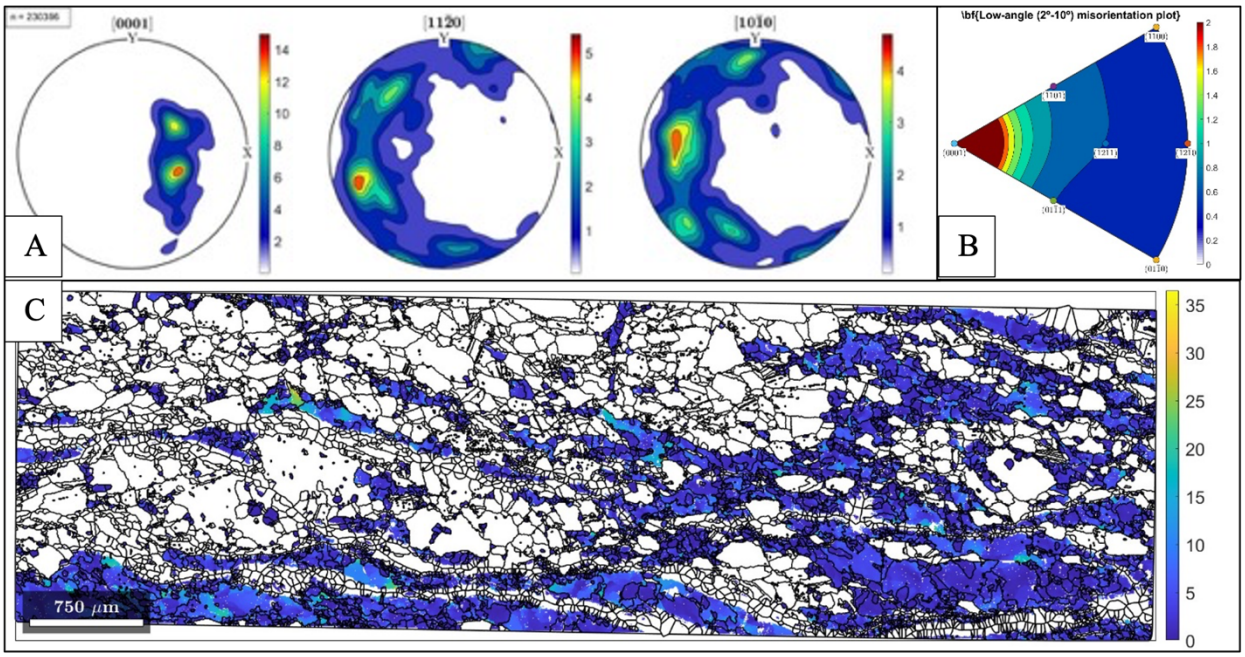

Figure 3.7. (A). Crystallographic preferred orientation (CPO) pole figures for quartz grains in EBSD-mapped sample VJ-02-19-22-4B. **(B).** Low-angle (2-10°) misorientation plot for sample VJ-02-19-22-4B. **(C).** A "mis2mean" map (misorientation with respect to the grain's mean orientation) of quartz from a mylonitic quartz vein sample. The large grains with high mis2mean values (red and orange) represent relict grains and the smaller grains with low mis2mean values (blue) represent recrystallized grains.

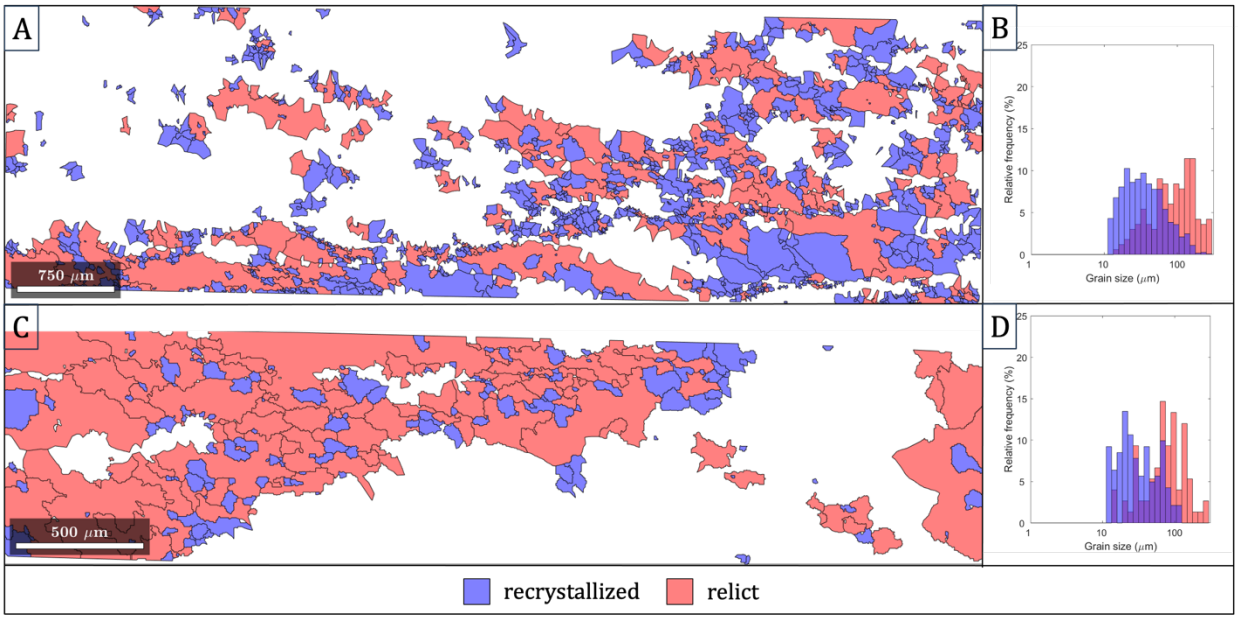

Figure 3.8. Log_{10} grain size distributions for 2 example data sets. Figures 3A and 3C are the grain size distributions for the entire grain population, which are separated into relict and recrystallized grain size distributions in Figures 3B and 3D. Relative frequencies (Figures 3B and 3D) are calculated with respect to the number of grains in each subpopulation, to "amplify" the relict grain histograms (red). Recrystallized grain sizes in blue.

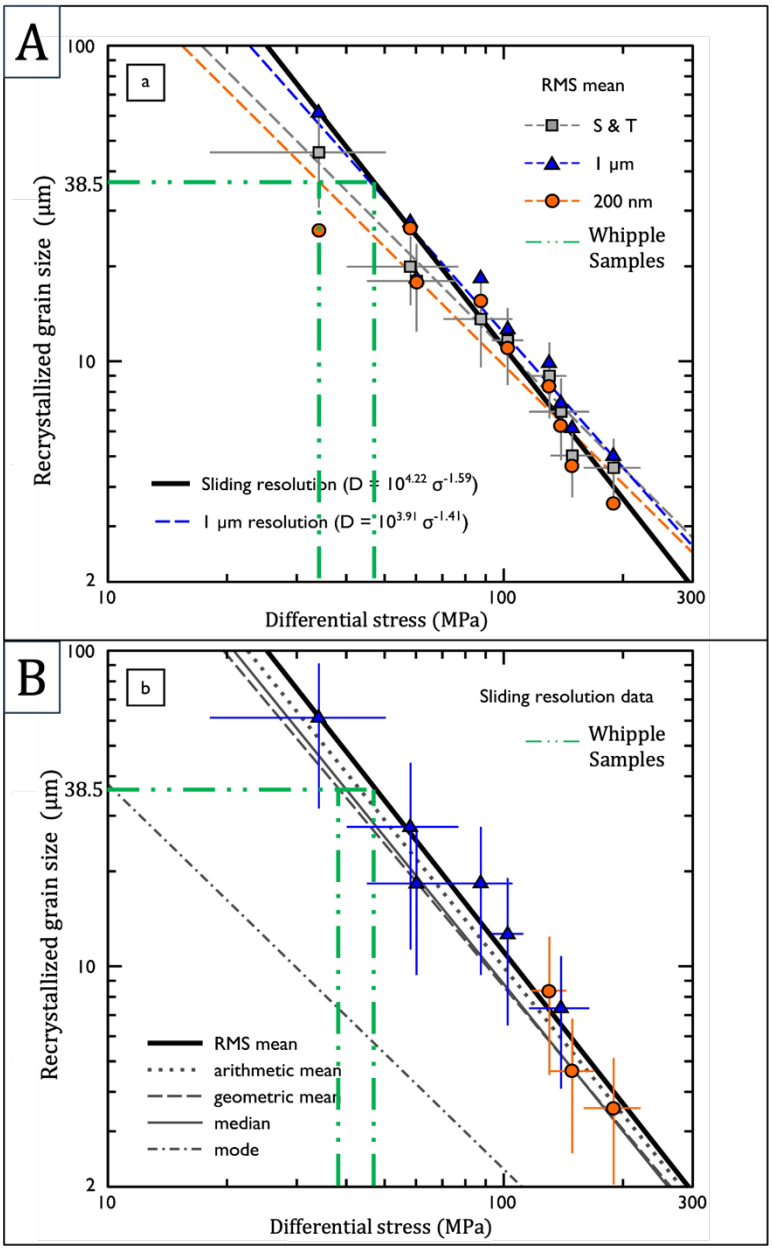

Figure 3.9. Quartz EBSD recrystallized grain size piezometer modified from Cross et al. (2017) to include Whipple sample data. The double-dotted line represents an average recrystallized grain size of 38.5 microns that results in differential stresses in the range of 35-48 MPa in both the Root Mean Square (RMS) piezometer **(A)** or the sliding resolution piezometer **(B)**.

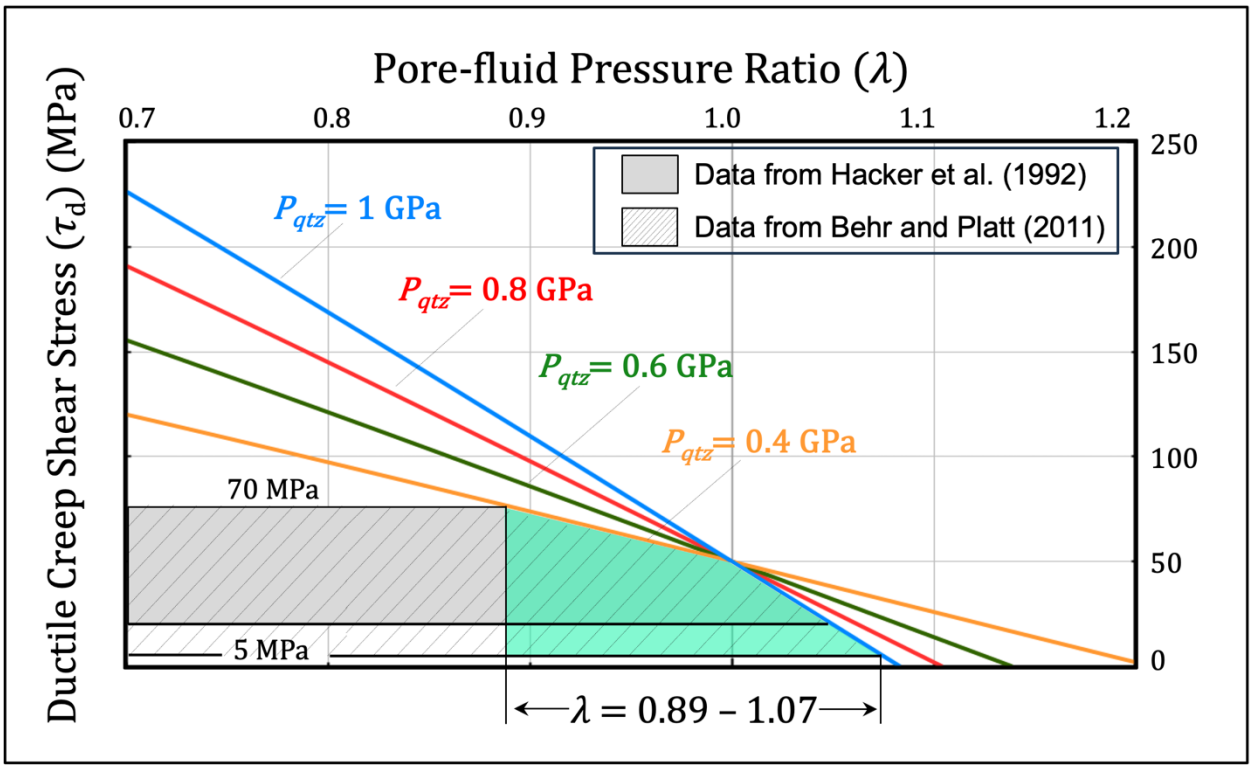

Figure 3.10. Relationship between ductile creep stress and pore-fluid pressure ratio with variable lithostatic pressures. Data from Hacker et al. (1992) and Behr and Platt (2011) are plotted to show previous shear stress estimates for the Whipple Mountains shear zone.

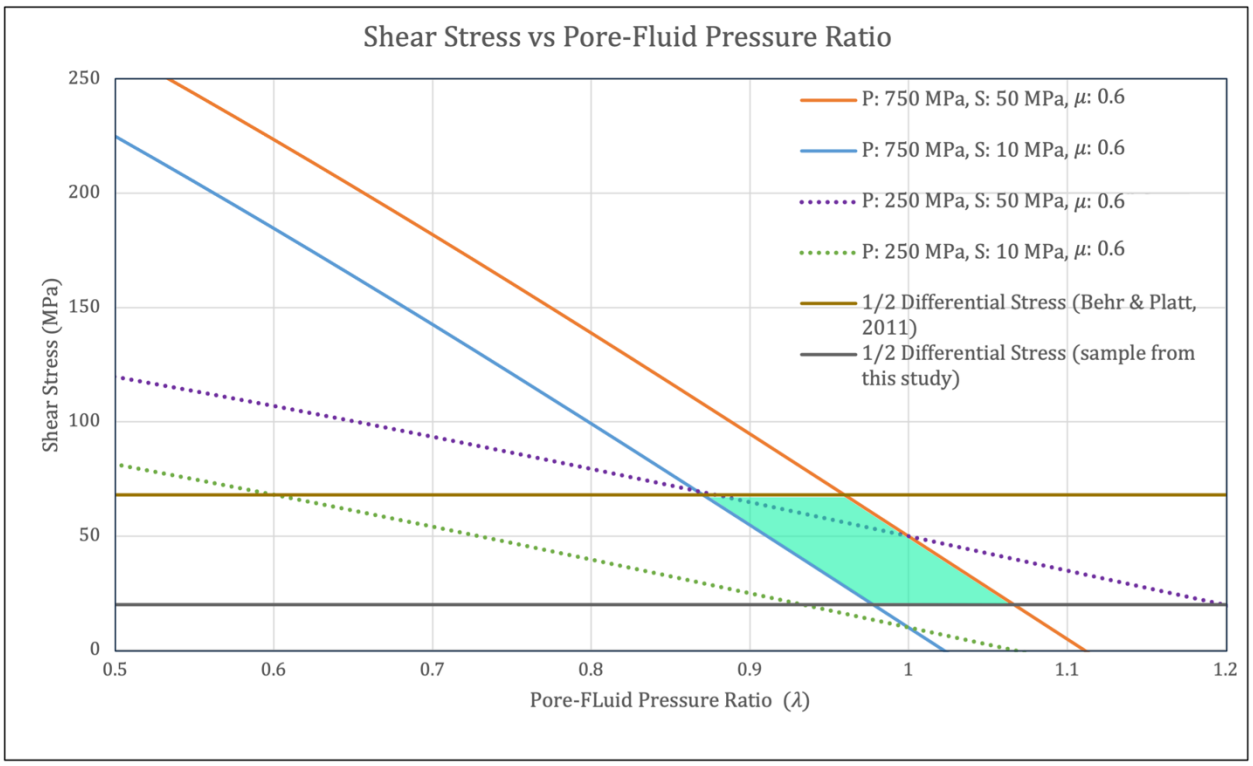

Figure 3.11. Relationship between max shear stress and pore-fluid pressure ratios. Data from Behr and Platt (2011) (tan horizontal line) are plotted to show previous max shear stress estimates for the Whipple Mountains shear zone (halved to represent the differential stress – 68 MPa). Max shear stress from this study ~19.5 MPa (dark grey horizontal line). Shallow curves represent conditions at ~9 km-depth or 250 MPa (Behr and Platt, 2011), with varying cohesion values (10 MPa - green, 50 MPa - purple), and μ = 0.6. Steeper curves represent Whipple Mountain shear zone conditions determined for this study with pressure values of 750 MPa, varying cohesion (10 MPa – blue, 50 MPa – orange), and μ = 0.6. Shaded rhombohedron highlights the lambda values determined for this study. Courtesy of, and modified in collaboration with, Andrew Zuza.

3.8 References

Anderson, J.L. & Cullers, R.L. (1990) Middle to upper crustal plutonic construction of a magmatic arc; An example from the Whipple Mountains metamorphic core complex. J.L. Anderson (Ed.), The Nature and Origin of Cordilleran Magmatism: Geological Society of America Memoir, 174 (1990), pp. 47-69

Axen, G. J. (2020). How a strong low-angle normal fault formed: The Whipple detachment, southeastern California. *GSA Bulletin*, *132*(9-10), 1817-1828.

Bachmann, F., Hielscher, R., & Schaeben, H. (2010). Texture analysis with MTEX–free and open-source software toolbox. *Solid state phenomena*, *160*, 63-68.

Behr, W. M., & Platt, J. P. (2011). A naturally constrained stress profile through the middle crust in an extensional terrane. *Earth and Planetary Science Letters*, *303*(3-4), 181-192.

Behr, W. M., & Platt, J. P. (2014). Brittle faults are weak, yet the ductile middle crust is strong: Implications for lithospheric mechanics. *Geophysical Research Letters*, *41*(22), 8067-8075.

Berman, R. G. (1990). Mixing properties of Ca-Mg-Fe-Mn garnets. *American Mineralogist*, *75*(3-4), 328-344.

Byerlee, J. D. (1968). Brittle-ductile transition in rocks. *Journal of Geophysical Research*, *73*(14), 4741-4750.

Byerlee, J. (1978). Friction of rocks. *Rock friction and earthquake prediction*, 615-626.

Campbell, L. R., & Menegon, L. (2019). Transient high strain rate during localized viscous creep in the dry lower continental crust (Lofoten, Norway). *Journal of Geophysical Research: Solid Earth*, *124*(10), 10240-10260.

Chapman, A. D., Kidder, S., Saleeby, J. B., & Ducea, M. N. (2010). Role of extrusion of the Rand and Sierra de Salinas schists in Late Cretaceous extension and rotation of the southern Sierra Nevada and vicinity. *Tectonics*, *29*(5).

Crittenden, M. D., Coney, P. J., Davis, G. H., & Davis, G. H. (Eds.). (1980). Cordilleran metamorphic core complexes (Vol. 153). Geological Society of America.

Cross, A. J., Prior, D. J., Stipp, M., & Kidder, S. (2017). The recrystallized grain size piezometer for quartz: An EBSD-based calibration. *Geophysical Research Letters*, *44*(13), 6667-6674.

Davis, G. A., Anderson, J. L., Frost, E. G., & Shackelford, T. J. (1980). Mylonitization and detachment faulting in the Whipple-Buckskin-Rawhide Mountains terrane, southeastern California and western Arizona.

Davis, G. A. (1988). Rapid upward transport of mid-crustal mylonitic gneisses in the footwall of a Miocene detachment fault, Whipple Mountains, southeastern California. *Geologische Rundschau*, *77*, 191-209.

Davis, G. H. (1980). Structural characteristics of metamorphic core complexes, southern Arizona. Cordilleran Metamorphic Core Complexes, Max D. Crittenden, Jr., Peter J. Coney, George H. Davis

Dresen, G., Duyster, J., Stöckhert, B., Wirth, R., & Zulauf, G. (1997). Quartz dislocation microstructure between 7000 m and 9100 m depth from the Continental Deep Drilling Program KTB. *Journal of Geophysical Research: Solid Earth*, *102*(B8), 18443-18452.

Ferry, J. T., & Spear, F. S. (1978). Experimental calibration of the partitioning of Fe and Mg between biotite and garnet. *Contributions to mineralogy and petrology*, *66*(2), 113-117.

Fossen, H. (2016). *Structural geology*. Cambridge university press.

Fredrich, J. T., Evans, B., & Wong, T. F. (1989). Micromechanics of the brittle to plastic transition in Carrara marble. *Journal of Geophysical Research: Solid Earth*, *94*(B4), 4129-4145.

Gleason, G. C., & Tullis, J. (1995). A flow law for dislocation creep of quartz aggregates determined with the molten salt cell. *Tectonophysics*, *247*(1-4), 1-23.

Hacker, B. R. (1991). The role of deformation in the formation of metamorphic gradients: ridge subduction beneath the Oman ophiolite. *Tectonics*, *10*(2), 455-473.

Hacker, B. R., Yin, A., Christie, J. M., & Davis, G. A. (1992). Stress magnitude, strain rate, and rheology of extended middle continental crust inferred from quartz grain sizes in the Whipple Mountains, California. *Tectonics*, *11*(1), 36-46.

Harrison, T. M., Grove, M., Lovera, O. M., & Catlos, E. J. (1998). A model for the origin of Himalayan anatexis and inverted metamorphism. *Journal of Geophysical Research: Solid Earth*, *103*(B11), 27017-27032.

Hirsch, P. B., & Roberts, S. G. (1997). Modelling plastic zones and the brittle-ductile transition. *Philosophical Transactions of the Royal Society of London. Series A: Mathematical, Physical and Engineering Sciences*, *355*(1731), 1991-2002.

Hirth, G., & Tullis, J. A. N. (1992). Dislocation creep regimes in quartz aggregates. *Journal of structural geology*, *14*(2), 145-159.

Hirth, G., Teyssier, C., & Dunlap, J. W. (2001). An evaluation of quartzite flow laws based on comparisons between experimentally and naturally deformed rocks. *International Journal of Earth Sciences*, *90*, 77-87.

Hobbs, B. E., Ord, A., & Teyssier, C. (1986). Earthquakes in the ductile regime?. *Pure and Applied Geophysics*, *124*, 309-336.

Hoisch, T. D. (1990). Empirical calibration of six geobarometers for the mineral assemblage quartz+ muscovite+ biotite+ plagioclase+ garnet. *Contributions to Mineralogy and Petrology*, *104*(2), 225-234.

Jaeger, J. C., and N. G. W. Cook, Fundamentals of Rock Mechanics, 3rd ed., Chapman and Hall, London, 1979.

Jäger, P., Schmalholz, S. M., Schmid, D. W., & Kuhl, E. (2008). Brittle fracture during folding of

rocks: A finite element study. *Philosophical Magazine*, *88*(28-29), 3245-3263.

Jaeger, J. C., Cook, N. G. W., & Zimmerman, R. (2009). Fundamentals of rock mechanics. John Wiley & Sons.

Jaoul, O., Tullis, J., & Kronenberg, A. (1984). The effect of varying water contents on the creep behavior of Heavitree quartzite. *Journal of Geophysical Research: Solid Earth*, 89(B6), 4298-4312.

Koch, P. S., Christie, J. M., Ord, A., & George Jr, R. P. (1989). Effect of water on the rheology of experimentally deformed quartzite. *Journal of Geophysical Research: Solid Earth*, *94*(B10), 13975-13996.

Kohlstedt, D. L., & Weathers, M. S. (1980). Deformation-induced microstructures, paleopiezometers, and differential stresses in deeply eroded fault zones. *Journal of Geophysical Research: Solid Earth*, *85*(B11), 6269-6285.

Kohlstedt, D. L., Evans, B., & Mackwell, S. J. (1995). Strength of the lithosphere: Constraints imposed by laboratory experiments. *Journal of Geophysical Research: Solid Earth*, *100*(B9), 17587-17602.

Kronenberg, A. K., & Tullis, J. (1984). Flow strengths of quartz aggregates: grain size and pressure effects due to hydrolytic weakening. *Journal of Geophysical Research: Solid Earth*, 89(B6), 4281-4297.

Kruhl, J. H., & Vernon, R. H. (2005). Syndeformational emplacement of a tonalitic sheet-complex

in a late-Variscan thrust regime: Fabrics and mechanism of intrusion, Monte'E Senes, Northeastern Sardinia, Italy. *The Canadian Mineralogist*, *43*(1), 387-407.

Labuz, J. F., & Zang, A. (2014). Mohr–Coulomb failure criterion. In *The ISRM Suggested Methods for Rock Characterization, Testing and Monitoring: 2007-2014* (pp. 227-231). Cham: Springer International Publishing.

Lavier, L. L., & Manatschal, G. (2006). A mechanism to thin the continental lithosphere at magma-poor margins. *Nature*, *440*(7082), 324-328.

Lusk, A. D., Platt, J. P., & Platt, J. A. (2021). Natural and experimental constraints on a flow law for dislocation-dominated creep in wet quartz. *Journal of Geophysical Research: Solid Earth*, *126*(5), e2020JB021302.

Moulas, E., Schmalholz, S. M., Podladchikov, Y., Tajčmanová, L., Kostopoulos, D., & Baumgartner, L. (2019). Relation between mean stress, thermodynamic, and lithostatic pressure. *Journal of metamorphic geology*, *37*(1), 1-14.

Noël, C., Passelègue, F. X., & Violay, M. (2021). Brittle faulting of ductile rock induced by pore fluid pressure build-up. *Journal of Geophysical Research: Solid Earth*, *126*(3), e2020JB021331.

Nüchter, J. A., & Stöckhert, B. (2008). Coupled stress and pore fluid pressure changes in the middle crust: Vein record of coseismic loading and postseismic stress relaxation. *Tectonics*, *27*(1).

Nunn, J. A. (1996). Buoyancy-driven propagation of isolated fluid-filled fractures: Implications f

or fluid transport in Gulf of Mexico geopressured sediments. *Journal of Geophysical Research: Solid Earth*, *101*(B2), 2963-2970.

Parrish, D. K., Krivz, A. L., & Carter, N. L. (1976). Finite-element folds of similar geometry. Tectonophysics, 32(3-4), 183-207.

Paterson, M. S., & Luan, F. C. (1990). Quartzite rheology under geological conditions. *Geological Society, London, Special Publications*, *54*(1), 299-307.

Paterson, M. S., & Wong, T. F. (2005). Micromechanics of brittle fracture. *Experimental Rock Deformation—The Brittle Field*, 115-145.

Ramsay, J. G. (1980). The crack–seal mechanism of rock deformation. *Nature*, *284*(5752), 135-139.

Rutter, E. H., & Brodie, K. H. (2004). Experimental intracrystalline plastic flow in hot-pressed synthetic quartzite prepared from Brazilian quartz crystals. *Journal of Structural Geology*, *26*(2), 259-270.

Sachau, T., Bons, P. D., & Gomez-Rivas, E. (2015). Transport efficiency and dynamics of hydraulic fracture networks. *Frontiers in Physics*, *3*, 63.

Schueller, S., & Davy, P. (2008). Gravity influenced brittle-ductile deformation and growth faulting in the lithosphere during collision: Results from laboratory experiments. *Journal of Geophysical Research: Solid Earth*, *113*(B12).

Seno, T. (2009). Determination of the pore fluid pressure ratio at seismogenic megathrusts in

subduction zones: Implications for strength of asperities and Andean-type mountain building. *Journal of geophysical research: Solid Earth*, *114*(B5).

Shen, J., Priest, S. D., & Karakus, M. (2012). Determination of Mohr–Coulomb shear strength parameters from generalized Hoek–Brown criterion for slope stability analysis. *Rock mechanics and rock engineering*, *45*, 123-129.

Sibson, R. H. (1977). Fault rocks and fault mechanisms. Journal of the Geological Society, 133(3), 191-213.

Sibson, R. H. (1986). Earthquakes and rock deformation in crustal fault zones. Annual Review of Earth and Planetary Sciences, Vol. 14, p. 149, 14, 149.

Soleymani, H., Kidder, S., Hirth, G., & Garapić, G. (2020). The effect of cooling during deformation on recrystallized grain-size piezometry. *Geology*, *48*(6), 531-535.

Sterner, S. M., & Pitzer, K. S. (1994). An equation of state for carbon dioxide valid from zero to extreme pressures. *Contributions to Mineralogy and Petrology*, *117*(4), 362-374.

Stipp, M., Stünitz, H., Heilbronner, R., & Schmid, S. M. (2002). Dynamic recrystallization of quartz: correlation between natural and experimental conditions. *Geological Society, London, Special Publications*, *200*(1), 171-190.

Stipp, M., & Kunze, K. (2008). Dynamic recrystallization near the brittle-plastic transition in naturally and experimentally deformed quartz aggregates. *Tectonophysics*, *448*(1-4), 77-97.

Stöckhert, B., Brix, M. R., Kleinschrodt, R., Hurford, A. J., & Wirth, R. (1999). Thermochronometry and microstructures of quartz—a comparison with experimental flow laws and predictions on the temperature of the brittle–plastic transition. *Journal of Structural Geology*, *21*(3), 351-369.

Tajčmanová, L., Podladchikov, Y., Powell, R., Moulas, E., Vrijmoed, J. C., & Connolly, J. A. D. (2014). Grain-scale pressure variations and chemical equilibrium in high-grade metamorphic rocks. *Journal of Metamorphic Geology*, *32*(2), 195-207.

Tjioe, M., & Borja, R. I. (2015). On the pore-scale mechanisms leading to brittle and ductile deformation behavior of crystalline rocks. *International Journal for Numerical and Analytical Methods in Geomechanics*, *39*(11), 1165-1187.

Tullis, J., Shelton, G. L., & Yund, R. A. (1979). Pressure dependence of rock strength: implications for hydrolytic weakening. *Bulletin de Minéralogie*, *102*(2), 110-114.

Twiss, R. J., & Moores, E. M. (1992). *Structural geology*. Macmillan.

Walther, J. V., & Orville, P. M. (1982). Volatile production and transport in regional metamorphism. *Contributions to Mineralogy and Petrology*, *79*, 252-257.

Wang, L., Kwiatek, G., Rybacki, E., Bonnelye, A., Bohnhoff, M., & Dresen, G. (2020). Laboratory study on fluid-induced fault slip behavior: The role of fluid pressurization rate. *Geophysical Research Letters*, *47*(6), e2019GL086627.

Warren, J. M., & Hansen, L. N. (2023). Ductile deformation of the lithospheric mantle. *Annual*

Review of Earth and Planetary Sciences, *51*(1), 581-609.

Whitney, D. L., Teyssier, C., Rey, P., & Buck, W. R. (2013). Continental and oceanic core complexes. *Bulletin*, *125*(3-4), 273-298.

Zuza, A. V., Cao, W., Rodriguez-Arriaga, A., DesOrmeau, J. W., & Odlum, M. L. (2022). Strain localization at brittle-ductile transition depths during Miocene magmatism and exhumation in the southern Basin and Range. *Journal of Structural Geology*, *163*, 104709.

4 Tectonic Model for the Evolution of the Whipple Mountains

4.1 Abstract

Multiple models have been proposed for the evolution of the Whipple Mountains, which serves as a model Orocopia emplacement and Miocene extension, but none explain all structural, lithologic and temporal observations. We propose a new model which explicitly relates Whipple Mountains evolution to Laramide flat subduction. The model successfully accounts for: 1) Paleocene zircon crystallization; 2) syn-kinematic monazite-in-garnet inclusion ages; 3) high-temperature metamorphism conditions; 4) Miocene extension; and 5) structural relations amongst the complex history of the Whipple Mountains shear zone evolution. The continued improvement of analytical tools provides new insight into P-T-t conditions which allow for new interpretations of Earth's geologic history.

4.2 Introduction

The Whipple Mountains of southeastern California are the birthplace of the modern concept of low-angle detachment faulting associated with large-scale continental extension (Coney et al., 1980; Davis, G.H., 1987; Davis & Coney, 1979; Lister et al., 1984; Murphy et al., 2002; Whitney et al., 2013). The Whipple detachment fault system consists of the classic structural association including a low-angle brittle detachment fault that is warped into a domal shape, an extended hanging wall involving tilted syn-extensional strata, and a mylonitic shear directly below the detachment fault (Coney et al., 1980; Davis, , 1987; Davis & Coney, 1979; Lister et al., 1984; Gans and Gentry, 2016). It has been long noted that the Whipple mylonitic shear zone is remarkably thick (>3.9 km) without exposing its base (Davis et al., 1980, 1982). This observation has been attributed to the capture of a sub-horizontal middle-crustal shear zone that linked the

western Mojave rift system in the Barstow area to the Lower Colorado River extensional corridor system (Jacobson et al., 2011; Seymour et al., 2018).

The earliest studies recognize that southeastern California was at or near the boundary between the Pacific and North American plates prior to the Mesozoic Era (Crowley, 1981). Clues as to how these two tectonic plates interacted in the past is preserved in the age and deformational history of rocks throughout western North America. Over the past 50 years, various groups have modeled metamorphic core-complex and detachment faulting evolution. Ernst (1981) summarized 5 different developmental stages in southeastern California: (1) a convergent continental margin consisting of middle to late Precambrian volcanic and plutonic rocks; (2) a rifted, late Precambrian to Paleozoic North American margin; (3) a Paleozoic to Mesozoic era island arc plus a basin adjacent to the continent; (4) Mesozoic to Cenozoic convergence; and (5) a complex late Cenozoic transform system. All stages were thought to have low-angle subduction, periods with high erosion rates, and ongoing volcanism or plutonism (Ernst, 1981; Anderson et al., 1988; Gans and Gentry, 2016).

Chapter 2 described our current understanding of low-angle detachment faulting and showed that models suggesting the detachments root no deeper than the upper crust are inconsistent with the high-pressure, high-temperature conditions experienced in the Whipple Mountains brittle-ductile shear zone. Recent studies suggest that the Orocopia schist was emplaced beneath core-complexes in southeastern California and Arizona (Kapp et al., 2023; Jacobson et al., 2011; Seymour et al., 2018; Strickland et al.., 2018). Proposed models suggest diapir-style emplacement of the Orocopia schist (Chapman, 2021), underplating material horizontally without subduction (Strickland et al., 2018), and schist underplating with shallow-slab subduction (Chapman et al., 2021) (Chapter 2, Figure 2.5). Here, I propose a similar model

for the evolution of the Whipple Mountains that accounts for a heating event during the Paleocene using detrital zircon ages from gabbro and schist rocks in the shear zone.

4.3 Methods

Zircon were extracted from sampled rocks using standard mineral separation procedures (i.e. crushing, sieving, pulverizing, panning, Frantz magnetic separator, and heavy liquids). Zircons were hand-picked under a microscope and mounted on double-sided adhesive tape. Approximately 600-100 grains from each sample were analyzed by Laser Ablation Inductively Coupled Mass Spectrometry (LA-ICP-MS) at the University of Texas, Austin following the procedures of Hart et al. (2016) (Table 2). A large spot size (50 μm) and long ablation time (60 s) were used so that each grain was continuously analyzed from the surface to a depth of approximately 35 μm (close to the grain center in most cases). U-Pb zircon data were carefully evaluated, considering discordance, data precision, and data mode robustness (Liu and Stockli, 2019). $^{206}Pb/^{238}U$ ages were selected for grains <850 Ma and $^{207}Pb/^{206}Pb$ ages for grains >850 Ma, the degree of discordance assessed between $^{206}Pb/^{238}U$ and $^{205}Pb/^{237}U$ ages (Liu and Stockli, 2019). Grains ≥850 Ma with >30% discordance and grains <850 Ma with >10% discordance were not further considered, as well as grains with >10% analytical error (Liu and Stockli, 2019). Internal errors are quoted at the 2σ level and "best ages" refer to the isotopic system that best represents the age of the grain (Gehrels et al., 2008; Horstwood et al., 2016). U-Pb zircon data was also collected for mafic samples within the shear zone, samples VJ313-1b and VJ314-1 were collected using the CAMECA ion mass spectrometer-1290 at the University of California, Los Angeles. U-Pb data for mafic sample VJ-02-19-22-2A and felsic samples VJ-04-03-22-1, VJ-03-11-22-1, and VJ-03-11-22-2, were collected at the Chinese Academy of Sciences laboratory (Table 4, 5).

Garnet-bearing thin sections were imaged under a petrographic microscope to determine if garnets contained monazite inclusions. Samples were sawn and mounted along with a monazite Th-Pb standard (554) within 1" epoxy rings that was then filled with epoxy. Polished mounts were analyzed using the Tescan Vega-3 XMU variable-pressure Scanning Electron Microscope at the University of California, Los Angeles (UCLA). Backscattered electron imagery highlights compositional variations in the sample and EDAX energy-dispersive analysis was used to determined elemental variations in the sample as well as to verify the presence of monazite inclusions in garnets. Monazite Th-Pb ages were obtained using the CAMECA ims-1290 (methods described in Chapter 2 of this thesis) (Harrison et al., 1995). Bulk rock geochemistry of several samples was obtained via inductively coupled plasma (ICP) mass spectrometry at Activation Laboratories, Ltd. (Table 6).

4.4 Results

Samples from varying structural depths across the Whipple detachment were collected and their crystallization and/or deformation ages were determined (Figure 4.1). A non-mylonitized, highly fractured, felsic gneiss sample (VJ-03-12-22-1) from the hanging wall at the base of the detachment yielded Proterozoic ages (1.9-1.7 Ga, $^{207}Pb/^{206}Pb$) (Table 5). Across the detachment, a mylonitized granitoid sample with epidote veining from the footwall of the detachment yielded weighted mean zircon $^{206}Pb/^{238}U$ deformation age of 24.1 ± 0.2 Ma and a smaller population of 68.3 ± 0.5 Ma with scattered dates from the Jurassic, Triassic and Proterozoic (Table 5). Both of these samples were collected along Powerline Rd., in the eastern edge of the Whipple Mountains (Figure 4.1). A fine-grained felsic dike sample was collected from the southwest edge of the detachment and yielded a weighted mean age of 63.9 ± 0.5 Ma ($^{206}Pb/^{238}U$). The felsic samples were plotted along with Gans and Gentry (2016) xenocryst zircon ages in Figure 4.2.

Three separate gabbro samples were collected and dated, two of these yielded ages spanning various geologic periods including the Late Cretaceous, Jurassic, Triassic, and Proterozoic (Table 4). Of special interest are the Late Cretaceous ages where sample VJ-03-13-22-1B has a weighted mean age of 83.0 ± 3.1 Ma ($^{206}Pb/^{238}U$, MSWD 1.48) and sample VJ-03-14-22-1 is a gabbro from the northwest base of the detachment (near War Eagle Mine) and has a weighted mean age of 87.3 ± 3.8 Ma ($^{206}Pb/^{238}U$, MSWD 1.04). Gabbro samples VJ-02-19-22-2A, in the mylonitic footwall, and VJ-102420-1C, in the non-mylonitic footwall yielded only Proterozoic ages ranging from 1.7-1.2 Ga ($^{207}Pb/^{206}Pb$).

Detrital zircons from extracted from garnet-bearing quartzofeldspathic gneiss and garnet-bearing schists were dated by the U-Pb SIMS (Table 2). Most of these samples yielded $^{207}Pb/^{206}Pb$ Proterozoic ages (VJ-10-24-20-8A, VJ-10-24-20-7A, and VJ-10-24-20-1B). However, sample VJ-10-24-20-7A also yielded a Late Cretaceous to Paleocene age with a weighted mean of 70.0 ± 0.5 Ma ($^{206}Pb/^{238}U$, MSWD 3.5 due to a rage of 62-93 Ma ages). The schist and gneiss zircon ages were plotted along with zircon ages from Seymour et al. (2018) (Figure 4.3).

Monazite-in-garnet ages resulted in two separate age estimates for two separate samples. Sample VJ-03-12-22-4 is a garnet-biotite schist with a weighted mean age of 63.2±1.9 Ma ($^{206}Pb/^{238}U$, MSWD 1.3) as well as a Proterozoic population (Table 1). A garnet-mica schist interlayered with quartzofeldspathic gneiss (sample VJ-03-12-22-10A) yielded monazite inclusion weighted mean age of 55.7± 2.0 Ma ($^{206}Pb/^{238}U$, MSWD 1.7) as well as scattered Late Cretaceous, Triassic, and Proterozoic ages (Table 1).

Three samples (i.e., VJ-03-12-22-4, VJ-03-12-22-12, VJ-02-19-22-2A) whose elemental concentration was plotted against a mafic schist sample from the Orocopia Mountains, yield distinctly different signatures (Figure 4.4). Dawson & Jacobson, (1989) paper shows that the

Orocopia protolith is a metabasalt (i.e. MORB, so has a basically flat trace element pattern) (Figure 4.4) .However, the three samples closest to a metabasalt – i.e., the gabbro and two schists, have fractionated trace element patterns, particularly much higher LREE (La, Ce) and very high incompatible element concentrations (Rb, Ba). They also show a negative Ti anomaly, which the Dawson data doesn't show. Interestingly too, there is a Nb-Ta negative anomaly (Figure 4.4).

4.5 Proposed Model and Discussion

The starting point of my model is that a syn-kinematic heating event, revealed by the aforementioned geochronologic results, at ~60 Ma was induced by hinge-zone retreat and injection of hot mantle beneath the North America continent during the flat or low-angle Laramide subduction (Grove et al., 2003; Jacobson et al., 2011; Kapp et al., 2023; Fig. 4B). The overlapping Late Cretaceous to Paleocene zircon and monazite ages (Table 1) together with results from prior studies (Gans and Gentry, 2016; Kapp et al., 2023; Seymour et al., 2018) suggest a metamorphic event at that time. The proposed model (Figure 4.5A) suggests steep subduction of the Farallon plate beneath the North American plate at 85-75 Ma placing accretionary wedge material next to forearc basin rocks and arc magmatism inland in the eastern Mojave. Arc magmatism may overlap with extended plutonism emplacement of the peraluminous granite Whipple Wash suite (89± 3 Ma) and the metaluminous Axtel quartz diorite (73± 3 Ma) (Anderson et al., 1988; Anderson and Cullers, 1990; Anderson and Crowley, 1981; Howard and John, 1987). Heating beneath this proposed arc magmatism would emplace a hot, juvenile root beneath the Mojave arc and induce partial melting at the base of the continental crust where there is evidence of eastward movement of arc magmatism prior to 90 Ma (Jacobson et al., 2011). Closing of the slab at 65-55 Ma would form low-angle subduction (Grove et al., 2003; Jacobson et al., 2011) as shown in Figure 4.5(B) that would initiate east-directed thrusting of the accretionary wedge, forearc basin, and basement

rocks. Inward migration of the magmatic arc at this time appears to be linked with cessation of magmatism in the Mojave region and the development of the Big Maria Thrust Belt (Seymour et al., 2018). I suggest subcontinental slab rollback and heating due to asthenospheric upwelling occurred around 60-50 Ma that produces a magmatic arc and sequential emplacement of subducted materials (i.e., accretionary-wedge complex, forearc-basin strata Proterozoic basement, and latest Cretaceous arc intrusions) by downward migration of thrusting that overlaps with the zircon and monazite ages in this study.

Figure 4.5(C) shows a return to flat subduction at 55-40 Ma that preserves the latest Laramide-age tectonites as well as a thrust sequence in crust that contains the Pelona-Orocopia-Rand schists as well as signatures of the lower most crust and upper mantle lithosphere in xenoliths (Chapman et al., 2020; Kapp et al., 2023; Seymour et al., 2018). A final slab rollback of the subducting plate at 25-20 Ma (Figure 4.5(D)) would produce widespread intrusive activity that may corresponds with 26± 5 Ma tonalite sills, 21.5 ± 0.7 Ma diabase and ~20.8 ± 0.8 Ma dacite intrusions of the Chambers Wells dike swarm (Gans and Gentry, 2016). At this time, the Whipple detachment fault may be placed to accommodate intra-arc detachment faulting and would capture Miocene mylonitization and highlight how the detachment roots into the middle to lower crust. Furthermore, the hanging wall felsic gneiss sample ages also overlapped with Miocene extension at 24.1 ± 0.2 Ma.

In this model, injecting juvenile material into the base of the crust would explain the high temperature (750°C) syn-kinematic metamorphism (see Chapter 2) at a time when the magmatic arc was located farther to the east along the western margin of the Colorado plateau (Kapp et al., 2023). However, the high temperature of the syn-kinematic metamorphism cannot be explained by diapiric flow as proposed by Chapman et al. (2020), which predicts much cooler temperatures

during the emplacement of the footwall gneiss complexes which I interpret as a middle-crustal tectonic mélange. Flat-slab subduction models like that of Axen et al. (2018) do not account for Pelona-Orocopia-Rand schist emplacement nor the 80-55 Ma or the >700°C thermal event. Copeland et al. (2017) highlighted the spatial distribution of arc magmatism across the western North America noting the 85-55 Ma change in distance with respect to the trench. It is also important to note that Th/U ratios in zircons can be used to distinguish between magmatic and metamorphic zircon growth where high Th/U ratios correspond to magmatic zircon crystallizing at high temperatures and low Th/U ratios indicate metamorphic zircons growing at lower crystallization temperatures (Harrison and Watson, 1983; Odlum et al., 2024). The Th/U ratios of zircons in this study suggest both magmatic and metamorphic zircon growth due to their wide range in ratios thus further analysis must be done to separate the two. Trace element data suggests to me a possible arc/subduction origin. Gabbro samples with Proterozoic and Cretaceous ages suggesting the Laramide overprinted the ~1.5 Ga anorogenic gabbro (Anderson, 1989) and 1.5-1.4 Ga granites. These dates are much older than the 19 ± 2 Ma gabbro from the War Eagle pluton, which is interpreted as the youngest intrusion in the Whipple Mountains (Gans and Gentry, 2016).

4.6 Conclusions

The purpose of this model was to determine if the Whipple detachment fault system and its associated low-angle detachment lined the western Mojave rift system in the Barstow area to the Lower Colorado River extensional corridor system. To test this hypothesis, samples were systematically collected from the Whipple shear-zone rocks to establish the age of the shear-zone protolith and the timing of mylonitic deformation. U-Pb zircon dating shows that the shear zone is composed of (1) ~1.6 Ga, ~1.1 Ga, and ~75 Ma gabbros, (2) 75-65 Ma and 23-20 Ma mylonitic felsic intrusions, and (3) detrital zircon ages ranging from 50 Ma to 1.6 Ga. U-Th Ion-microprobe

Th-Pb dating of monazite-inclusions in syn-kinematic garnet yields an age spread of 79 to 62 Ma, 59 Ma to 51 Ma, and 66 to 56 Ma. A thermobarometric study on the garnet-bearing rock sample, from which the monazite ages were obtained, indicates the peak syn-kinematic metamorphism occurred at T = 750 C and P = 7.5 kbar. An interesting result from the detrital zircon dating is that a significant number of younger zircons are clustered at 60-50 Ma, overlapping the interpreted peak metamorphic age of 63-55 Ma obtained from U-Th monazite dating. The lack of 60-50 Ma plutons in the mylonitic gneisses and the high U/Th ratios indicate that the 60-50 Ma detrital zircons may have resulted from a heating event. Because the arc was located east of the Whipple Mountains at 60-50 Ma, the required heating event could have been induced by sub-crustal slab steepening and the associated mantle upwelling. This interpretation adds more complexities for the Laramide flat subduction in the SW United States and the formation of the Whipple detachment system. Specifically, the new interpretation predicts the mylonitic front as the top of a Laramide mid- crustal shear zone, the Whipple shear-zone rocks were originated from the middle-crustal mélange complex consisting of a mixture of the Proterozoic basement rocks and the western Mojave arc root intruded later by Miocene felsic rocks.

4.7 Figures

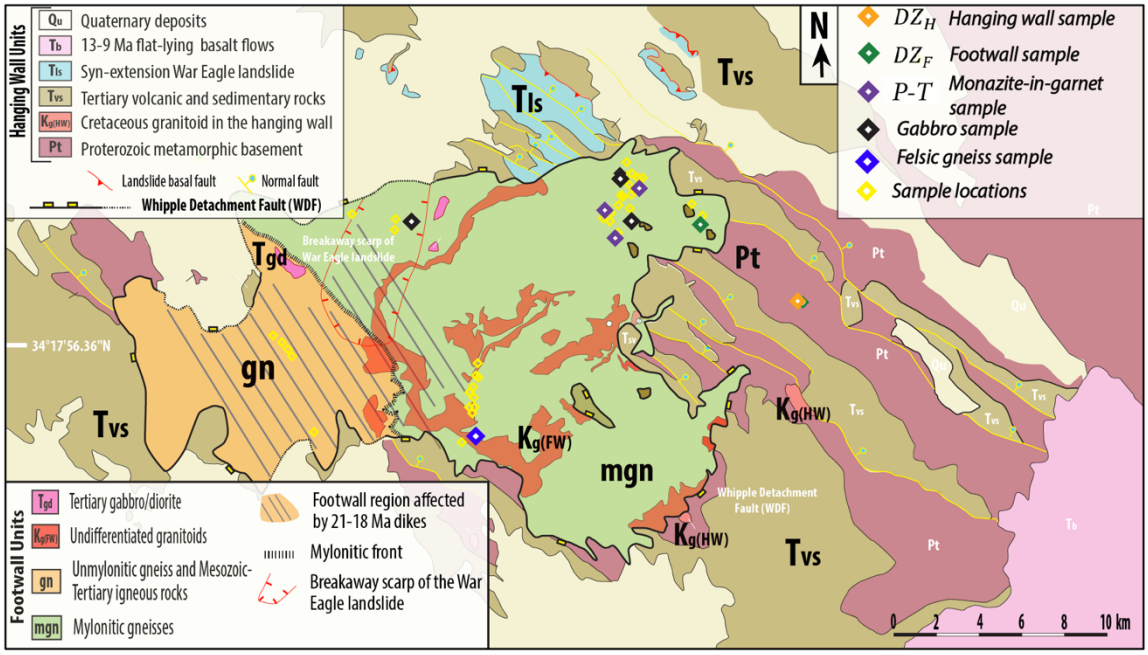

Figure 4.1. Simplified geologic map of the Whipple Mountains, southeastern California with sample locations. Yellow diamonds represent all sample locations from the research area. Bold diamond locations represent samples that were dated either through detrital zircon or monazite-in-garnet U-Th-Pb methods. Modified from Chapter 2 (this thesis) and Gans and Gentry (2016).

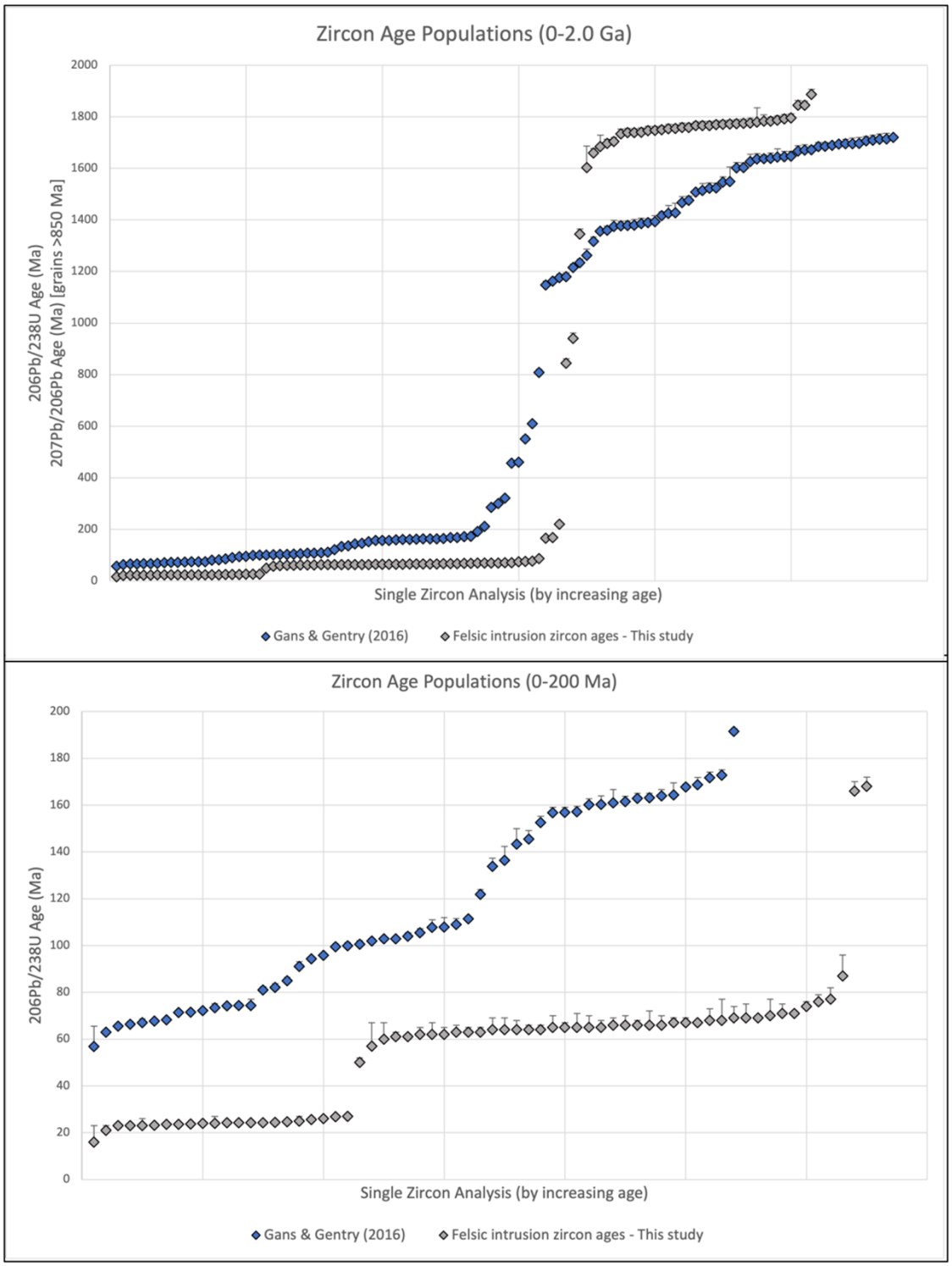

Figure 4.2. (A) Representative U-Pb zircon data showing 2σ uncertainty from felsic intrusions along the Whipple Mountains shear zone up to 2.0 Ga. (B) Same set of U-Pb zircon data with ages only up to 200 Ma. Note that zircon ages fall into discrete groups of ~20 Ma, 60-80 Ma, 160-18 Ma, 1.4 Ga, and 1.6-1.8 Ga. Gans and Gentry (2016) xenocrystic zircon age data plotted in blue diamonds.

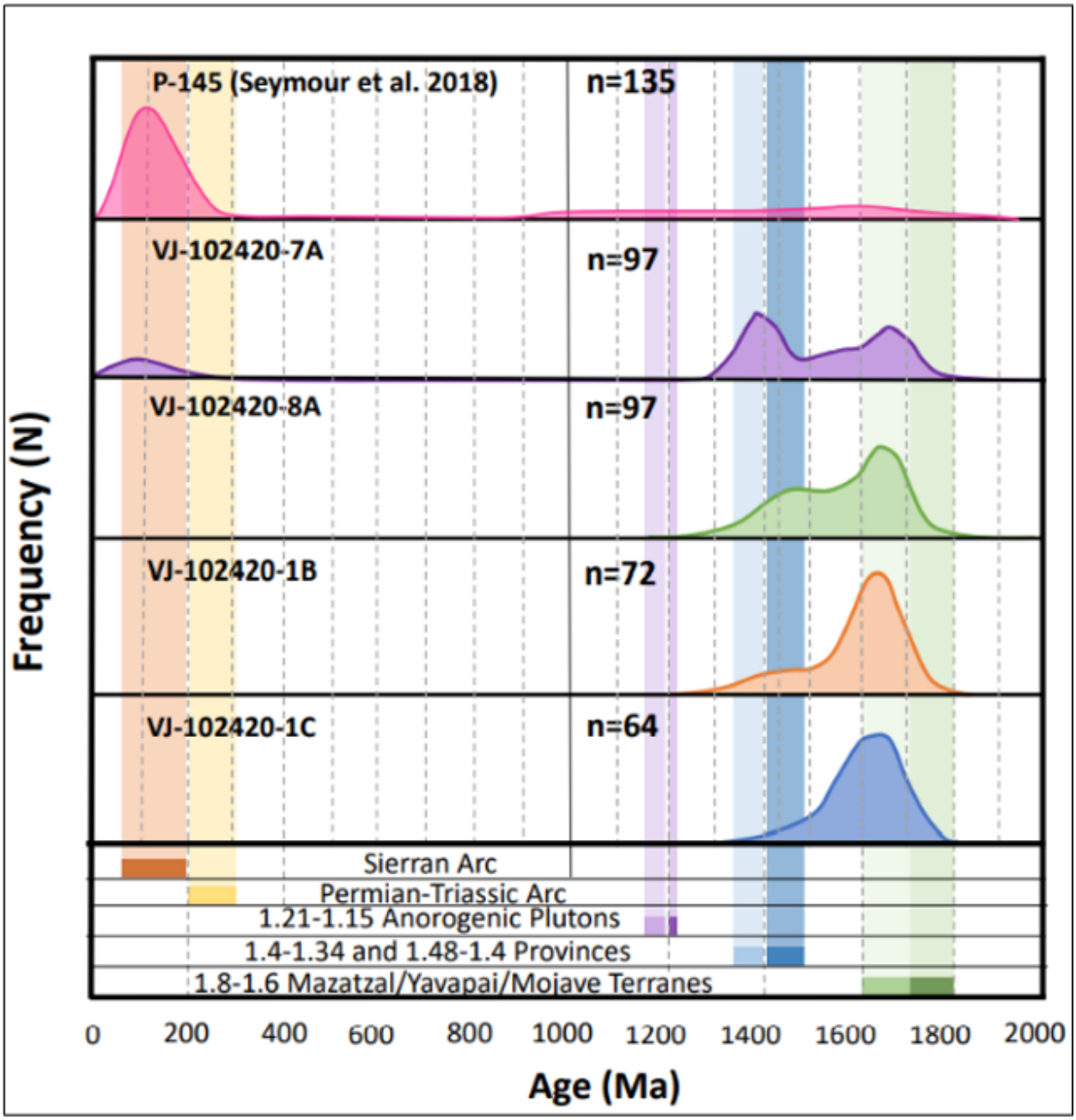

Figure 4.3. Detrital zircon U-Pb age spectra for schist and gneisses ((VJ-102420-1C,7A, 8A) and gabbro sample (VJ-102420-1B) in the Whipple Mountains, California, USA. Figure modified from Seymour et al., (2018) whose zircons U-Pb age spectra from sample P-145 are also plotted. The bottom bar indicate major orogenic and anorogenic events up to 2.0 Ga.

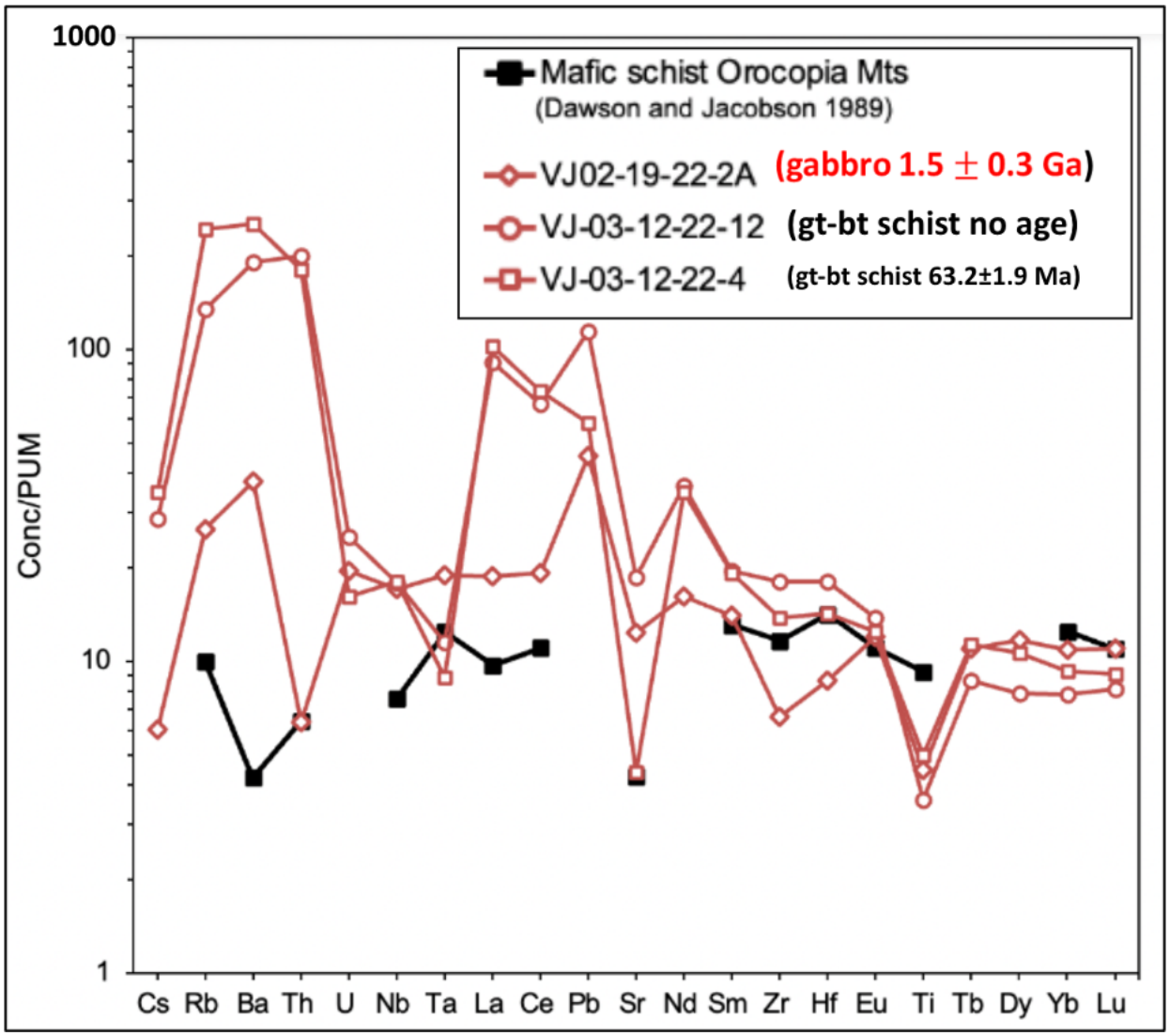

Figure 4.4. Trace element data for three samples from the Whipple Mountains shear zone plotted with a mafic schist sample from Dawson and Jacobson (1989). Trace element concentration is normalized to primitive upper mantle (PUM). Sample VJ-02-19-22-2A is a gabbro sample and samples VJ-03-12-22-12,4 are garnet-mica schists.

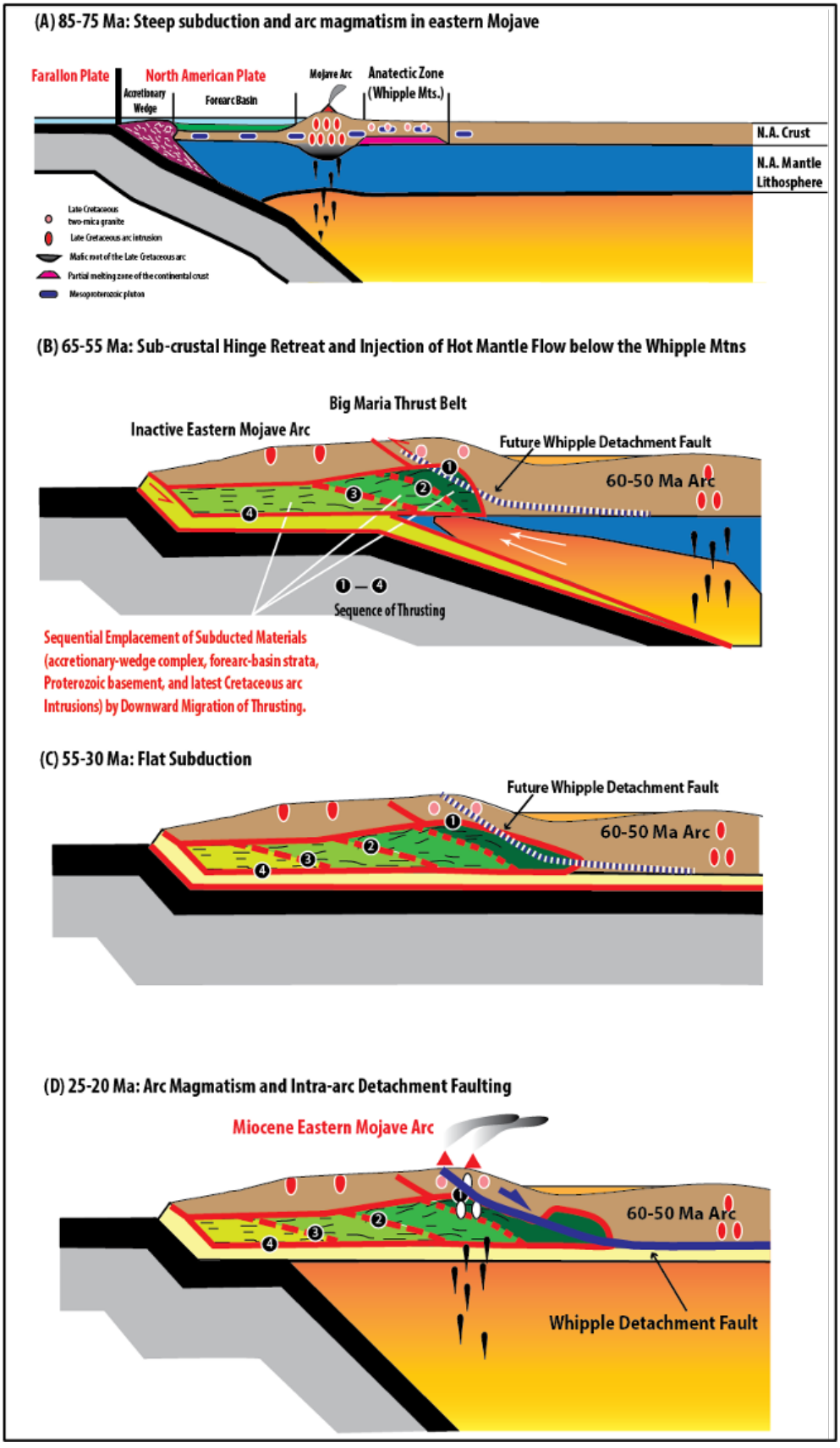
(A) 85-75 Ma: Steep subduction and arc magmatism in eastern Mojave
Farallon Plate
North American Plate
Mojave Arc
Anatectic Zone
(Whipple Mts.)
Accretionary Wedge
Forearc Basin
N.A. Crust
N.A. Mantle Lithosphere
Late Cretaceous two-mica granite
Late Cretaceous arc intrusion
Mafic root of the Late Cretaceous arc
Partial melting zone of the continental crust
Mesoproterozoic pluton
(B) 65-55 Ma: Sub-crustal Hinge Retreat and Injection of Hot Mantle Flow below the Whipple Mtns
Big Maria Thrust Belt
Inactive Eastern Mojave Arc
Future Whipple Detachment Fault
60-50 Ma Arc
1 — 4
Sequence of Thrusting
Sequential Emplacement of Subducted Materials (accretionary-wedge complex, forearc-basin strata, Proterozoic basement, and latest Cretaceous arc Intrusions) by Downward Migration of Thrusting.
(C) 55-30 Ma: Flat Subduction
Future Whipple Detachment Fault
60-50 Ma Arc
(D) 25-20 Ma: Arc Magmatism and Intra-arc Detachment Faulting
Miocene Eastern Mojave Arc
60-50 Ma Arc
Whipple Detachment Fault

Figure 4.5. Proposed tectonic evolution model for the Whipple Mountains. (A) 85-75 Ma steep subduction and arc magmatism (B) 65-55 Ma Eastward arc migration and heating event of the Whipple gneiss complex (C) 55-40 Ma flat subduction (D) 25-20 Ma slab rollback, arc magmatism, and intra-arc detachment faulting. Light pink circles with a white border represent Late-Cretaceous two-mica granites, red ovals with a white border represent Late-Cretaceous arc intrusions, and blue ellipsoids represent Mesoproterozoic plutons. Accretionary wedge (purple in A, yellow in B-D) forearc-basin strata (lime green), and Proterozoic basement rocks (green) represent deformed tectonites (C). White and black inverted tear drops represent magmatism/plutons. Red dashed lines represent thrust faults.

4.8 Tables

Table 4.1. Results of Th-Pb monazite ages for samples analyzed in this study.

Sample	Age (Ma)	Age (Ma)	% Radiogenic
	$^{208}Pb/^{232}Th$	$^{208}Pb/^{232}Th$	^{208}Pb
		1 s.e.	
VJ-03-12-22-10A_VJ10A_1a.ais	903.2	49.0	99.9
VJ-03-12-22-10A_VJ10A_1b.ais	990.4	50.8	99.9
VJ-03-12-22-10A_VJ10A_2a.ais	58.5	2.5	98.0
VJ-03-12-22-10A_VJ10A_2b.ais	50.9	3.3	100.0
VJ-03-12-22-4_VJ4_1a.ais	56.0	4.8	98.4
VJ-03-12-22-4_VJ4_1a@1b.ais	64.5	2.0	97.3
VJ-03-12-22-4_VJ4_3a.ais	1310	65.5	99.7
VJ-03-12-22-4_VJ4_4a.ais	104.7	12.8	93.9
VJ-03-12-22-4_VJ4_5a.ais	1194	28.8	99.8
VJ-03-12-22-4_VJ4_6a.ais	224	58.3	96.5

Table 4.2. Results of detrital zircon ages for schist samples analyzed in this study.

SCHIST AGES

Sample Name	Grain#		Best Age (Ma)	2σ (Ma)
VJ102420-7A	29.FIN2	$^{206}Pb/^{238}U$	62	1
VJ102420-7A	71.FIN2	$^{206}Pb/^{238}U$	67	2
VJ102420-7A	43.FIN2	$^{206}Pb/^{238}U$	69	2
VJ102420-7A	14r.FIN2	$^{206}Pb/^{238}U$	69	2
VJ102420-7A	42.FIN2	$^{206}Pb/^{238}U$	69	2
VJ102420-7A	49.FIN2	$^{206}Pb/^{238}U$	69	2
VJ102420-7A	37.FIN2	$^{206}Pb/^{238}U$	70	6
VJ102420-7A	95.FIN2	$^{206}Pb/^{238}U$	70	2
VJ102420-7A	30.FIN2	$^{206}Pb/^{238}U$	70	3
VJ102420-7A	54.FIN2	$^{206}Pb/^{238}U$	71	3
VJ102420-7A	73.FIN2	$^{206}Pb/^{238}U$	71	2
VJ102420-7A	40.FIN2	$^{206}Pb/^{238}U$	71	2
VJ102420-7A	18.FIN2	$^{206}Pb/^{238}U$	71	2
VJ102420-7A	34.FIN2	$^{206}Pb/^{238}U$	71	2
VJ102420-7A	61.FIN2	$^{206}Pb/^{238}U$	71	3
VJ102420-7A	74.FIN2	$^{206}Pb/^{238}U$	71	2
VJ102420-7A	52r.FIN2	$^{206}Pb/^{238}U$	74	2
VJ102420-7A	91.FIN2	$^{206}Pb/^{238}U$	74	2
VJ102420-7A	86.FIN2	$^{206}Pb/^{238}U$	75	3
VJ102420-7A	26.FIN2	$^{206}Pb/^{238}U$	77	3
VJ102420-7A	13r.FIN2	$^{206}Pb/^{238}U$	77	3
VJ102420-7A	28.FIN2	$^{206}Pb/^{238}U$	93	6
VJ102420-7A	11.FIN2	$^{206}Pb/^{238}U$	123	4
VJ102420-7A	41r.FIN2	$^{207}Pb/^{206}Pb$	1620	90
VJ102420-7A	6.FIN2	$^{207}Pb/^{206}Pb$	1571	62
VJ102420-7A	84.FIN2	$^{207}Pb/^{206}Pb$	1655	49
VJ102420-7A	25.FIN2	$^{207}Pb/^{206}Pb$	1596	31
VJ102420-7A	39.FIN2	$^{207}Pb/^{206}Pb$	1618	33
VJ102420-7A	94.FIN2	$^{207}Pb/^{206}Pb$	1659	50
VJ102420-7A	78.FIN2	$^{207}Pb/^{206}Pb$	1650	28
VJ102420-7A	1.FIN2	$^{207}Pb/^{206}Pb$	1565	32
VJ102420-7A	4.FIN2	$^{207}Pb/^{206}Pb$	1566	41
VJ102420-7A	16.FIN2	$^{207}Pb/^{206}Pb$	1583	64
VJ102420-7A	85.FIN2	$^{207}Pb/^{206}Pb$	1655	23
VJ102420-7A	13c.FIN2	$^{207}Pb/^{206}Pb$	1579	57
VJ102420-7A	77.FIN2	$^{207}Pb/^{206}Pb$	1650	34
VJ102420-7A	31.FIN2	$^{207}Pb/^{206}Pb$	1609	47
VJ102420-7A	36.FIN2	$^{207}Pb/^{206}Pb$	1611	26
VJ102420-7A	51.FIN2	$^{207}Pb/^{206}Pb$	1629	36
VJ102420-7A	33.FIN2	$^{207}Pb/^{206}Pb$	1610	83
VJ102420-7A	45.FIN2	$^{207}Pb/^{206}Pb$	1625	44
VJ102420-7A	10.FIN2	$^{207}Pb/^{206}Pb$	1576	53
VJ102420-7A	32.FIN2	$^{207}Pb/^{206}Pb$	1610	37
VJ102420-7A	21.FIN2	$^{207}Pb/^{206}Pb$	1594	29
VJ102420-7A	65.FIN2	$^{207}Pb/^{206}Pb$	1636	39
VJ102420-7A	90.FIN2	$^{207}Pb/^{206}Pb$	1658	63
VJ102420-7A	19.FIN2	$^{207}Pb/^{206}Pb$	1591	64
VJ102420-7A	87.FIN2	$^{207}Pb/^{206}Pb$	1656	56
VJ102420-7A	60.FIN2	$^{207}Pb/^{206}Pb$	1633	56
VJ102420-7A	69.FIN2	$^{207}Pb/^{206}Pb$	1639	36
VJ102420-7A	22.FIN2	$^{207}Pb/^{206}Pb$	1595	36
VJ102420-7A	50.FIN2	$^{207}Pb/^{206}Pb$	1629	73
VJ102420-7A	15c.FIN2	$^{207}Pb/^{206}Pb$	1582	68
VJ102420-7A	15r.FIN2	$^{207}Pb/^{206}Pb$	1582	53
VJ102420-7A	24.FIN2	$^{207}Pb/^{206}Pb$	1596	28
VJ102420-7A	8.FIN2	$^{207}Pb/^{206}Pb$	1574	51
VJ102420-7A	75.FIN2	$^{207}Pb/^{206}Pb$	1648	39
VJ102420-7A	55.FIN2	$^{207}Pb/^{206}Pb$	1631	78
VJ102420-7A	57.FIN2	$^{207}Pb/^{206}Pb$	1632	33
VJ102420-7A	83.FIN2	$^{207}Pb/^{206}Pb$	1655	63
VJ102420-7A	79.FIN2	$^{207}Pb/^{206}Pb$	1651	52
VJ102420-7A	46.FIN2	$^{207}Pb/^{206}Pb$	1626	25
VJ102420-7A	56.FIN2	$^{207}Pb/^{206}Pb$	1631	32
VJ102420-7A	3.FIN2	$^{207}Pb/^{206}Pb$	1566	36
VJ102420-7A	14c.FIN2	$^{207}Pb/^{206}Pb$	1580	52
VJ102420-7A	5.FIN2	$^{207}Pb/^{206}Pb$	1569	41
VJ102420-7A	81c.FIN2	$^{207}Pb/^{206}Pb$	1652	26
VJ102420-7A	47.FIN2	$^{207}Pb/^{206}Pb$	1626	40
VJ102420-7A	20.FIN2	$^{207}Pb/^{206}Pb$	1594	29
VJ102420-7A	41r.FIN2	$^{207}Pb/^{206}Pb$	1622	73
VJ102420-7A	53.FIN2	$^{207}Pb/^{206}Pb$	1630	35
VJ102420-7A	58.FIN2	$^{207}Pb/^{206}Pb$	1632	61
VJ102420-7A	16.FIN2	$^{207}Pb/^{206}Pb$	1584	37
VJ102420-7A	66.FIN2	$^{207}Pb/^{206}Pb$	1637	37
VJ102420-7A	80.FIN2	$^{207}Pb/^{206}Pb$	1651	37
VJ102420-7A	72.FIN2	$^{207}Pb/^{206}Pb$	1642	26
VJ102420-7A	9.FIN2	$^{207}Pb/^{206}Pb$	1576	37
VJ102420-7A	67.FIN2	$^{207}Pb/^{206}Pb$	1637	27
VJ102420-7A	70.FIN2	$^{207}Pb/^{206}Pb$	1640	29
VJ102420-7A	17.FIN2	$^{207}Pb/^{206}Pb$	1590	27
VJ102420-7A	62.FIN2	$^{207}Pb/^{206}Pb$	1635	28
VJ102420-7A	89.FIN2	$^{207}Pb/^{206}Pb$	1656	22
VJ102420-7A	41c.FIN2	$^{207}Pb/^{206}Pb$	1620	25
VJ102420-7A	35.FIN2	$^{207}Pb/^{206}Pb$	1611	30
VJ102420-7A	2.FIN2	$^{207}Pb/^{206}Pb$	1565	27
VJ102420-7A	93.FIN2	$^{207}Pb/^{206}Pb$	1659	22
VJ102420-7A	48.FIN2	$^{207}Pb/^{206}Pb$	1627	25
VJ102420-7A	64.FIN2	$^{207}Pb/^{206}Pb$	1635	35
VJ102420-7A	7.FIN2	$^{207}Pb/^{206}Pb$	1572	29
VJ102420-7A	81r.FIN2	$^{207}Pb/^{206}Pb$	1653	28
VJ102420-7A	12.FIN2	$^{207}Pb/^{206}Pb$	1578	27
VJ102420-7A	59.FIN2	$^{207}Pb/^{206}Pb$	1633	25
VJ102420-7A	52c.FIN2	$^{207}Pb/^{206}Pb$	1629	37
VJ102420-7A	68.FIN2	$^{207}Pb/^{206}Pb$	1638	23
VJ102420-7A	63.FIN2	$^{207}Pb/^{206}Pb$	1635	39
VJ102420-7A	76.FIN2	$^{207}Pb/^{206}Pb$	1649	28
VJ102420-7A	92.FIN2	$^{207}Pb/^{206}Pb$	1659	30
VJ102420-7A	82.FIN2	$^{207}Pb/^{206}Pb$	1654	31
VJ102420-7A	27.FIN2	$^{207}Pb/^{206}Pb$	1598	28
VJ102420-7A	44.FIN2	$^{207}Pb/^{206}Pb$	1624	33
VJ102420-7A	38.FIN2	$^{207}Pb/^{206}Pb$	1617	26

Table 4.3. Results of detrital zircon ages for schist samples analyzed in this study.

SCHIST AGES								
Sample Name	Grain#		Best Age (Ma)	2σ (Ma)	Sample Name	Grain#	Best Age (Ma)	2σ (Ma)
VJ102420-8A	1.FIN2	$^{207}Pb/^{206}Pb$	1660	60	VJ102420-8A	63.FIN2	1702	42
VJ102420-8A	2.FIN2	$^{207}Pb/^{206}Pb$	1660	33	VJ102420-8A	64.FIN2	1703	42
VJ102420-8A	3.FIN2	$^{207}Pb/^{206}Pb$	1660	27	VJ102420-8A	65.FIN2	1704	34
VJ102420-8A	4.FIN2	$^{207}Pb/^{206}Pb$	1661	41	VJ102420-8A	66.FIN2	1705	34
VJ102420-8A	5.FIN2	$^{207}Pb/^{206}Pb$	1661	38	VJ102420-8A	67.FIN2	1705	35
VJ102420-8A	6.FIN2	$^{207}Pb/^{206}Pb$	1661	33	VJ102420-8A	68.FIN2	1705	35
VJ102420-8A	7.FIN2	$^{207}Pb/^{206}Pb$	1662	35	VJ102420-8A	69.FIN2	1706	34
VJ102420-8A	8.FIN2	$^{207}Pb/^{206}Pb$	1662	47	VJ102420-8A	70.FIN2	1708	39
VJ102420-8A	9.FIN2	$^{207}Pb/^{206}Pb$	1663	45	VJ102420-8A	71.FIN2	1709	30
VJ102420-8A	10.FIN2	$^{207}Pb/^{206}Pb$	1664	43	VJ102420-8A	72.FIN2	1710	34
VJ102420-8A	11.FIN2	$^{207}Pb/^{206}Pb$	1665	32	VJ102420-8A	73.FIN2	1710	29
VJ102420-8A	12.FIN2	$^{207}Pb/^{206}Pb$	1667	82	VJ102420-8A	74.FIN2	1711	27
VJ102420-8A	12.FIN2	$^{207}Pb/^{206}Pb$	1668	33	VJ102420-8A	75.FIN2	1712	93
VJ102420-8A	13.FIN2	$^{207}Pb/^{206}Pb$	1669	44	VJ102420-8A	75.FIN2	1712	44
VJ102420-8A	14.FIN2	$^{207}Pb/^{206}Pb$	1671	25	VJ102420-8A	76.FIN2	1719	33
VJ102420-8A	15.FIN2	$^{207}Pb/^{206}Pb$	1671	31	VJ102420-8A	77.FIN2	1720	45
VJ102420-8A	16.FIN2	$^{207}Pb/^{206}Pb$	1671	34	VJ102420-8A	78.FIN2	1721	29
VJ102420-8A	17.FIN2	$^{207}Pb/^{206}Pb$	1673	36	VJ102420-8A	79.FIN2	1725	30
VJ102420-8A	18.FIN2	$^{207}Pb/^{206}Pb$	1674	75	VJ102420-8A	80.FIN2	1728	52
VJ102420-8A	19.FIN2	$^{207}Pb/^{206}Pb$	1674	29	VJ102420-8A	81.FIN2	1729	28
VJ102420-8A	20.FIN2	$^{207}Pb/^{206}Pb$	1674	33	VJ102420-8A	82.FIN2	1729	32
VJ102420-8A	21.FIN2	$^{207}Pb/^{206}Pb$	1674	33	VJ102420-8A	83.FIN2	1730	34
VJ102420-8A	22.FIN2	$^{207}Pb/^{206}Pb$	1675	33	VJ102420-8A	84.FIN2	1732	52
VJ102420-8A	23.FIN2	$^{207}Pb/^{206}Pb$	1675	52	VJ102420-8A	85.FIN2	1738	39
VJ102420-8A	24.FIN2	$^{207}Pb/^{206}Pb$	1676	47	VJ102420-8A	86.FIN2	1743	43
VJ102420-8A	25.FIN2	$^{207}Pb/^{206}Pb$	1676	33	VJ102420-8A	87.FIN2	1745	34
VJ102420-8A	26.FIN2	$^{207}Pb/^{206}Pb$	1677	32	VJ102420-8A	88.FIN2	1756	38
VJ102420-8A	27.FIN2	$^{207}Pb/^{206}Pb$	1677	36	VJ102420-8A	89.FIN2	1758	37
VJ102420-8A	28.FIN2	$^{207}Pb/^{206}Pb$	1680	30	VJ102420-8A	90.FIN2	1764	34
VJ102420-8A	29.FIN2	$^{207}Pb/^{206}Pb$	1680	30	VJ102420-8A	91.FIN2	1765	31
VJ102420-8A	30.FIN2	$^{207}Pb/^{206}Pb$	1680	32				
VJ102420-8A	31.FIN2	$^{207}Pb/^{206}Pb$	1681	30				
VJ102420-8A	32.FIN2	$^{207}Pb/^{206}Pb$	1681	32				
VJ102420-8A	33.FIN2	$^{207}Pb/^{206}Pb$	1681	30				
VJ102420-8A	34.FIN2	$^{207}Pb/^{206}Pb$	1681	45				
VJ102420-8A	35.FIN2	$^{207}Pb/^{206}Pb$	1681	32				
VJ102420-8A	36.FIN2	$^{207}Pb/^{206}Pb$	1683	32				
VJ102420-8A	37.FIN2	$^{207}Pb/^{206}Pb$	1684	38				
VJ102420-8A	38.FIN2	$^{207}Pb/^{206}Pb$	1684	32				
VJ102420-8A	39.FIN2	$^{207}Pb/^{206}Pb$	1684	42				
VJ102420-8A	40.FIN2	$^{207}Pb/^{206}Pb$	1685	27				
VJ102420-8A	41.FIN2	$^{207}Pb/^{206}Pb$	1685	34				
VJ102420-8A	42.FIN2	$^{207}Pb/^{206}Pb$	1685	29				
VJ102420-8A	43.FIN2	$^{207}Pb/^{206}Pb$	1685	30				
VJ102420-8A	44.FIN2	$^{207}Pb/^{206}Pb$	1687	50				
VJ102420-8A	45.FIN2	$^{207}Pb/^{206}Pb$	1689	45				
VJ102420-8A	46.FIN2	$^{207}Pb/^{206}Pb$	1690	44				
VJ102420-8A	47.FIN2	$^{207}Pb/^{206}Pb$	1691	30				
VJ102420-8A	48.FIN2	$^{207}Pb/^{206}Pb$	1691	32				
VJ102420-8A	49.FIN2	$^{207}Pb/^{206}Pb$	1692	32				
VJ102420-8A	50.FIN2	$^{207}Pb/^{206}Pb$	1692	41				
VJ102420-8A	51.FIN2	$^{207}Pb/^{206}Pb$	1693	37				
VJ102420-8A	52.FIN2	$^{207}Pb/^{206}Pb$	1693	26				
VJ102420-8A	53.FIN2	$^{207}Pb/^{206}Pb$	1694	27				
VJ102420-8A	54.FIN2	$^{207}Pb/^{206}Pb$	1695	36				
VJ102420-8A	55.FIN2	$^{207}Pb/^{206}Pb$	1695	33				
VJ102420-8A	56.FIN2	$^{207}Pb/^{206}Pb$	1697	32				
VJ102420-8A	57.FIN2	$^{207}Pb/^{206}Pb$	1699	36				
VJ102420-8A	58.FIN2	$^{207}Pb/^{206}Pb$	1700	130				
VJ102420-8A	58.FIN2	$^{207}Pb/^{206}Pb$	1701	27				
VJ102420-8A	59.FIN2	$^{207}Pb/^{206}Pb$	1701	36				
VJ102420-8A	60.FIN2	$^{207}Pb/^{206}Pb$	1702	33				
VJ102420-8A	61.FIN2	$^{207}Pb/^{206}Pb$	1702	25				
VJ102420-8A	62.FIN2	$^{207}Pb/^{206}Pb$	1702	47				

Table 4.4. Results of detrital zircon ages for gabbro samples analyzed in this study.

GABBRO AGES

Sample Name Grain#		Best Age (Ma)	1 s.e. (Ma)
VJ313-1b-r3big@1.ais	$^{206}Pb/^{238}U$	71	6
VJ313-1b-r3big.ais	$^{206}Pb/^{238}U$	74	13
VJ313-1b r1A@4.ais	$^{206}Pb/^{238}U$	83	6
VJ313-1b r1A@5.ais	$^{206}Pb/^{238}U$	92	5
VJ313-1b r1A@2.ais	$^{206}Pb/^{238}U$	631	39
VJ313-1b-r1-last.ais	$^{207}Pb/^{206}Pb$	1184	174
VJ313-1b r3A@1.ais	$^{207}Pb/^{206}Pb$	1424	14
VJ313-1b-r1-2tl.ais	$^{207}Pb/^{206}Pb$	1436	264
VJ313-1b-r2A@2.ais	$^{207}Pb/^{206}Pb$	1519	66
VJ313-1b r1A@1.ais	$^{207}Pb/^{206}Pb$	1567	149
VJ313-1b-r3A@5.ais	$^{207}Pb/^{206}Pb$	1571	25
VJ313-1b-r2A@7.ais	$^{207}Pb/^{206}Pb$	1645	50
VJ313-1b-r3A@4.ais	$^{207}Pb/^{206}Pb$	1665	11
VJ313-1b-r2A@3.ais	$^{207}Pb/^{206}Pb$	1733	31
VJ313-1b-r2A@6.ais	$^{207}Pb/^{206}Pb$	1817	45
VJ314-1-r1A@3.ais	$^{206}Pb/^{238}U$	81	6
VJ314-1-r3xx.ais	$^{206}Pb/^{238}U$	92	5
VJ314-1-r3E@1.ais	$^{206}Pb/^{238}U$	160	6
VJ314-1-r3E.ais	$^{206}Pb/^{238}U$	188	14
VJ314-1-r1A@1.ais	$^{206}Pb/^{238}U$	465	16
VJ314-1-r2y.ais	$^{207}Pb/^{206}Pb$	1305	259
VJ314-1-r2D.ais	$^{207}Pb/^{206}Pb$	1338	441
VJ314-1-r1y.ais	$^{207}Pb/^{206}Pb$	1376	39
VJ314-r2D.ais	$^{207}Pb/^{206}Pb$	1384	27
VJ314-1-r3-grA.ais	$^{207}Pb/^{206}Pb$	1390	30
VJ314-1-r3yy@1.ais	$^{207}Pb/^{206}Pb$	1391	11
VJ314-1-r3-grC.ais	$^{207}Pb/^{206}Pb$	1397	11
VJ314-1-r1z.ais	$^{207}Pb/^{206}Pb$	1402	26
VJ314-1-r3A@1.ais	$^{207}Pb/^{206}Pb$	1420	15
VJ314-1-r1D.ais	$^{207}Pb/^{206}Pb$	1433	37
VJ314-1-r3-grB.ais	$^{207}Pb/^{206}Pb$	1498	40
VJ314-1-r1x.ais	$^{207}Pb/^{206}Pb$	1574	64
VJ314-1-r2E.ais	$^{207}Pb/^{206}Pb$	1600	34
VJ314-1-r1E.ais	$^{207}Pb/^{206}Pb$	1662	22
VJ314-1-r2A@1.ais	$^{207}Pb/^{206}Pb$	1664	103
VJ314-1-r3F.ais	$^{207}Pb/^{206}Pb$	1732	39

Sample Name Grain #		Best Age (Ma)	2σ (Ma)
VJ-02-19-22-2A-1	$^{207}Pb/^{206}Pb$	1257	86
VJ-02-19-22-2A-2	$^{207}Pb/^{206}Pb$	1329	85
VJ-02-19-22-2A-3	$^{207}Pb/^{206}Pb$	1308	96
VJ-02-19-22-2A-4	$^{207}Pb/^{206}Pb$	1454	23
VJ-02-19-22-2A-5	$^{207}Pb/^{206}Pb$	1286	87
VJ-02-19-22-2A-6	$^{207}Pb/^{206}Pb$	1284	88
VJ-02-19-22-2A-7	$^{207}Pb/^{206}Pb$	1421	20
VJ-02-19-22-2A-8	$^{207}Pb/^{206}Pb$	1425	23
VJ-02-19-22-2A-9	$^{207}Pb/^{206}Pb$	1325	87
VJ-02-19-22-2A-10	$^{207}Pb/^{206}Pb$	1685	19
VJ-02-19-22-2A-11	$^{207}Pb/^{206}Pb$	1645	17
VJ-02-19-22-2A-12	$^{207}Pb/^{206}Pb$	1321	72
VJ-02-19-22-2A-13	$^{207}Pb/^{206}Pb$	1683	18
VJ-02-19-22-2A-14	$^{207}Pb/^{206}Pb$	1422	20
VJ-02-19-22-2A-15	$^{207}Pb/^{206}Pb$	1607	17
VJ-02-19-22-2A-16	$^{207}Pb/^{206}Pb$	1386	17
VJ-02-19-22-2A-17	$^{207}Pb/^{206}Pb$	1650	15
VJ-02-19-22-2A-18	$^{207}Pb/^{206}Pb$	1587	16
VJ-02-19-22-2A-19	$^{207}Pb/^{206}Pb$	1385	23
VJ-02-19-22-2A-20	$^{207}Pb/^{206}Pb$	1479	16
VJ-02-19-22-2A-21	$^{207}Pb/^{206}Pb$	1445	21
VJ-02-19-22-2A-22	$^{207}Pb/^{206}Pb$	1698	15
VJ-02-19-22-2A-23	$^{207}Pb/^{206}Pb$	1488	29
VJ-02-19-22-2A-24	$^{207}Pb/^{206}Pb$	1609	49
VJ-02-19-22-2A-25	$^{207}Pb/^{206}Pb$	1499	20
VJ-02-19-22-2A-26	$^{207}Pb/^{206}Pb$	1388	29
VJ-02-19-22-2A-27	$^{207}Pb/^{206}Pb$	1666	17
VJ-02-19-22-2A-28	$^{207}Pb/^{206}Pb$	1616	18
VJ-02-19-22-2A-29	$^{207}Pb/^{206}Pb$	1665	15
VJ-02-19-22-2A-30	$^{207}Pb/^{206}Pb$	1609	18
VJ-02-19-22-2A-31	$^{207}Pb/^{206}Pb$	1438	21
VJ-02-19-22-2A-32	$^{207}Pb/^{206}Pb$	1416	33
VJ-02-19-22-2A-33	$^{207}Pb/^{206}Pb$	1442	26
VJ-02-19-22-2A-34	$^{207}Pb/^{206}Pb$	1562	16
VJ-02-19-22-2A-36	$^{207}Pb/^{206}Pb$	1409	26
VJ-02-19-22-2A-37	$^{207}Pb/^{206}Pb$	1591	18
VJ-02-19-22-2A-38	$^{207}Pb/^{206}Pb$	1494	64
VJ-02-19-22-2A-39	$^{207}Pb/^{206}Pb$	1626	17
VJ-02-19-22-2A-40	$^{207}Pb/^{206}Pb$	1608	53

Table 4.5. Results of detrital zircon ages for granitoid samples analyzed in this study.

Felsic Sill Ages (SW Part of map)			
		Best Age	2σ
Sample Name_Grain #		(Ma)	(Ma)
VJ-04-03-22-1-01	$^{206}Pb/^{238}U$	66	3
VJ-04-03-22-1-02	$^{206}Pb/^{238}U$	67	2
VJ-04-03-22-1-03	$^{206}Pb/^{238}U$	65	5
VJ-04-03-22-1-04	$^{206}Pb/^{238}U$	65	2
VJ-04-03-22-1-10	$^{206}Pb/^{238}U$	66	2
VJ-04-03-22-1-13	$^{206}Pb/^{238}U$	69	5
VJ-04-03-22-1-15	$^{206}Pb/^{238}U$	62	3
VJ-04-03-22-1-29	$^{206}Pb/^{238}U$	61	2
VJ-04-03-22-1-30	$^{206}Pb/^{238}U$	63	2
VJ-04-03-22-1-31	$^{206}Pb/^{238}U$	61	1
VJ-04-03-22-1-32	$^{206}Pb/^{238}U$	64	4
VJ-04-03-22-1-33	$^{206}Pb/^{238}U$	64	2
VJ-04-03-22-1-34	$^{206}Pb/^{238}U$	64	2
Granitoid Ages (Footwall)			
VJ-03-11-22-2-35	$^{206}Pb/^{238}U$	21	2
VJ-03-11-22-2-27	$^{206}Pb/^{238}U$	23	1
VJ-03-11-22-2-06	$^{206}Pb/^{238}U$	24	1
VJ-03-11-22-2-21	$^{206}Pb/^{238}U$	24	1
VJ-03-11-22-2-16	$^{206}Pb/^{238}U$	24	1
VJ-03-11-22-2-01	$^{206}Pb/^{238}U$	24	1
VJ-03-11-22-2-23	$^{206}Pb/^{238}U$	24	3
VJ-03-11-22-2-08	$^{206}Pb/^{238}U$	24	1
VJ-03-11-22-2-09	$^{206}Pb/^{238}U$	24	1
VJ-03-11-22-2-24	$^{206}Pb/^{238}U$	24	1
VJ-03-11-22-2-34	$^{206}Pb/^{238}U$	24	1
VJ-03-11-22-2-17	$^{206}Pb/^{238}U$	24	1
VJ-03-11-22-2-13	$^{206}Pb/^{238}U$	25	1
VJ-03-11-22-2-32	$^{206}Pb/^{238}U$	25	2
VJ-03-11-22-2-19	$^{206}Pb/^{238}U$	50	2
VJ-03-11-22-2-18	$^{206}Pb/^{238}U$	67	1
VJ-03-11-22-2-02	$^{206}Pb/^{238}U$	69	1
VJ-03-11-22-2-25	$^{206}Pb/^{238}U$	71	1
VJ-03-11-22-2-15	$^{206}Pb/^{238}U$	74	2
VJ-03-11-22-2-03	$^{206}Pb/^{238}U$	76	3
VJ-03-11-22-2-11	$^{206}Pb/^{238}U$	166	4
VJ-03-11-22-2-05	$^{206}Pb/^{238}U$	220	6
VJ-03-11-22-2-20	$^{206}Pb/^{238}U$	844	17
VJ-03-11-22-2-07	$^{206}Pb/^{238}U$	940	21
VJ-03-11-22-2-26	$^{207}Pb/^{206}Pb$	1392	89

Granitoid Ages (Hanging Wall)			
		Best Age	2σ
Sample Name_Grain #		(Ma)	(Ma)
VJ-03-11-22-1-1	$^{207}Pb/^{206}Pb$	1887	19
VJ-03-11-22-1-2	$^{207}Pb/^{206}Pb$	1786	18
VJ-03-11-22-1-3	$^{207}Pb/^{206}Pb$	1779	55
VJ-03-11-22-1-4	$^{207}Pb/^{206}Pb$	1734	18
VJ-03-11-22-1-5	$^{207}Pb/^{206}Pb$	1603	84
VJ-03-11-22-1-6	$^{207}Pb/^{206}Pb$	1753	17
VJ-03-11-22-1-7	$^{207}Pb/^{206}Pb$	1775	19
VJ-03-11-22-1-8	$^{207}Pb/^{206}Pb$	1684	45
VJ-03-11-22-1-9	$^{207}Pb/^{206}Pb$	1845	18
VJ-03-11-22-1-10	$^{207}Pb/^{206}Pb$	1738	17
VJ-03-11-22-1-11	$^{207}Pb/^{206}Pb$	1783	24
VJ-03-11-22-1-12	$^{207}Pb/^{206}Pb$	1696	16
VJ-03-11-22-1-13	$^{207}Pb/^{206}Pb$	1792	17
VJ-03-11-22-1-14	$^{207}Pb/^{206}Pb$	1795	16
VJ-03-11-22-1-15	$^{207}Pb/^{206}Pb$	1704	16
VJ-03-11-22-1-16	$^{207}Pb/^{206}Pb$	1749	15
VJ-03-11-22-1-17	$^{207}Pb/^{206}Pb$	1765	15
VJ-03-11-22-1-19	$^{207}Pb/^{206}Pb$	1659	18
VJ-03-11-22-1-20	$^{207}Pb/^{206}Pb$	1758	17
VJ-03-11-22-1-21	$^{207}Pb/^{206}Pb$	1747	15
VJ-03-11-22-1-22	$^{207}Pb/^{206}Pb$	1770	15
VJ-03-11-22-1-23	$^{207}Pb/^{206}Pb$	1758	16
VJ-03-11-22-1-24	$^{207}Pb/^{206}Pb$	1766	15
VJ-03-11-22-1-25	$^{207}Pb/^{206}Pb$	1746	17
VJ-03-11-22-1-26	$^{207}Pb/^{206}Pb$	1766	15
VJ-03-11-22-1-27	$^{207}Pb/^{206}Pb$	1773	16
VJ-03-11-22-1-28	$^{207}Pb/^{206}Pb$	1772	15
VJ-03-11-22-1-29	$^{207}Pb/^{206}Pb$	1845	15
VJ-03-11-22-1-30	$^{207}Pb/^{206}Pb$	1774	16
VJ-03-11-22-1-31	$^{207}Pb/^{206}Pb$	1754	15
VJ-03-11-22-1-32	$^{207}Pb/^{206}Pb$	1769	15
VJ-03-11-22-1-33	$^{207}Pb/^{206}Pb$	1738	15
VJ-03-11-22-1-34	$^{207}Pb/^{206}Pb$	1783	16
VJ-03-11-22-1-35	$^{207}Pb/^{206}Pb$	1740	17

Table 4.6. Trace elemental data for gabbro and two schist samples in Figure 5.4.

	W22238002	W22238004	Ref	W22238003	Ref	W22238005	Ref	W22238039	W22238045	W22238048
	BLANK	BHVO-2	BHVO-2	BCR-2	BCR-2	RGM-2	RGM-2	VJ02-19-22-2A	VJ-03-12-22-12	VJ-03-12-22-4
	BLANK	Standard	*Standard*	Standard	*Standard*	Standard	*Standard*	**Gabbro + quartz veins**	**garnet-mica schist**	**garnet-biotite schist**
Li	0.0454	4.37	4.80	9.12	9.0	61.8	57.0	4.10	14.5	19.0
Be	0.0000	0.95	1.0	2.16		2.46	2.37	2.49	0.75	0.12
Sc	0.0236	31.9	32.0	33.4	33.0	4.46	4.40	33.4	14.3	27.1
V	0.0992	320	317	410	416	11.7	13.0	202	77.0	146
Cr	0.1237	275	280	14.0	16.5	6.97	5.90	252	85.1	153
Co	0.0374	44.5	45.0	36.7	37.0	1.96	2.0	35.4	14.8	32.2
Ni	0.0499	119	119	11.8	13.0	5.04	5.20	60.8	29.1	62.2
Cu	0.0190	131	127	18.2	19.7	9.41	9.60	94.4	23.2	50.4
Zn	0.0312	105	103	133	133	31.8	32.0	74.3	88.4	125
Ga	0.0033	22.1	21.7	22.8	23.0	16.3	16.5	18.6	20.8	37.5
Rb	0.0049	9.05	9.11	47.4	46.9	150	150	15.9	80.6	146
Sr	0.0054	398	396	341	340	107	108	246	371	87.5
Y	0.0001	26.5	26.0	36.8	37.0	22.8	23.2	47.0	31.5	40.1
Zr	0.0245	170	172	185	184	222	220	69.7	189	144
Nb	0.0004	18.5	18.1	12.6	12.6	8.99	9.30	11.2	11.7	11.9
Sn	0.0051	1.61	1.70	2.23	2.03	3.46	3.34	1.86	1.57	4.07
Cs	0.0010	0.096	0.10	1.08	1.10	9.82	9.60	0.13	0.60	0.73
Ba	0.0265	127	131	669	677	826	810	249	1252	1666
La	0.0004	15.5	15.2	25.1	24.9	23.4	24.0	12.1	59.1	66.5
Ce	0.0010	38.1	37.5	52.9	52.9	46.5	47.0	32.0	112	123
Pr	0.0000	5.42	5.35	6.80	6.70	5.26	5.36	4.49	12.6	12.3
Nd	0.0010	24.6	24.5	28.4	28.7	19.3	19.0	20.2	45.6	43.6
Sm	0.0000	6.17	6.07	6.61	6.58	4.10	4.30	5.70	7.88	7.77
Eu	0.0000	2.05	2.07	1.98	1.96	0.66	0.66	1.85	2.13	1.91
Gd	0.0000	6.14	6.24	6.84	6.75	3.70	3.70	6.63	6.28	6.87
Tb	0.0000	0.98	0.92	1.07	1.07	0.58	0.66	1.09	0.86	1.12
Dy	0.0000	5.47	5.31	6.50	6.41	3.80	4.10	7.85	5.30	7.15
Ho	0.0000	1.01	0.98	1.30	1.28	0.78	0.82	1.70	1.15	1.42
Er	0.0000	2.57	2.54	3.63	3.66	2.31	2.35	4.88	3.29	3.95
Tm	0.0000	0.35	0.33	0.53	0.54	0.37	0.37	0.71	0.51	0.60
Yb	0.0001	2.02	2.0	3.41	3.38	2.54	2.60	4.82	3.44	4.09
Lu	0.0001	0.28	0.27	0.51	0.50	0.39	0.40	0.74	0.55	0.61
Hf	0.0003	4.45	4.36	4.99	4.90	5.94	6.20	2.46	5.11	4.04
Ta	0.0006	1.20	1.14	0.77	0.78	0.89	0.95	0.70	0.43	0.33
Tl	0.0520	0.10	0.058	0.31		0.88	0.93	0.11	0.40	0.65
Pb	0.0067	1.53	1.60	10.9	11.0	19.4	19.3	6.81	17.1	8.73
Th	0.0005	1.22	1.22	5.95	5.70	14.8	15.1	0.51	15.9	14.3
U	0.0000	0.43	0.40	1.66	1.69	5.77	5.80	0.40	0.51	0.33

Blank: 10-9 (ng/g), Standard Sample: 10-6 (µg/g).

4.9 References

Anderson, J.L. & Rowley, M.C. Mineralogist, C. (1981). Synkinematic intrusion of peraluminous and associated peraluminous granitic magmas, Whipple Mountains. California. *The Canadian Mineralogist*, *19*, 83-101.

Anderson, J. L., Barth, A. P., & Young, E. D. (1988). Mid-crustal Cretaceous roots of Cordilleran metamorphic core complexes. *Geology*, *16*(4), 366-369.

Anderson, J. L., Jenney, J. P., & Reynolds, S. J. (1989). Proterozoic anorogenic granites of the southwestern United States. *Geologic evolution of Arizona*, *17*, 211-238.

Axen, G. J., van Wijk, J. W., & Currie, C. A. (2018). Basal continental mantle lithosphere displaced by flat-slab subduction. *Nature Geoscience*, *11*(12), 961-964.

Chapman, A. D., Rautela, O., Shields, J., Ducea, M. N., & Saleeby, J. (2020). Fate of the lower lithosphere during shallow-angle subduction: The Laramide example. *GSA Today*, *30*(1), 4-10.

Coney, P. J., Jones, D. L., & Monger, J. W. (1980). Cordilleran suspect terranes. Nature, 288(5789), 329-333.

Copeland, P., Currie, C. A., Lawton, T. F., & Murphy, M. A. (2017). Location, location, location: The variable lifespan of the Laramide orogeny. *Geology*, *45*(3), 223-226.

Crowell, J. C. (1981). An outline of the tectonic history of southeastern California.

Davis, G. A., J. L. Anderson, E. G. Frost, and T. J. Shackelford (1980), Mylonitization and detachment faulting in the Whipple-Buckskin-Rawhide Mountains terrane, southeastern California and western Arizona, Geol. Soc. Am. Mem., 153,79–130.

Davis, G. A., Anderson, J. L., Martin, D. L., Krummenacher, D., Frost, E. G., & Armstrong, R.

L. (1982). Geologic and geochronologic relations in the lower plate of the Whipple detachment fault, Whipple Mountains, southeastern California: A progress report. *Mesozoic-Cenozoic tectonic evolution of the Colorado River region, California, Arizona, and Nevada: San Diego, California, Cordilleran Publishers*, 408-432.

Davis, G. H., & Coney, P. J. (1979). Geologic development of the Cordilleran metamorphic core complexes. Geology, 7(3), 120-124.

Davis, G. H. (1987). A shear-zone model for the structural evolution of metamorphic core complexes in southeastern Arizona. *Geological Society, London, Special Publications*, *28*(1), 247-266.

Dawson, M. R., & Jacobson, C. E. (1989). Geochemistry and origin of mafic rocks from the Pelona, Orocopia, and Rand Schists, southern California. *Earth and planetary science letters*, *92*(3-4), 371-385.

Ernst, W. G., & Rubey, W. W. (1981). *The geotectonic development of California*. Prentice-Hall.

Gans, P. B., & Gentry, B. J. (2016). Dike emplacement, footwall rotation, and the transition from magmatic to tectonic extension in the Whipple Mountains metamorphic core complex, southeastern California. *Tectonics*, *35*(11), 2564-2608.

Gehrels, G. E., Valencia, V. A., & Ruiz, J. (2008). Enhanced precision, accuracy, efficiency, and spatial resolution of U-Pb ages by laser ablation–multicollector–inductively coupled plasma–mass spectrometry. *Geochemistry, Geophysics, Geosystems*, *9*(3).

Grove, M., Jacobson, C. E., Barth, A. P., & Vucic, A. (2003). Temporal and spatial trends of Late Cretaceous-early Tertiary underplating Pelona and related schist beneath Southern California and southwestern Arizona.

Harrison, T. M., & Watson, E. B. (1983). Kinetics of zircon dissolution and zirconium diffusion

in granitic melts of variable water content. *Contributions to Mineralogy and Petrology*, *84*, 66-72.

Harrison, T. M., McKeegan, K. D., & LeFort, P. (1995). Detection of inherited monazite in the Manaslu leucogranite by $^{208}Pb/^{232}Th$ ion microprobe dating: crystallization age and tectonic implications. *Earth and Planetary Science Letters*, *133*(3-4), 271-282.

Hart, N. R., Stockli, D. F., & Hayman, N. W. (2016). Provenance evolution during progressive rifting and hyperextension using bedrock and detrital zircon U-Pb geochronology, Mauléon Basin, western Pyrenees. *Geosphere*, *12*(4), 1166-1186.

Horstwood, M. S., Košler, J., Gehrels, G., Jackson, S. E., McLean, N. M., Paton, C., ... & Schoene, B. (2016). Community-derived standards for LA-ICP-MS U-(Th-) Pb geochronology–Uncertainty propagation, age interpretation and data reporting. *Geostandards and Geoanalytical Research*, *40*(3), 311-332.

Howard, K. A., & John, B. E. (1987). Crustal extension along a rooted system of imbricate low-angle faults: Colorado River extensional corridor, California and Arizona. *Geological Society, London, Special Publications*, *28*(1), 299-311.

Jacobson, C. E., Grove, M., Vucic, A., Pedrick, J. N., & Ebert, K. A. (2007). Exhumation of the Orocopia Schist and associated rocks of southeastern California: Relative roles of erosion, synsubduction tectonic denudation, and middle Cenozoic extension.

Jacobson, C. E., Grove, M., Pedrick, J. N., Barth, A. P., Marsaglia, K. M., Gehrels, G. E., & Nourse, J. A. (2011). Late Cretaceous–early Cenozoic tectonic evolution of the southern California margin inferred from provenance of trench and forearc sediments. *Bulletin*, *123*(3-4), 485-506.

Kapp, P., Jepson, G., Carrapa, B., Schaen, A. J., He, J. J., & Wang, J. W. (2023). Laramide

bulldozing of lithosphere beneath the Arizona transition zone, southwestern United States. *Geology*, *51*(10), 952-956.

Lister, G. S., Banga, G., & Feenstra, A. (1984). Metamorphic core complexes of Cordilleran type in the Cyclades, Aegean Sea, Greece. *Geology*, *12*(4), 221-225.

Liu, L., & Stockli, D. F. (2020). U-Pb ages of detrital zircons in lower Permian sandstone and siltstone of the Permian Basin, west Texas, USA: Evidence of dominant Gondwanan and peri-Gondwanan sediment input to Laurentia. *GSA Bulletin*, *132*(1-2), 245-262.

Murphy, M. A., Yin, A., Kapp, P., Harrison, T. M., Manning, C. E., Ryerson, F. J., ... & Jinghui, G. (2002). Structural evolution of the Gurla Mandhata detachment system, southwest Tibet: Implications for the eastward extent of the Karakoram fault system. *Geological Society of America Bulletin*, *114*(4), 428-447.

Odlum, M. L., Capaldi, T. N., Thomson, K. D., & Stockli, D. F. (2024). Tracking cycles of Phanerozoic opening and closing of ocean basins using detrital rutile and zircon geochronology and geochemistry. *Geology*, *52*(5), 357-361.

Strickland, E. D., Singleton, J. S., & Haxel, G. B. (2018). Orocopia Schist in the northern Plomosa Mountains, west-central Arizona: A Laramide subduction complex exhumed in a Miocene metamorphic core complex. *Lithosphere*, *10*(6), 723-742.

Whitney, D. L., Teyssier, C., Rey, P., & Buck, W. R. (2013). Continental and oceanic core complexes. *Bulletin*, *125*(3-4), 273-298.

5 Summary

The topics covered in this dissertation focus on tectonic processes occurring in the Whipple Mountains metamorphic core complex, southeastern California. The purpose of this work was to understand the geology of the area and see how these results fit in with the evolution of the North American Cordillera. The first chapter summarizes the tectonic history of the North American Cordillera metamorphic core complex belt that forms a North-South-trending belt from British Columbia, Canada to Northern Mexico (Armstrong, 1982; Miller and Bradfish, 1980). The North American Cordillera is generally divided a northern, central, and southern segment where core-complex extension and metamorphism have been well-constrained in the northern and central segments, but the southern segment is lacking data (Chapman et al., 2021). In order to constrain the timing of extension and metamorphism in the Whipple Mountains, quartzofeldspathic garnet-rich gneisses and schists from the footwall of the Whipple detachment shear zone were collected analyzed. The garnet-plagioclase-biotite-muscovite-rich mineral assemblage allowed for thermobarometric analysis and new pressure-temperature estimates were found for metamorphism in the Whipple ductile shear zone (Lanari and Engi, 2017; Lanari & Duesterhoeft, 2019). The rim, 680-750°C and 7-9.4 kbar and core, 750-800°C and 6.2-7.8 kbar P-T conditions are higher than previously established as ~500°C and 4-5 kbar by Behr and Platt (2011). Furthermore, monazite inclusions in garnets are helpful in dating the timing of deformation by using Th-Pb radiometric dating and yielded monazite-inclusion 62±9 Ma, 67±7 Ma, and 80±6 Ma (Th-Pb dates, ±1σ)) ages (Catlos et al., 2002; Harrison et al., 1995).

The second chapter focuses on calculating the pore-fluid pressure ratios at the brittle-ductile transition zone from samples in the Whipple Mountains brittle-ductile shear zone. Since brittle-ductile deformation mechanisms are preserved throughout the shear zone rock mechanics

can be used to represent cataclastic deformation and dislocation creep flow laws used to represent crystal-plastic deformation. The equations related to each deformation mechanism were set equal to each other to determine unknown variables (e.g. differential and shear stress, strain rate, pore-fluid pressure ratio, strain rate, etc.). The calculated pore-fluid pressure ratios, λ = 0.92-1.11, suggest pore-fluid pressure was greater than the lithostatic pressure and quartz veins were allowed to form throughout the shear zone. This method may be applied to other areas and may provide insights into slow-slip earthquakes or tremors (Yin, 2018).

The last chapter analyzes more monazite-in-garnet ages to further constrain the deformation timing of mylonitization in the Whipple Mountains ductile shear zone. Detrital zircon and zircon crystallization ages were also collected. Both dating methods yielded Late-Cretaceous to Paleocene ages that we attribute to a thermal event due to slab rollback and asthenosphere upwelling into the slab wedge. A model was proposed to explain the high P-T conditions as well as zircon and monazite Paleocene ages.

5.1 References

Armstrong, R. L. (1982). Cordilleran metamorphic core complexes-from Arizona to southern Canada. Annual review of earth and planetary sciences, 10, 129.

Behr, Whitney M., and John P. Platt. "A naturally constrained stress profile through the middle crust in an extensional terrane." *Earth and Planetary Science Letters* 303.3-4 (2011): 181-192.

Catlos, E. J., Gilley, L. D., & Harrison, T. M. (2002). Interpretation of monazite ages obtained via in situ analysis. Chemical Geology, 188(3-4), 193-215.

Chapman, J. B., Runyon, S. E., Shields, J. E., Lawler, B. L., Pridmore, C. J., Scoggin, S. H., ... & Haxel, G. B. (2021). The north American cordilleran anatectic belt. *Earth-Science Reviews*, *215*, 103576.

Harrison, T. M., Copeland, P., Kidd, W. S. F., & Lovera, O. M. (1995). Activation of the Nyainqentanghla shear zone: Implications for uplift of the southern Tibetan Plateau. *Tectonics*, *14*(3), 658-676.

Lanari, P., & Engi, M. (2017). Local bulk composition effects on metamorphic mineral assemblages. Reviews in mineralogy and geochemistry, 83(1), 55-102.

Lanari, P., & Duesterhoeft, E. (2019). Modeling metamorphic rocks using equilibrium thermodynamics and internally consistent databases: Past achievements, problems and perspectives. Journal of Petrology, 60(1), 19-56.

Miller, C. F., & Bradfish, L. J. (1980). An inner Cordilleran belt of muscovite-bearing plutons. *Geology*, *8*(9), 412-416.

Yin, A. (2018). Water hammers tremors during plate convergence. *Geology*, *46*(12), 1031-1034.